T2R2 東京科学大学 リサーチリポジトリ
Science Tokyo Research Repository

論文 / 著書情報
Article / Book Information

題目(和文)	デッドゾーン内側境界における岩石微惑星形成：円盤表層の影構造と太陽系形成過程への示唆
Title(English)	Planetesimal Formation at the Inner Edge of the Dead Zone: Implications for Disk Observations and Solar System Formation
著者(和文)	植田高啓
Author(English)	Takahiro Ueda
出典(和文)	学位:博士(理学), 学位授与機関:東京工業大学, 報告番号:甲第11051号, 授与年月日:2019年3月26日, 学位の種別:課程博士, 審査員:井田 茂,奥住 聡,中本 泰史,野村 英子,佐藤 文衛
Citation(English)	Degree:Doctor (Science), Conferring organization: Tokyo Institute of Technology, Report number:甲第11051号, Conferred date:2019/3/26, Degree Type:Course doctor, Examiner:,,,,
学位種別(和文)	博士論文
Type(English)	Doctoral Thesis

Powered by T2R2 (Science Tokyo Research Repository)

Planetesimal Formation at the Inner Edge of the Dead Zone: Implications for Disk Shadows and Solar System Formation

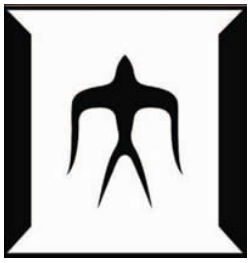

Takahiro Ueda

Department of Earth and Planetary Sciences

Tokyo Institute of Technology

A thesis submitted for the degree of

Doctor of Science

February 26, 2019

Abstract

Planets are thought to form from micron-sized dust particles within a protoplanetary disk rotating around the central star. In the evolution of dust particles, they are thought to form kilometer-sized bodies, so-called planetesimals, which are the building blocks of planets. However, formation of planetesimals, especially rocky ones, is still unclear because dust particles are easy to fragment at a typical collisional velocity in protoplanetary disks and rapidly spiral into the central star.

One preferential site of rocky planetesimal formation is the inner edge of the so-called dead zone. The dead zone is the location where magneto-rotational instability (MRI) is suppressed because of poor gas ionization. The dead zone is likely to have an inner edge where the gas temperature reaches $\sim$ 1000 K, above which thermal ionization of the gas is effective enough to activate MRI. Across the dead zone inner edge, the turbulent viscosity arising from MRI steeply decreases from inside out, resulting in a local maximum in the radial profile of the gas pressure. The pressure maximum traps solid particles drifting from the outer part of the disk, leading potentially to the formation of rocky planetesimals via the gravitational clumping of the dust layer.

In this thesis, we first analytically investigate the temperature structure of the inner region of protoplanetary disks based on the results from the recent radiation hydrodynamical simulations. The inner part of a disk can be divided into four regions: a dust-free region with a gas temperature in the optically thin limit, an optically thin dust halo, an optically thick condensation front, and the classical, optically thick region, in order from the innermost to the outermost. We derive the analytic expressions successfully describing these characteristic structures obtained from the numerical simulations. We find that the radius of the dead zone inner edge predicted from our formulas is $\sim$ 2-3 times larger than that expected from the temperature profile of the classical optically thick disk model.

As a next step, we perform simulations of the dust and gas disk evolution around a Herbig Ae star to investigate the planetesimal formation at the dead-zone inner edge. We show that the total mass of planetesimals is sensitive to the turbulence strength in the dead zone because of the combined effect of turbulence-induced particle fragmentation and turbulent diffusion. For a typical critical fragmentation velocity of silicate dust particles of 1 m s^{-1}, the stress to pressure ratio in the dead zone needs to be lower than 3×10^{-4} for dust trapping to operate.

The obtained dust distribution is postprocessed using the radiative transfer code RADMC-3D to investigate the effect of a shadow casted by the dust-pileup. We find that a dust pileup at the dead-zone inner edge, if present, casts a shadow extending out to $\sim$ 10 au. In the shadowed region the temperature significantly drops, which in some cases yields even multiple water snow lines. We also find that even without a dust pileup at the dead-zone inner edge, the disk surface can become thermally unstable, and the excited waves can naturally produce shadows and ring-like structures in observed images. This mechanism might account for the ring-like structures seen in the scattered light images of some disks, such as the TW Hya disk.

Finally, we investigate whether rocky planetesimal formation at the dead-zone inner edge can account for the formation of inner solar system planets by performing simulations of the dust and gas disk evolution around a Sun-like star. We show that if the disk is viscously heated, rocky planetesimals form at $\sim$ 0.7–1 au via the dust-pileup at the dead-zone inner edge. In addition, we also show that the total mass of planetesimals invoked from the total mass of inner solar system planets can also be reproduced. However, the turbulence strength in the dead-zone needs to be finely tuned because the total mass of planetesimals is quite sensitive to it. Since the disk needs to be massive for the dead-zone inner edge to be located at $\sim$ 0.7–1 au, the disk needs to have a outer edge of $\lesssim$ 80 au to be gravitationally stable. Although the subsequent evolution of the planetesimals has large uncertainty, this scenario would potentially account for the inner solar system formation.

Contents

1 General Introduction **1**

1.1 Exoplanets 2
1.2 Protoplanetary Disk Observations 3
1.3 Physical Structure of Protoplanetary Disks 6
1.4 Dust Dynamics in Protoplanetary Disks 9
1.5 Difficulties in Planetesimal Formation 13
1.5.1 Radial drift barrier 13
1.5.2 Fragmentation barrier 14
1.6 Inner Edge of the Dead Zone 16
1.6.1 Dead zone in protoplanetary disks 16
1.6.2 Dust-trapping at the inner edge of the dead zone 18
1.7 About this thesis 20

2 Analytic Expressions for the Inner-Rim Structure of Passively Heated Protoplanetary Disks **22**

2.1 Abstract of this Chapter 23
2.2 Introduction of this Chapter 24
2.3 Analytic Solutions for the Inner Rim Structure 25
2.3.1 Region A: Optically thin dust-free region 26
2.3.2 Region B: Optically thin dust halo region 26
2.3.3 Region C: Optically thick dust condensation front 28
2.3.4 Region D: Optically thick region 30
2.4 Discussion 35
2.4.1 The position of the dead zone inner edge 35
2.4.2 The effect of viscous heating 37
2.4.3 Migration trap 38
2.4.4 Instabilities at the inner region of protoplanetary disks . . . 38
2.5 Summary 39

2.6 Appendix 40
2.6.1 Effect of the evaporation temperature 40

3 Dust-Pileup at the Dead-Zone Inner Edge and Implications for the Disk Shadow 42
3.1 Abstract of this Chapter 43
3.2 Introduction of this Chapter 44
3.3 Dust-Pileup at the Dead-Zone Inner Edge 45
3.3.1 Dust and gas evolution models 45
3.3.1.1 Surface density evolution 46
3.3.1.2 Dust-size evolution 47
3.3.1.3 Radial temperature profile 49
3.3.1.4 Turbulence 50
3.3.1.5 Planetesimal formation 50
3.3.2 Results of simulations of dust and gas disk evolution 51
3.4 Radiative Transfer Simulations 55
3.4.1 Radiative transfer models 55
3.4.2 Results of radiative transfer simulations 56
3.4.2.1 Radial intensity profile 56
3.4.2.2 Synthetic images 58
3.4.2.3 Midplane temperature 60
3.4.2.4 Spectral energy distribution 61
3.5 Waves on the Disk Surface 62
3.6 Discussion 64
3.6.1 Implications for planet formation 64
3.6.2 Feedback from the shadows on dust growth 66
3.6.3 Implications for disk observations 66
3.7 Summary 67
3.8 Appendix 68
3.8.1 Details of the oscillatory behavior 68
3.8.2 Convergence of the Thermal Monte Carlo simulation 70
3.8.3 Effect of Scattering 70

4 Inner Solar System Formation via the Dust-Pileup at the Dead-Zone Inner Edge **74**
4.1 Abstract of this Chapter 75
4.2 Introduction of this Chapter 76
4.3 Calculation Method 77
4.4 Results 78
4.4.1 Disk evolution 78
4.4.2 Planetesimal surface density 80
4.4.3 Condition for the inner solar system formation 81
4.5 Discussion 83
4.5.1 Dependence on Planetesimal Formation Model 83
4.5.2 Effect of uncertainty in the opacity on the planetesimal formation 85
4.5.3 Implication from the cosmochemical constraints 85
4.5.4 Migration of formed planetesimals 86
4.6 Summary 87
4.7 Appendix 88
4.7.1 Instability induced by the opacity gradient 88

5 Summary and Future Prospect **91**

Bibliography **96**

Chapter 1

General Introduction

1.1 Exoplanets

Recent exoplanet observations have revealed that the planetary systems are very diverse. Figure 1.1 shows the mass and semi-major axis distribution of detected plan-

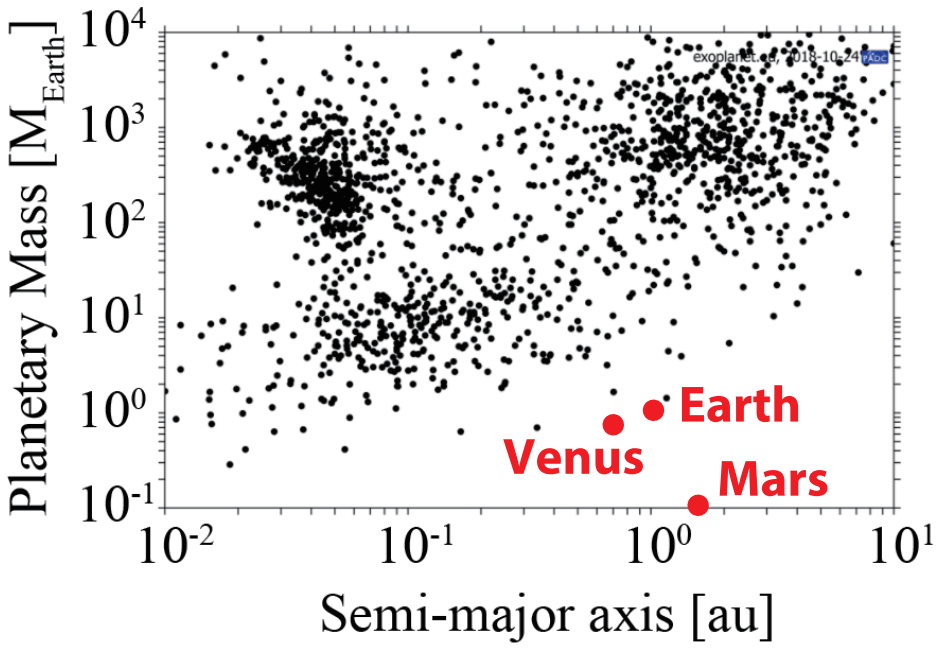

Figure 1.1: Mass and semi-major axis distribution of detected planets.

ets. The data is taken from The Extrasolar Planets Encyclopaedia[1]. We clearly see that there are three distinct groups of planets. The first group is the so-called cold Jupiters: planets having a mass similar to Jupiter mass and located at outside of $\sim$ 1 au. The second group is the so-called hot Jupiters: the mass is similar to that of Jupiter but they are located at < 0.1 au. The third group is the so-called close-in super-earths: the mass is $\sim$ 1–30$M_\oplus$ and the semi-major axis is < 1 au. If we correct an observational bias, the occurence rate of hot Jupiters, cold Jupiters and super-earths around Sun-like stars are estimated to be around 0.5%, 10% and 30%, respectively (e.g., Fressin et al. 2013; Santerne et al. 2016; Zhu et al. 2018). Hence, we can say that close-in super-earths are not rare objects but are common around Sun-like stars. Figure 1.1 also shows the distribution of solar system terrestrial planets except for Mercury. Although it is difficult to detect planets similar to the solar system terrestrial planets because of the combined effect of their small masses and

[1] `http://exoplanet.eu`

large semi-major axes, we can say that the mass and semi-major axis distribution of detected exoplanets is dramatically different from that of the solar system terrestrial planets.

The formation mechanism of these close-in planets is still under discussion. One of the most plausible models is the so-called in-situ formation model (e.g., Ogihara et al. 2018). This model can explain the fact that many of close-in planets are not in mean motion resonances with other planets. However, this model needs $\sim$ 5–10 times higher solid mass than the MMSN disk (Hayashi, 1981) which has been traditionally accepted disk model inferred from the mass distribution of current solar system. Another formation scenario for these planets is formation at the outer region followed by the inward migration (e.g., Coleman & Nelson 2016). In this model, planets form at the outer region and inwardly migrate via the gravitational interaction with the disk gas. This model does not need large solid mass in the inner region since the planets form at the outer region. However, migrating planets are easily trapped into the mean motion resonances with other planets, which the observation does not support. The so-called inside-out formation model is also plausible model for close-in exoplanets (e.g., Chatterjee & Tan 2014). In this model, a super-earth is assumed to form at the so-called dead-zone inner edge via the dust-pileup. The formed super-earth opens a gap in the gas disk, leading to enhanced ionization and a retreat of the dead zone inner edge. This model potentially account for the mass of the observed super-earths and orbital separation of the planets. However, this hypothesis strongly relies on the dust dynamics on which we will focus in the following sections.

1.2 Protoplanetary Disk Observations

Planets are thought to be formed from micron-sized dust particles in protoplanetary disks. By observing the protoplanetary disks, we can obtain the information about the formation environment of planets. Figure 1.2 shows the schematic of the disk observations at different observing wavelengths. Using the different observing wavelengths, we can understand the three-dimensional structure of the disks. If we look at the disk with the near-infrared wavelength, we observe the scattered light from the disk surface which traces the distribution of micron-sized small grains. Observations at the mid-infrared wavelength trace the thermal emission from warm dust particles ($\sim$30–300 K) and the molecular emissions from such as H_2O and CO_2. If we use the (sub-)millimeter wavelength, we can obtain the information about the thermal emission from the millimeter-sized particles located at the disk mid-plane.

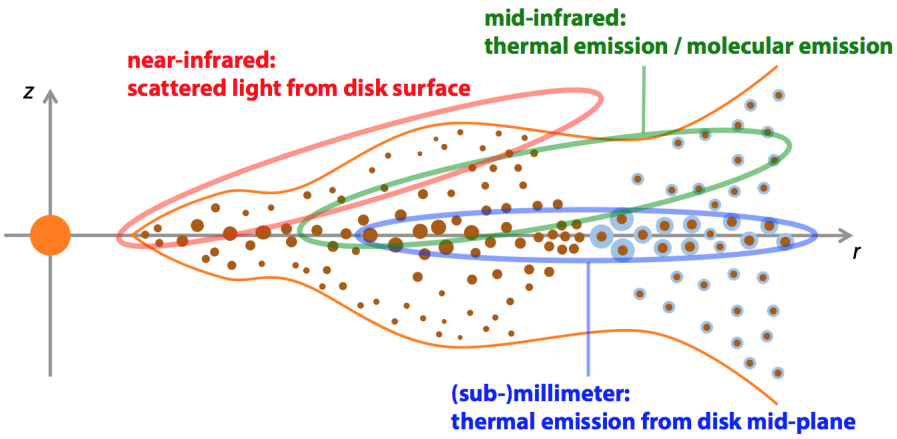

Figure 1.2: Schematic of disk observations at different observing wavelengths. Different observing wavelengths trace different locations in the disk.

Recent infrared observations have revealed that many protoplanetary disks have gaps and ring-like structures on its surface (Figure 1.3, e.g., Avenhaus et al. 2018). The origin of these structures on disk surface have been actively debated. One plausible explanation for these structure is a gap opened by giant planets (e.g., Kanagawa et al. 2015, Kanagawa et al. 2016). A giant planet embedded in a protoplanetary disk forms a gap by gravitationally pushing out the surrounding disk gas. If the surface density has a gap, the disk surface drops off in the gap region, leading to a shadow at the gap and a bright ring at the outer edge of the gap. The TW Hya disk is a nice example having three gaps at < 6 au, ≈ 21 au and ≈ 85 au in the polarized scattered light profile (van Boekel et al., 2017). Theoretical modeling of the planet-opened gap suggests that these gaps are opened by planets with masses of $6M_{\oplus}$, $15M_{\oplus}$ and $34_{\oplus}$, from the inner one to outer one (van Boekel et al. 2017, Mentiplay et al. 2018). However, it is still unclear that these gaps are indeed opened by the planets because there has been no detection of planets within observed gaps except for the disk around PDS 70 (Keppler et al., 2018). In addition, some numerical simulations suggest that gap-opening planets excite the spiral arm which should be detected by the current observations (Mentiplay et al., 2018).

Recent ALMA observations have also shown that many protoplanetary disks have gaps and ring-like structures in the radial profile of the dust continuum emission (Figure 1.4, e.g., ALMA Partnership et al. 2015). In contrast to the near-infrared observations, these observations trace the dust continuum emission which is expected to be dominated by a population of millimeter-sized grains concentrated near the disk

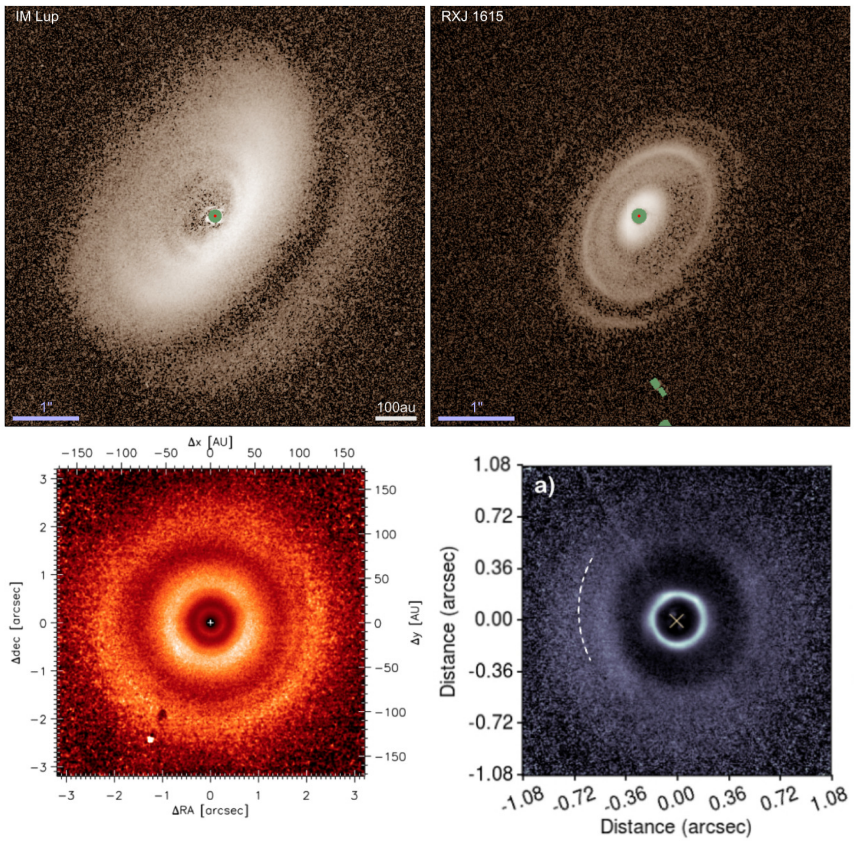

Figure 1.3: Images of disks having gaps and ring-like structures in near-infrared observations. *top left*: the IM Lup disk (Avenhaus et al., 2018), *top right*: the RXJ 1615 disk (Avenhaus et al., 2018), *bottom left*: the TW Hya disk (van Boekel et al., 2017), *bottom right*: the HD 169142 disk (Bertrang et al., 2018),

midplane. The TW Hya disk has gaps also in the dust continuum emission (Andrews et al. 2016, Nomura et al. 2016). Although there are some differences in the structural features in near-infrared and millimeter observations, there is some correspondence between them (van Boekel et al., 2017).

In order to explain these gaps in the dust continuum emission, some plausible mechanisms have been proposed. The first one is a gap opened by a planet, which is the same as mentioned above. If the disk has a gap in the surface gas density, millimeter-sized particles are trapped at the outer edge of the gap, resulting into the depletion of dust particles within the gap in the gas disk (e.g., Bae et al. 2018). Another explanation is formation of gaps and rings around the condensation fronts (e.g., Banzatti et al. 2015; Okuzumi et al. 2016). Around the condensation fronts, dust radii and opacities are expeceted to be changed due to the evaporation and sintering-

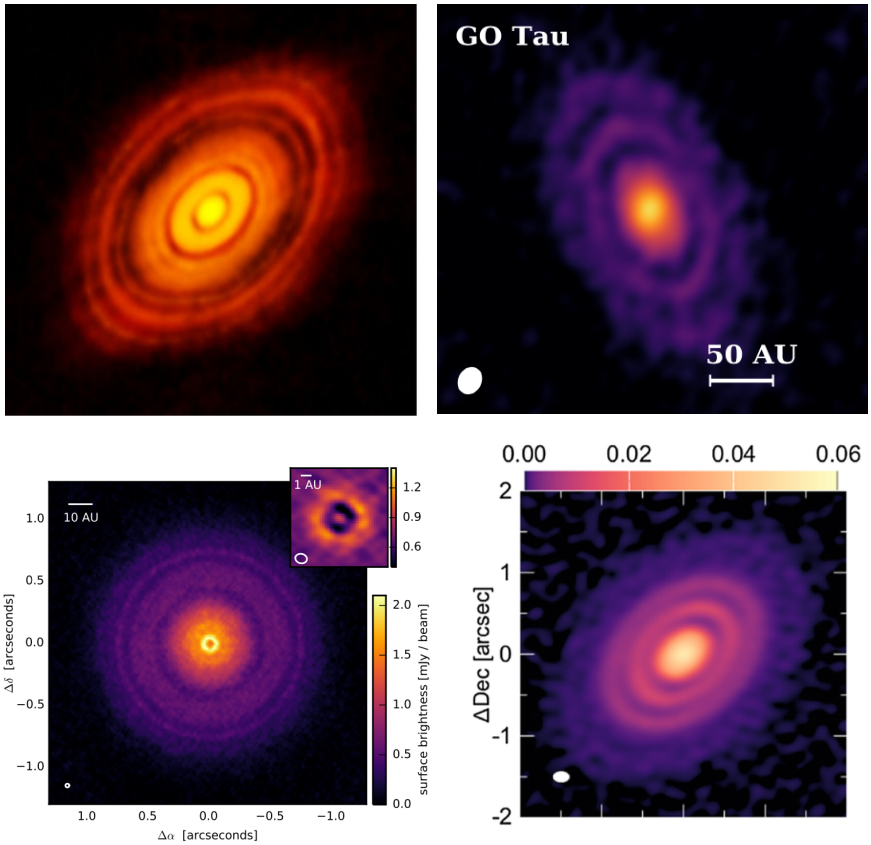

Figure 1.4: Images of disks having gaps and ring-like structures in dust continuum observations. *top left*: the HL Tau disk (ALMA Partnership et al., 2015), *top right*: the GO Tau disk (Long et al., 2018), *bottom left*: the TW Hya disk (Andrews et al., 2016), *bottom right*: the HD 163296 disk (Isella et al., 2016),

induced fragmentation, resulting in gaps and rings seen in dust continuum images. In this model, the locations of the gaps can be estimated from the disk temperature since the locations of condensation fronts are determined by the temperature. However, recent ALMA survey of disks in the Taurus star-forming region showed that the gap locations are not well correlated with the expected locations of major condensation fronts (Long et al., 2018).

1.3 Physical Structure of Protoplanetary Disks

The physical structure of the protoplanetary disks determines how planets form and evolve within it. In this section, we introduce the basics of the disk structure.

Protostar is formed by the gravitational collapse of a dense molecular cloud core. Although most of the core mass will be into the protostar, protoplanetary disk is also

formed around the protostar since the core has non-zero angular momentum. Basically, the protoplanetary disk can be regarded as geometrically thin disk, meaning that, in the almost entire region of the disk, the height above the mid-plane z can be assumed to be sufficiently smaller than the mid-plane distance from the central star r.

The vertical structure of the disk is determined by the equilibrium between the vertical pressure gradient force and the vertical gravitational force from the central star:

$$\frac{1}{\rho_{\rm g}}\frac{\partial p}{\partial z} = -\frac{GM_*}{r^3}z, \tag{1.1}$$

where $\rho_{\rm g}$ is the gas density, p is the pressure, G is the gravitational constant and M_* is the mass of the central star. By integrating Equation (1.1) with assuming the isothermal sound speed $c_{\rm s} = \sqrt{p/\rho_{\rm g}}$, we obtain the vertical gas density profile as

$$\rho_{\rm g} = \rho_0 \exp\left(-\frac{1}{2}\frac{z^2}{h_{\rm g}}\right), \tag{1.2}$$

where ρ_0 is the mid-plane gas density, $h_{\rm g} = c_{\rm s}/\Omega_{\rm K}$ is the pressure scale height with $\Omega_{\rm K}$ being the Keplerian frequency. If we assume a typical temperature profile for the disk, the ratio of $h_{\rm g}$ over r is less than ~ 0.1 which justifies the assumption of the geometrically thin disk.

With above analysis, let us move on to the one-dimensional (radial) evolution of the disk. For the one-dimensional analysis, It is useful to introduce the vertically integrated surface density

$$\Sigma_{\rm g}(r) = \int_{-\infty}^{\infty} \rho_{\rm g}(r, z){\rm d}z. \tag{1.3}$$

One of the most well known model for the surface density profile is the so-called Minimum Mass Solar Nebulae model (MMSN, Hayashi 1981);

$$\Sigma_{\rm g}(r) = 1700\left(\frac{r}{\rm au}\right)^{-3/2}\ {\rm g\ cm^{-2}}, \tag{1.4}$$

which is estimated from the mass distribution of current solar system.

Protoplanetary disks are thought to radially evolve by the angular momentum transport between the two neighboring annuli due to the viscosity ν. In protoplanetary disks, the viscosity is mainly originated from the large scale turbulent motion of gas not from the molecular viscosity. Although the origin of the turbulence in protoplanetary disks is still actively debated, there has been a helpful parameterization for the viscosity proposed by Shakura & Sunyaev (1973),

$$\nu = \alpha c_{\rm s} h_{\rm g}, \tag{1.5}$$

where the dimensionless parameter α describe how strong the turbulence is. This formulation is called as α-viscosity model. The radial drift velocity of the gas originated from the angular momentum transport due to the viscosity is written as (Lynden-Bell & Pringle, 1974)

$$v_{\rm vis}(r) = \frac{3}{\Sigma_{\rm g} r^{1/2}} \frac{\partial}{\partial r} \left(\Sigma_{\rm g} \nu r^{1/2} \right). \tag{1.6}$$

Once we know the radial drift velocity, we can calculate the time evolution of the gas surface density by considering the one-dimensional continuity equation for the axisymmetric disk

$$\frac{\partial \Sigma_{\rm g}}{\partial t} = -\frac{1}{r} \frac{\partial}{\partial r} \left(\Sigma_{\rm g} v_{\rm vis} r \right). \tag{1.7}$$

Combining Equation (1.6) and (1.7), we obtain the equation describing the time evolution of the surface density as

$$\frac{\partial \Sigma_{\rm g}}{\partial t} = \frac{3}{r} \frac{\partial}{\partial r} \left[r^{1/2} \frac{\partial}{\partial r} \left(\nu \Sigma_{\rm g} r^{1/2} \right) \right]. \tag{1.8}$$

Here, let us consider the steady state of the disk ($\partial/\partial t = 0$). From Equation (1.8), one can immediately see that $\nu\Sigma_{\rm g}$ is constant with radius in a steady state. If we assume power-law distributions of the gas surface density and the temperature as

$$\Sigma_{\rm g}(r) = \Sigma_{\rm g,0} \left(\frac{r}{\rm au} \right)^{-p}, \tag{1.9}$$

$$T(r) = T_0 \left(\frac{r}{\rm au} \right)^{-q}, \tag{1.10}$$

where $\Sigma_{\rm g,0}$ and T_0 are the surface density and the temperature at 1 au, respectively, the relation between p and q needs to satisfy $p + q = 3/2$ for $\nu\Sigma_{\rm g}$ to be constant.

With $\nu\Sigma_{\rm g}$ being constant with radius, Equation (1.6) can be rewritten into the simple form:

$$v_{\rm vis}(r) = -\frac{3}{2} \frac{\nu}{r}. \tag{1.11}$$

From this equation, the gas mass accretion rate onto the central star can be written as

$$\dot{M} = 2\pi r \Sigma_{\rm g} v_{\rm vis} \tag{1.12}$$

$$= 3\pi \Sigma_{\rm g} \nu. \tag{1.13}$$

It is also helpful to rewrite Equation (1.13) as

$$\Sigma_{\rm g} = \frac{\dot{M}}{3\pi\nu} = \frac{\dot{M}}{3\pi\alpha c_{\rm s} h_{\rm g}}. \tag{1.14}$$

Equation (1.14) shows that for a given mass accretion rate, stronger turbulence leads to lower gas surface density because the turbulence-induced viscosity easily transports the angular momentum of the gas.

1.4 Dust Dynamics in Protoplanetary Disks

In section 1.3, we described the basics of the structure of protoplanetary disks with focusing on the gas disk. Although the mass of the disk is composed almost entirely of the gas (≈ 99 %), the evolution of solid materials which constitutes only 1% of the mass of the disk is definitely important for both detemining the disk structure and understanding how planets form within the disk. In this section, we describe how dust particles behave in the gas disk.

The gas and dust particles in prtoplanetary disks have different rotational velocities since only the gas feels the pressure gradient force (Figure 1.5). Owing to the

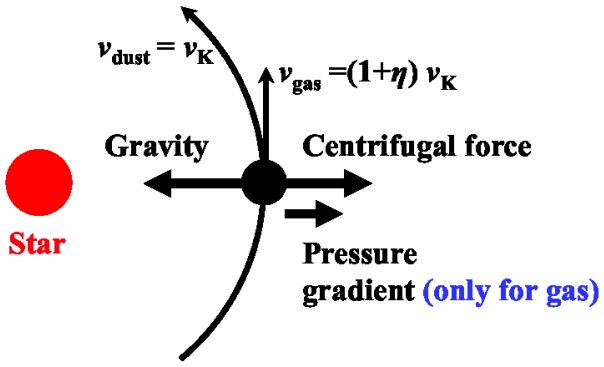

Figure 1.5: Schematic of the balance of forces acting on a dust particle and gas. The disk gas rotates with slightly smaller velocity than that of dust particles because the disk gas feel a outward pressure gradient force.

difference in the velocity, dust particles feel a drag force from the surrounding disk gas given by

$$\boldsymbol{F}_{\rm drag} = -\frac{m}{\tau_{\rm s}}\Delta v, \tag{1.15}$$

where m is the mass of the dust particle, Δv is the velocity of the dust particle relative to the gas. The stopping time $\tau_{\rm s}$ is defined as the momentum of the particle divided by the drag force acting on it and denote the degree of coupling between the dust particle and the gas. The stopping time is related to the dust radius a as

$$\tau_{\rm s} = \begin{cases} \dfrac{\rho_{\rm int} a}{\rho_{\rm g} v_{\rm th}}, & a < \dfrac{9\lambda_{\rm mfp}}{4} \quad \text{(Epstein regime)}, \\ \dfrac{\rho_{\rm int} a}{\rho_{\rm g} v_{\rm th}} \dfrac{4a}{9\lambda_{\rm mfp}}, & a > \dfrac{9\lambda_{\rm mfp}}{4} \quad \text{(Stokes regime)}, \end{cases} \tag{1.16}$$

where $\rho_{\rm int}$ is the dust internal density, $v_{\rm th} = \sqrt{8/\pi}c_{\rm s}$ is the thermal velocity of the gas and $\lambda_{\rm mfp}$ is the mean free path of gas molecules. It is also useful to introduce the so-called Stokes number which is the dimensionless stopping time defined as

$$\mathrm{St} \equiv \Omega_{\rm K}\tau_{\rm s}. \tag{1.17}$$

Let us consider the gas and dust motions in the cylindrical coordinate (r, ϕ, z). The dust and gas velocities are denoted as $\boldsymbol{v}_{\rm d} = (v_{\rm d,r}, v_{\rm d,\phi}, v_{\rm d,z})$ and $\boldsymbol{v}_{\rm g} = (v_{\rm g,r}, v_{\rm g,\phi}, v_{\rm g,z})$, respectively. The equations of motions for the dust particles are given by (e.g., Nakagawa et al. 1986)

$$\frac{\partial v_{\rm d,r}}{\partial t} + (\boldsymbol{v}_{\rm d}\cdot\nabla)\, v_{\rm d,r} - \frac{v_{\rm d,\phi}^2}{r} = -r\Omega_{\rm K}^2 - \frac{v_{\rm d,r} - v_{\rm g,r}}{\tau_{\rm s}}, \tag{1.18}$$

$$\frac{\partial v_{\rm d,\phi}}{\partial t} + (\boldsymbol{v}_{\rm d}\cdot\nabla)\, v_{\rm d,\phi} + \frac{v_{\rm d,r}v_{\rm d,\phi}}{r} = -\frac{v_{\rm d,\phi} - v_{\rm g,\phi}}{\tau_{\rm s}}, \tag{1.19}$$

$$\frac{\partial v_{\rm d,z}}{\partial t} + (\boldsymbol{v}_{\rm d}\cdot\nabla)\, v_{\rm d,z} = -\Omega_{\rm K}^2 z - \frac{v_{\rm d,z} - v_{\rm g,z}}{\tau_{\rm s}}, \tag{1.20}$$

and for the gas are

$$\frac{\partial v_{\rm g,r}}{\partial t} + \Big(\boldsymbol{v}_{\rm g}\cdot\nabla\Big)\, v_{\rm g,r} - \frac{v_{\rm g,\phi}^2}{r} = -\frac{1}{\rho_{\rm g}}\frac{\partial p}{\partial r} - r\Omega_{\rm K}^2 - \frac{\rho_{\rm d}}{\rho_{\rm g}}\frac{v_{\rm g,r} - v_{\rm d,r}}{\tau_{\rm s}}, \tag{1.21}$$

$$\frac{\partial v_{\rm g,\phi}}{\partial t} + \Big(\boldsymbol{v}_{\rm g}\cdot\nabla\Big)\, v_{\rm g,\phi} + \frac{v_{\rm g,r}v_{\rm g,\phi}}{r} = -\frac{\rho_{\rm d}}{\rho_{\rm g}}\frac{v_{\rm g,\phi} - v_{\rm d,\phi}}{\tau_{\rm s}}, \tag{1.22}$$

$$\frac{\partial v_{\rm g,z}}{\partial t} + \Big(\boldsymbol{v}_{\rm g}\cdot\nabla\Big)\, v_{\rm g,z} = -\frac{1}{\rho_{\rm g}}\frac{\partial p}{\partial z} - \Omega_{\rm K}^2 z - \frac{\rho_{\rm d}}{\rho_{\rm g}}\frac{v_{\rm g,z} - v_{\rm d,z}}{\tau_{\rm s}}, \tag{1.23}$$

here we assume $z \ll r$. If we consider a steady state ($\partial/\partial t = 0$) of an azimuthally symmetric disk ($\partial/\partial\phi = 0$) and $\rho_{\rm d} \ll \rho_{\rm g}$, Equation (1.21) yields

$$\frac{v_{\rm g,\phi}^2}{r} = \frac{1}{\rho_{\rm g}}\frac{\partial p}{\partial r} + r\Omega_{\rm K}^2. \tag{1.24}$$

From Equation (1.24), we obtain the rotational velocity of the gas as

$$v_{\rm g,\phi} \approx (1-\eta)v_{\rm K}, \tag{1.25}$$

where

$$\eta \equiv -\frac{1}{2}\left(\frac{c_{\rm s}}{v_{\rm K}}\right)^2 \frac{\partial \ln p}{\partial \ln r}. \tag{1.26}$$

Equations (1.25) and (1.26) show that if the gradient in the radial pressure profile is negative, the disk gas rotates with the sub-Keplerian velocity. In contrast, if the

gradient in the radial pressure profile is positive, the disk gas rotates with the super-Keplerian velocity. Basically, the radial pressure gradient is negative in most of the region of protoplanetary disks since the inner region tends to have higher temperature and higher density than the outer region. Owing to the sub-Keplerian motion of the gas, dust particles feel a head wind from the surrounding disk gas and radially drift. By assuming $|v_{\rm d,r}|$, $|v_{\rm d,\phi} - v_{\rm K}|$, $|v_{\rm d,z}| \ll v_{\rm K}$, the radial drift velocity of dust $v_{\rm d,r}$ can be obtained from Equations (1.18) and (1.19) as

$$v_{\rm d,r} \approx -\frac{\rm St}{1+{\rm St}^2} 2\eta v_{\rm K} \tag{1.27}$$

Although we ignore the feed back from dust to gas in the above analysis by assuming $\rho_{\rm d} \ll \rho_{\rm g}$, the feedback could be important when dust particles are locally accumulated (e.g., Kretke et al. 2009). If we accurately consider the feed back from dust to gas, the radial drift velocity of dust and gas are given as (Kanagawa, Ueda, Muto, Okuzumi 2017)

$$v_{\rm d,r} = -\frac{\rm St}{{\rm St}^2+(1+\epsilon)^2} 2\eta v_{\rm K} + \frac{1+\epsilon}{{\rm St}^2+(1+\epsilon)^2} v_{\rm vis}, \tag{1.28}$$

$$v_{\rm g,r} = \frac{{\rm St}\epsilon}{{\rm St}^2+(1+\epsilon)^2} 2\eta v_{\rm K} + \left\{1 - \frac{(1+\epsilon)\epsilon}{{\rm St}^2+(1+\epsilon)^2}\right\} v_{\rm vis} \tag{1.29}$$

where, ϵ is the dust-to-gas density ratio. The first term in Equation (1.28) is the radial drift velocity with respect to the gas, which is basically same as Equation (1.27) except for the feedback effect. The second term (1.28) is a drag term comes from the radial motion of the gas. The radial motion of the gas can directly drag the dust particles radially since they are somewhat coupled with the gas. If we consider the feedback from dust to gas, the radial drift velocity of dust particles decreases with increasing ϵ.

An interesting feature in Equations (1.28) and (1.29) is the outward motion of the gas. Figure 1.6 shows the radial drift velocities of the gas and dust particle with fully including the feedback from dust to gas. Although dust particles always has a negative value (drift inward), the gas moves outward when the Stokes number is ~ 1 and $\alpha < 10^{-3}$. This is because the gas gain the angular momentum from the inwardly drifting dust particles. This implies that dust particles potentially change the gas disk structure even though they constitute only 1% of the disk mass (Gonzalez et al. 2017, Kanagawa, Ueda, Muto, Okuzumi 2017).

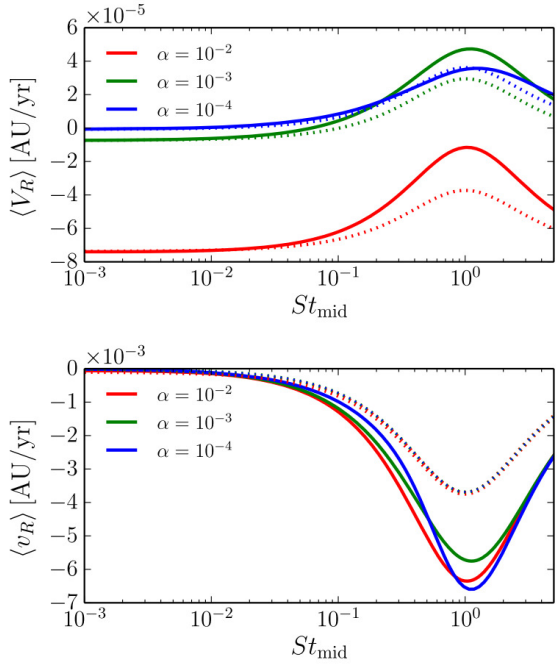

Figure 1.6: Radial drift velocities of gas (top) and dust particles (bottom) at $r = 10$ au with assuming $h_{\rm g}/r = 0.05$ and $\Sigma_{\rm d}/\Sigma_{\rm g} = 0.01$. The solid and dashed lines denote the velocities obtained from the three-dimensional and two-dimensional (vertically integrated) analysis, respectively. The Stokes number is defined by the value at the mid-plane. Figure is taken from Kanagawa, Ueda, Muto, Okuzumi (2017).

1.5 Difficulties in Planetesimal Formation

In order for dust particles to grow to planets, they first have to form kilometer-sized bodies called as planetesimals. However, it is known that there are some barriers in planetesimal formation. In this section, we explain why the planetesimal formation is a severe problem in planet formation.

1.5.1 Radial drift barrier

The first barrier is the so-called radial drift barrier. As described in the previous section, dust particles feel a head wind from the surrounding disk gas. Owing to the head wind, dust particles lose angular momentum and eventually spiral into the central star before they grow large enough (Weidenschilling, 1977).

Let us estimate the drift timescale and the growth timescale of dust particles. By using Equation (1.27), the drift timescale is defined as

$$\tau_{\rm drift} = \frac{r}{|v_{\rm d,r}|} = \frac{1}{2\eta}\frac{1+{\rm St}^2}{\rm St}\frac{1}{\Omega_{\rm K}}. \tag{1.30}$$

From Equation (1.30), we see that the drift timescale is minimum at St = 1. In order for the dust particles to grow, the drift timescale needs to be sufficiently larger than the growth timescale of the dust particles. The growth timescale is defined as

$$\tau_{\rm grow} = \frac{m}{4\pi\rho_{\rm d,0}a^2\Delta v_{\rm pp}\epsilon_{\rm stick}}, \tag{1.31}$$

where $\rho_{\rm d,0}$ is the mid-plane dust density, $\Delta v_{\rm pp}$ is the relative velocity between the colliding particles and $\epsilon_{\rm stick}$ is the sticking efficiency (< 1). In the inner region of protoplanetary disks, the relative velocity is mainly determined by the turbulence. If ${\rm St} \sim 1$, the relative velocity originating from the turbulence can be written as $\Delta v_{\rm pp} = \sqrt{3\alpha{\rm St}}c_{\rm s}$ (Ormel & Cuzzi, 2007). The mid-plane dust density can be estimated as $\Sigma_{\rm d}/\sqrt{\pi}h_{\rm d}$ with $h_{\rm d}$ being the scale height of the dust disk given as (Dubrulle et al., 1995; Youdin & Lithwick, 2007)

$$h_{\rm d} \approx h_{\rm g}\left(1+\frac{\rm St}{\alpha}\right)^{-1/2}, \tag{1.32}$$

Using these equations, the growth timescale can be rewritten as a simple form:

$$\tau_{\rm grow} \approx \frac{0.3}{\epsilon_{\rm stick}}\frac{\Sigma_{\rm g}}{\Sigma_{\rm d}}\frac{1}{\Omega_{\rm K}}. \tag{1.33}$$

From Equations (1.30) and (1.33), we obtain

$$\frac{\tau_{\rm drift}}{\tau_{\rm grow}} = \frac{\epsilon_{\rm stick}}{0.3\eta}\frac{\Sigma_{\rm d}}{\Sigma_{\rm g}}, \tag{1.34}$$

here we assume St = 1. If we consider the MMSN disk with the temperature profile of $T = 280(r/{\rm au})^{-1/2}$ K, Equation (1.34) yields

$$\frac{\tau_{\rm drift}}{\tau_{\rm grow}} = 10\left(\frac{\epsilon_{\rm stick}}{0.5}\right)\left(\frac{\Sigma_{\rm d}/\Sigma_{\rm g}}{0.01}\right)\left(\frac{r}{\rm au}\right)^{-1/2}. \tag{1.35}$$

Equation (1.35) shows that the radial drift barrier is more severe in the outer region. If the sticking efficiency is close to unity, the radial drift barrier would not be a severe problem in the inner region of the disk. However, as we will discuss in next section, the sticking efficiency of rocky grains would be much lower than unity and potentially has a negative value. In that case, the dust particles would be depleted from the protoplanetary disks by the radial drift. It should be noted that the growth timescale $\tau_{\rm grow}$ we defined is a mass-doubling timescale, which means that in order for dust particles to grow to planetesimals, $\tau_{\rm drift}$ has to be sufficiently larger than $\tau_{\rm grow}$.

1.5.2 Fragmentation barrier

The second barrier is the so-called fragmentation barrier: dust particles cannot stick to each other but fragment into small particles at a typical collisional velocity in protoplanetary disks.

Figure 1.7 shows the typical collisional velocity of dust particles as a function of its radius. In the inner region of protoplanetary disks where we focus on, the collisional velocity of dust particles is governed by the relative velocity originated from the disk turbulence except for the very early stage of their growth. The collisional velocity reaches a maximum at where the dust radius is $\sim$ 10–100 cm (corresponding to St $\sim$ 1) and the maximum value is an order of $\sim$ 100 m s^{-1}.

If the collisional velocity is higher than a critical fragmentation velocity, dust particles cannot stick to each other but fragment into small particles, meaning that the collision does not contribute to the growth of dust particles. The critical fragmentation velocity have been studied by both numerical simulations (e.g., Wada et al. 2013) and laboratory experiments (e.g., Blum & Wurm 2000). Figure 1.8 shows the maximum aggregate size in the outcome of the aggregate collisons as a function of the impact energy (Wada et al., 2008). We can see that if the impact energy is high, the collision results into the fragmentation which results into a negative sticking efficiency. In Figure 1.8, the critical impact energy is $E_{\rm imp} \sim 10 n_{\rm k} E_{\rm break}$ for silicate

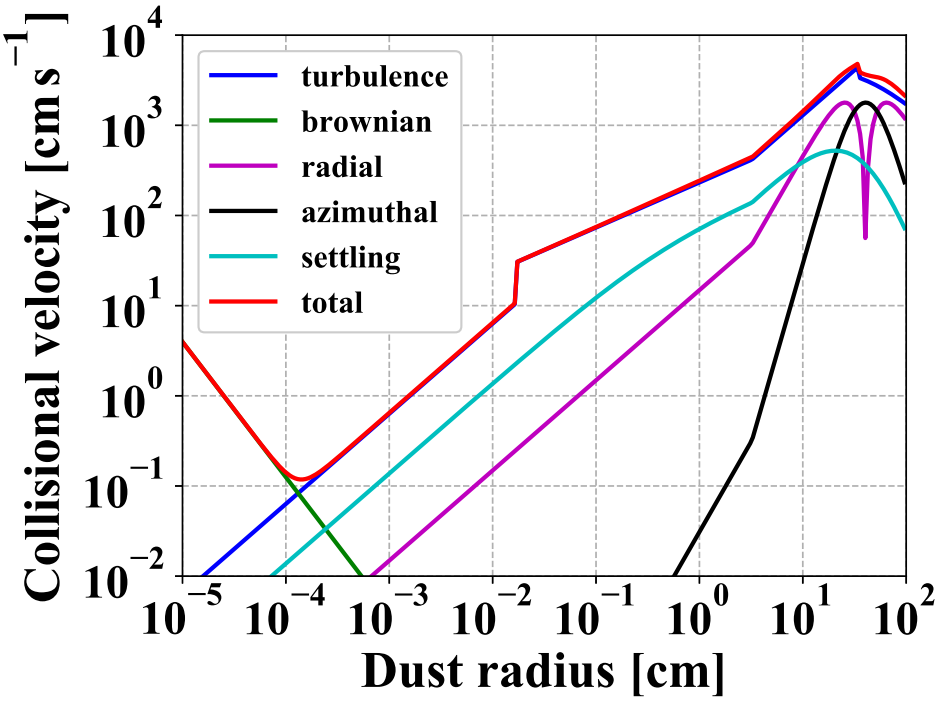

Figure 1.7: Collisional velocity of dust particles at 1 au in the MMSN disk. Different lines correspond to different origins of the relative velocity. The turbulence strength parameter α is set to be 10^{-3}. The collision is assumed to be between particles with a size ratio of two.

aggregates, which corresponds to the critical fragmentation velocity of 3.4 m s^{-1} with a monomer radius of 0.1 μm.

The exact value of the critical fragmentation velocity depends on both the monomer radius and the chemical composition of the dust particle. If the monomer radius is 0.1 μm, which is a typical size of dust particles in the interstellar medium, the critical fragmentation velocities for rocky and icy grains are estimated to be $\sim$ 8 m s^{-1} and $\sim$ 80 m s^{-1}, respectively (e.g., Wada et al. 2013). The dust fragmentation is much more severe for rocky particles because rocky particles are less sticky than icy ones. These fact suggests that dust particles are easy to fragment at a typical collisional velocity in protoplanetary disks and cannot grow beyond the radius of $\sim$ 10 cm. Since the critical fragmentation velocity is almost inversely proportional to the radius of monomer particle (Chokshi et al., 1993), the fragmentation barrier could be solved if the monomer radius is sufficiently small (Arakawa & Nakamoto, 2016). However, it is unclear that such very small particles exist enough in protoplanetary disks.

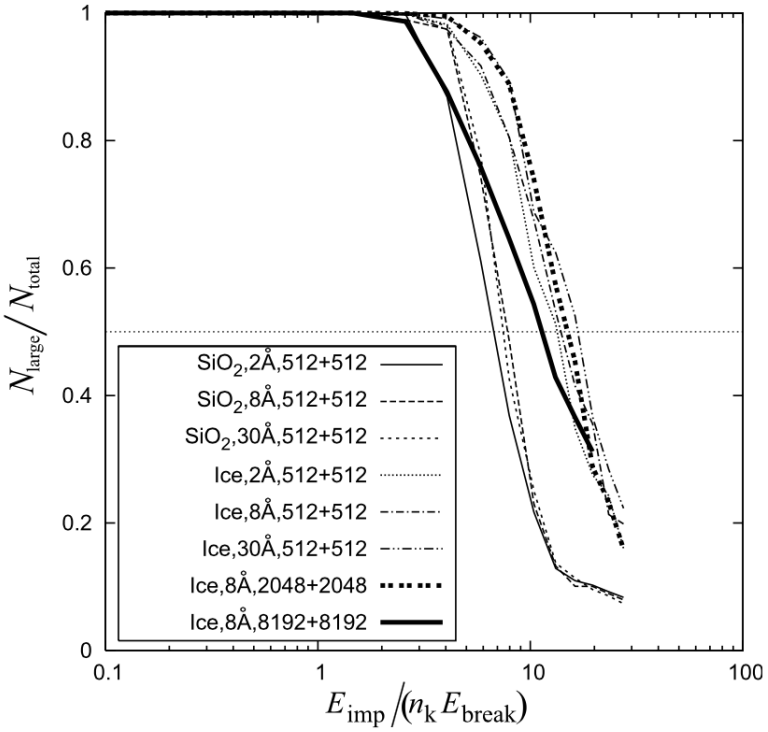

Figure 1.8: Ratio of the number of particles in the largest fragment, $N_{\rm large}$, to the total number of particles, $N_{\rm total}$, as a function of the impact energy $E_{\rm imp}$ obtained from the numerical simulations of aggregate collisons. $N_{\rm large}/N_{\rm total} = 0.5$ corresponds to the collision with no net mass growth. The figure is taken from Wada et al. (2008).

1.6 Inner Edge of the Dead Zone

As mentioned in section 1.5, planetesimal formation via the collisional growth of dust particles is difficult due to rapid radial drift and fragmentation of dust particles. Especially for rocky one, the fragmentation barrier is a severe problem.

1.6.1 Dead zone in protoplanetary disks

One of the solutions to form rocky planetesimals is a dust-pileup followed by the gravitational clumping of the dust layer. As mentioned in section 1.4, if the disk has a local maximum in the radial pressure profile, the inward drift of dust particles is halted and it leads to the local enhancement of the dust-to-gas mass ratio. If the dust-to-gas mass ratio is sufficiently high, the streaming instability is triggered and potentially forms rocky planetesimals via the gravitational force (Youdin & Goodman, 2005; Johansen et al., 2007; Carrera et al., 2015).

One preferential location where the local pressure maximum originates is the inner edge of the so-called dead zone (e.g., Dzyurkevich et al. 2010; Flock et al. 2016). The dead zone is the location where magneto-rotational instability (MRI, Balbus & Hawley 1998) is suppressed because of poor gas ionization (Gammie, 1996).

Figure 1.9 shows the schematic of the turbulent state in the protoplanetary disks. Whether MRI is active or not is determined by the ionization degree of the disk gas.

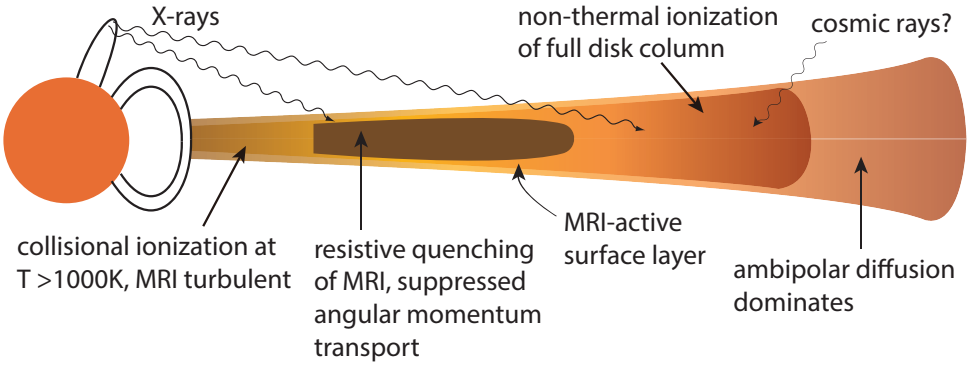

Figure 1.9: Schematic of the dead zone in the protoplanetary disk, taken from Armitage (2011)

If the ionization degree is too low for the gas to be coupled with the magnetic fields, MRI does not occur and the turbulent viscosity arising from MRI is vanished. The gas in protoplanetary disk is thought to be ionized by some mechanisms. In the very inner region of disks, the disk gas is ionized owing to its high temperature. If the gas temperature is higher than $\sim$ 1000 K, the collisional ionization of gas-phase alkali elements such as potassium generate free electrons and ions, which is enough for MRI to operate (e.g., Desch & Turner 2015). In the outer region where the disk surface density is low, the gas is ionized by FUV, X-rays and cosmic rays. However, FUV, Xrays and cosmic rays are attenuated by the column densities of ~ 0.1 g cm^{-2}, $\sim$ 10 g cm^{-2} and $\sim$ 100 g cm^{-2}, respectively (e.g., Umebayashi & Nakano 1981; Perez-Becker & Chiang 2011; Ercolano & Glassgold 2013). As a result, in the midplane of the middle part of the disk, both the thermal and non-thermal ionization are not efficient, leading to the suppression of MRI.

Figure 1.10 shows the radial profile of the turbulence strength parameter α obtained from the recent magneto-hydrodynamical simulation (Flock et al., 2017). We clearly see that across the dead zone inner edge, the turbulent viscosity steeply decreases from inside out because of the suppression of MRI.

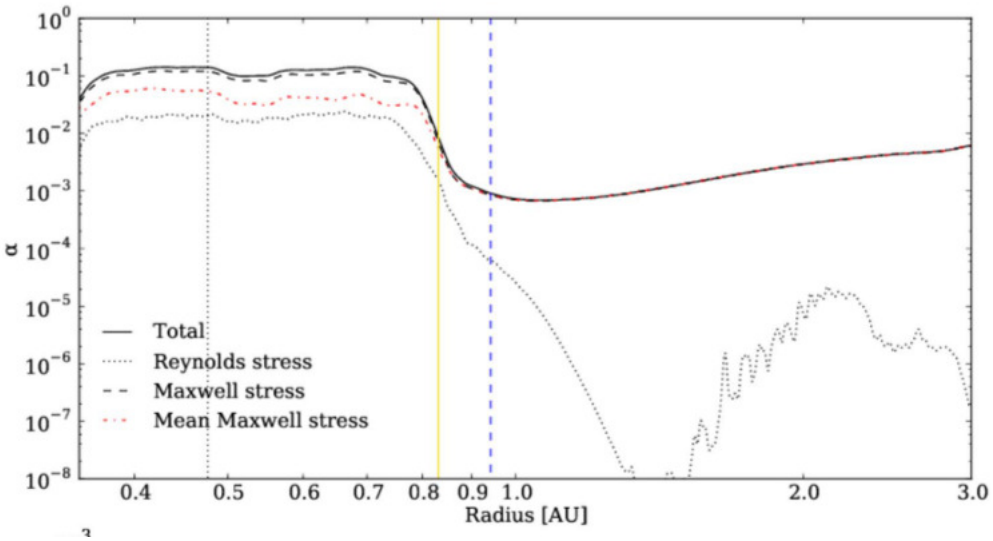

Figure 1.10: Radial profile of the turbulence strength parameter α obtained from the three-dimensional non-ideal magneto-hydrodynamical simulations. The black solid line denotes the turbulence strength parameter α which is determined by the sum of the Reynolds stress (black dotted line) and Maxwell stress (black dashed line). The dead-zone inner edge and the local pressure maximum are denoted by the vertical yellow solid line and blue dashed line, respectively. The figure is taken from Flock et al. (2017).

1.6.2 Dust-trapping at the inner edge of the dead zone

From the above discussion, the inner edge of the dead-zone can be defined as a radial location where the gas temperature reaches $\sim$ 1000 K. Across the dead zone inner edge, the turbulent viscosity arising from MRI steeply decreases from inside out. As Equation (1.14) shows, gas surface density increases with decreasing the turbulence viscosity. This implies that around the dead-zone inner edge, the gas surface density has a positive radial gradient, which results into a local maximum in the radial pressure profile.

Figure 1.11 shows the schematic of the dust-trapping at a radial pressure maximum. Basically, the disk gas has a negative pressure gradient in radial direction and rotates with the sub-Keplerian velocity. Since the dust particles feel a head wind from the surrounding disk gas, the dust particles lose angular momentum and radially drift inward. However, around the dead-zone inner edge, the positive gradient in the radial surface density profile owing to the decrease in the turbulence strength leads to the positive gradient in the radial pressure profile. In the positive pressure gradient region, the gas rotates with the super-Keplerian velocity, so the dust particles receive

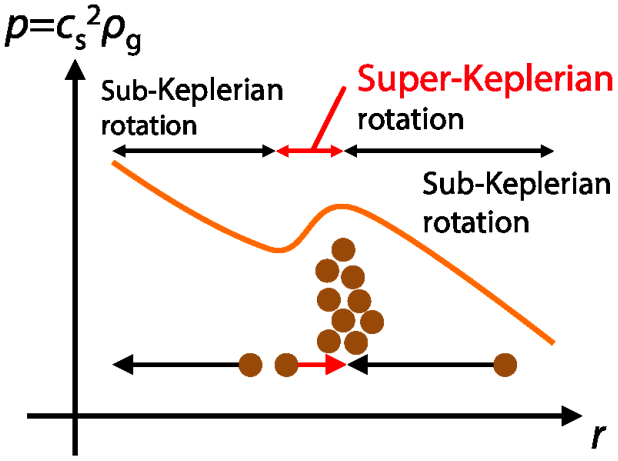

Figure 1.11: Schematic of the dust-trapping at a radial pressure maximum. The disk gas rotates with the super-Keplerian velocity at just inside of a pressure maximum, which leads to the outward drift of dust particles.

the angular momentum from the gas and drift outward (Whipple 1972; Adachi et al. 1976). Therefore the dust particles would pileup on the dead-zone inner edge.

There have been many studies related to the dust-pileup at the dead-zone inner edge (e.g., Brauer et al. 2008; Kretke et al. 2009; Dzyurkevich et al. 2010; Pinilla et al. 2016). Kretke et al. (2009) demonstrated that the dust particles indeed pileup on the dead-zone inner edge by performing the simulations of dust and gas disk evolution. However, Kretke et al. (2009) ignored the effect of the dust fragmentation. As mentioned in section 1.5.2, the fragmentation must regulate growth of dust particles and it would significantly affect the behavior of dust motion in the gas.

There are also some studies on the dust-pileup at the dead-zone inner edge originating from the non-thermal ionization helped by the inner cavity of the gas disk due to disk wind (e.g., Pinilla et al. 2016) or by the ice sublimation (e.g., Brauer et al. 2008; Drążkowska et al. 2013). Although these inner edges of the dead-zone would be preferable for icy planetesimal formation, it does not account for the formation of rocky planetesimals since these edges are located at the outer region of the disk where icy particles exist.

Although the most of these previous works focused on only the theoretical modeling of the planetesimal formation, the dust-pileup at the dead-zone inner edge would be a interesting subject even for the observational aspects. As we see in section 1.2, many disks have interesting substructures in the outer region where we can currently observe. Future telescopes and interferometer instruments will reveal the detailed

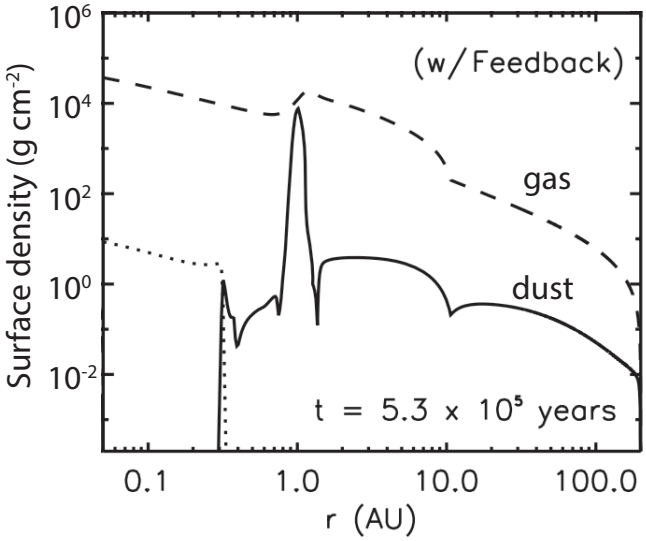

Figure 1.12: Dust-trapping at the dead-zone inner edge located at 1 au around an intermediate-mass star. The figure is taken from Kretke et al. (2009).

structure of the innre region of the disks. For example, VLTI/MATISSE instrument will allow us to image the inner region of protoplanetary disks at mid-infrared wavelengths with high angular resolution ($\sim$ 5 mas in L-band, e.g., Lopez et al. 2014), which will provide us opportunities to directly compare the theoretical models of the dead-zone inner edge with the observations. Hence, modeling of the dead-zone inner edge aiming at the comparison with observations must be important to understand the rocky planetesimal formation.

1.7 About this thesis

This thesis focuses on the formation of rocky planetesimals at the innermost region of protoplanetary disks. As described above, collisional growth of dust particles is halted by both rapid radial drift and fragmentation of the dust particles. The dead-zone inner edge located at the innermost region of the disk is a preferential site for rocky planetesimal formation because it traps dust particles drifting from the outer region, leading to the rocky planetesimal formation via the gravitational force.

In chapter 2, we analytically investigate the temperature structure of the innermost region of passively heated protoplanetary disks. Since the dead-zone inner edge is characterized as a radial position where the gas temperature reaches $\sim$ 1000 K, the temperature structure of the innermost region of disks is important to understand the

planetesimal formation at the dead-zone inner edge. This chapter is based on Ueda, Okuzumi, Flock 2017.

In chapter 3, we investigate the dust-pileup at the dead-zone inner edge around a Herbig Ae star by performing simulations of the dust and gas disk evolution. We show how the total mass of planetesimals formed at the dead-zone inner edge depends on the strength of turbulence and the critical fragmentation velocity. Based on the results, we analytically derive the condition for the dust-pileup to operate at the dead-zone inner edge. Furthermore, using the radiative transfer code RADMC-3D, we examine the effect of the dust-pileup on the temperature structure and the disk appearance. We show that the dust-pileup casts a shadow on the disk surface and it significantly changes the disk temperature structure. This chapter is based on Ueda, Flock, Okuzumi accepted for for publication in ApJ.

In chapter 4, we apply the above simulations to the disk around a Sun-like star to verify the hypothesis that building blocks of the inner solar system planets formed at the dead-zone inner edge. We show that planetesimal distribution invoked from the current dynamical configuration of inner solar system planets can be reproduced by the planetesimal formation at the dead-zone inner edge.

Chapter 5 summarizes our findings and discusses future prospects of this thesis.

Chapter 2

Analytic Expressions for the Inner-Rim Structure of Passively Heated Protoplanetary Disks

Modified from Ueda, Okuzumi & Flock 2017b, ApJ, 843, 49

2.1 Abstract of this Chapter

We analytically derive the expressions for the structure of the inner region of protoplanetary disks based on the results from the recent hydrodynamical simulations. The inner part of a disk can be divided into four regions: dust-free region with gas temperature in the optically thin limit, optically thin dust halo, optically thick condensation front and the classical optically thick region in order from the inside. We derive the dust-to-gas mass ratio profile in the dust halo using the fact that partial dust condensation regulates the temperature to the dust evaporation temperature. Beyond the dust halo, there is an optically thick condensation front where all the available silicate gas condenses out. The curvature of the condensation surface is determined by the condition that the surface temperature must be nearly equal to the characteristic temperature $\sim$ 1200 K. We derive the mid-plane temperature in the outer two regions using the two-layer approximation with the additional heating by the condensation front for the outermost region. As a result, the overall temperature profile is step-like with steep gradients at the borders between the outer three regions. The borders might act as planet traps where the inward migration of planets due to gravitational interaction with the gas disk stops. The temperature at the border between the two outermost regions coincides with the temperature needed to activate magnetorotational instability, suggesting that the inner edge of the dead zone must lie at this border. The radius of the dead-zone inner edge predicted from our solution is $\sim$ 2–3 times larger than that expected from the classical optically thick temperature.

2.2 Introduction of this Chapter

The inner region of protoplanetary disks is the birthplace of rocky planetesimals and planets. One preferential site of rocky planetesimal formation is the inner edge of the so-called dead zone (e.g., Kretke et al. 2009). The dead zone is the location where magneto-rotational instability (MRI, Balbus & Hawley 1998) is suppressed because of poor gas ionization (Gammie, 1996). In the inner region of protoplanetary disks, the dead zone is likely to have an inner edge where the gas temperature T reaches ~1000 K, above which thermal ionization of the gas is effective enough to activate MRI (Gammie 1996, Desch & Turner 2015). Across the dead zone inner edge, the turbulent viscosity arising from MRI steeply decreases from inside out, resulting in a local maximum in the radial profile of the gas pressure (e.g., Dzyurkevich et al. 2010, Flock et al. 2016, Flock et al. 2017). The pressure maximum traps solid particles (Whipple 1972, Adachi et al. 1976) and may thereby facilitate dust growth (Brauer et al. 2008, Testi et al. 2014) and in-situ planet formation (Tan et al., 2015). The dead zone edge may even trap planets by halting their inward migration (Masset et al., 2006). Because the location of the dead zone inner edge is determined by the gas temperature, understanding the temperature structure is important to understand rocky planetesimal formation as well as the orbital architecture of inner planets.

The temperature structure of the innermost regions of protoplanetary disks has been extensively studied in the context of their observational appearance (see Dullemond & Monnier 2010 for review, and also Natta et al. 2001; Dullemond et al. 2001a; Isella & Natta 2005). Recently, Flock et al. (2016) performed the radiation hydrodynamical calculations of the the inner rim structures of disks around Herbig Ae stars taking into account the effects of starlight and viscous heating, evaporation and condensation of silicate grains and gas opacity. They found that the inner disk consists of four distinct zones with different temperature profiles. According to their results, the dead zone inner edge occurs at the border between two outermost regions, where the temperature drops steeply across 1000 K. Thus, this complex temperature structure potentially influences where rocky planetesimals and planets preferentially form. However, there has been no simple analytic model that reproduces the entire structure of the temperature profile. In addition, because Flock et al. (2016) performed simulations only for the disks around Herbig Ae stars, it has been unclear how the inner rim structures depend on stellar parameters.

In this study, we analytically derive the temperature and dust-to-gas mass ratio profile for the inner region of disks and reveal how these structures depend on the

central star parameters based on the results from Flock et al. (2016). Our analysis and the analytic solutions are showed in Section 2.3. We discuss the implications for the planetesimal and planet formation and the disk observation in Section 2.4. The summary is in Section 2.5.

2.3 Analytic Solutions for the Inner Rim Structure

We derive analytic expressions for the inner rim structure of protoplanetary disks based on the recent numerical simulations conducted by Flock et al. (2016). They found that the inner region of protoplanetary disks can be divided into four regions (region A, B, C and D) in terms of the temperature profile. Figure 2.1 schematically

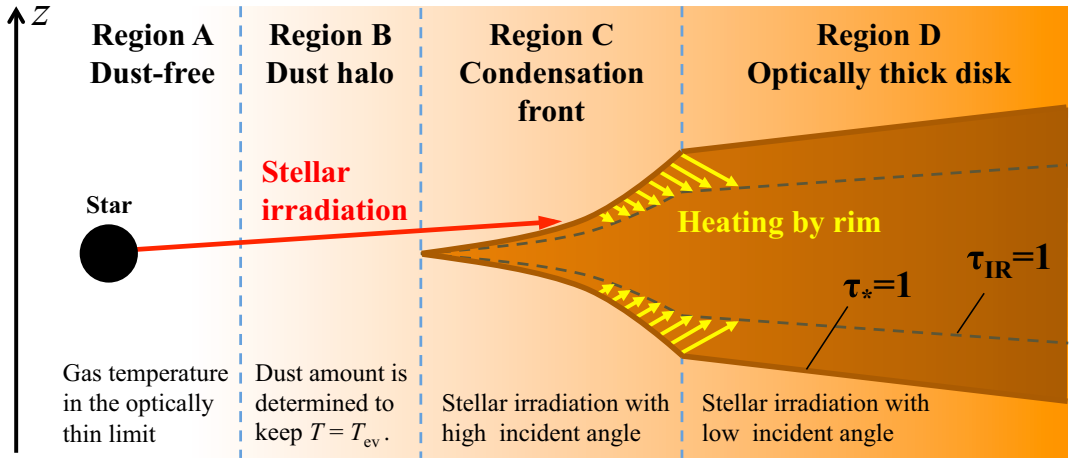

Figure 2.1: Schematic illustration of the inner structure of a passively irradiated protoplanetary disk. The disk received the starlight on the surface where the visual optical depth τ_* measured along the starlight reaches unity (solid curve), and receives the reprocessed light from the $\tau_* = 1$ surface on the deeper surface where the infrared optical depth $\tau_{\rm IR}$ measured vertically (z-direction) from above reaches unity (dashed curve). The inner region can be divided into four regions (region A, B, C and D). Region A: optically thin dust-free region; Region B: optically thin dust halo region where the temperature is nearly equal to the evaporation temperature; Region C: optically thick dust condensation front irradiated by the central star with high incident angle; Region D: optically thick disk illuminated by not only the central star but also dust condensation front.

shows the inner region of protoplanetary disks. In the following subsections, we describe how the structures such as the temperature and the dust-to-gas mass ratio are determined in each region.

2.3.1 Region A: Optically thin dust-free region

Region A is the innermost region where the temperature is above the evaporation temperature of dust. This region is therefore free of dust and is optically thin to the starlight. In an optically thin region, the temperature profile is generally given by

$$T = \epsilon^{-1/4} \left(\frac{R_*}{2r} \right)^{1/2} T_*, \tag{2.1}$$

where r is the distance from the central star, and R_* and T_* are the stellar radius and temperature, respectively. The dimensionless quantity ϵ is the ratio between the emission and absorption efficiencies of the disk gas including the contribution from dust,

$$\epsilon \equiv \frac{\kappa_{\rm g} + f_{\rm d2g} \kappa_{\rm d}(T)}{\kappa_{\rm g} + f_{\rm d2g} \kappa_{\rm d}(T_*)}, \tag{2.2}$$

where $f_{\rm d2g}$ is the dust-to-gas mass ratio, $\kappa_{\rm g}$ is the Planck mean gas opacity (here assumed to be independent of the temperature), and $\kappa_{\rm d}(T_*)$ and $\kappa_{\rm d}(T)$ are the Planck mean dust opacities at the stellar and disk temperatures, respectively. Flock et al. (2016) adopted $\kappa_{\rm g} = 10^{-4}$ cm^2 g^{-1}, $\kappa_{\rm d}(T_*) = 2100$ cm^2 g^{-1} and $\kappa_{\rm d}(T) = 700$ cm^2 g^{-1}.

For region A, $\epsilon \approx 1$ because $f_{\rm d2g} \approx 0$. Therefore, the temperature profile in region A, $T_{\rm A}$, is given by

$$T_{\rm A} = \left(\frac{R_*}{2r} \right)^{1/2} T_*. \tag{2.3}$$

Flock et al. (2016) showed that Equation (2.3) accurately reproduces the temperature profile in region A (see the top panel of their Figure 1). The real gas temperature might be more difficult to understand because it depends on gas opacity (Dullemond & Monnier 2010, Hirose 2015), which is assumed to be independent on wavelength in this study.

2.3.2 Region B: Optically thin dust halo region

Region B is the location where dust starts to condense but is still optically thin. This region, which Flock et al. (2016) called the dust halo, has a uniform temperature that is nearly equal to the evaporation temperature $T_{\rm ev}$ (see Figure 1 of Flock et al. (2016)). These features can be understood by noting that the condensing dust acts as a thermostat: if T falls below $T_{\rm ev}$, dust starts to condense, but the condensed dust acts to push the temperature back up because the emission-to-absorption ratio ϵ of the dust is lower than that of the gas. Thus, dust evaporation and condensation regulate the temperature in this region to $\sim T_{\rm ev}$. Strictly speaking, the temperature of region

B obtained by Flock et al. (2016) is higher than $T_{\rm ev}$ by about 100 K. However, this is due to their numerical treatment of the dust evaporation, where the dust-to-gas ratio is given by a smoothed step function of T with the smoothing width of 100 K.

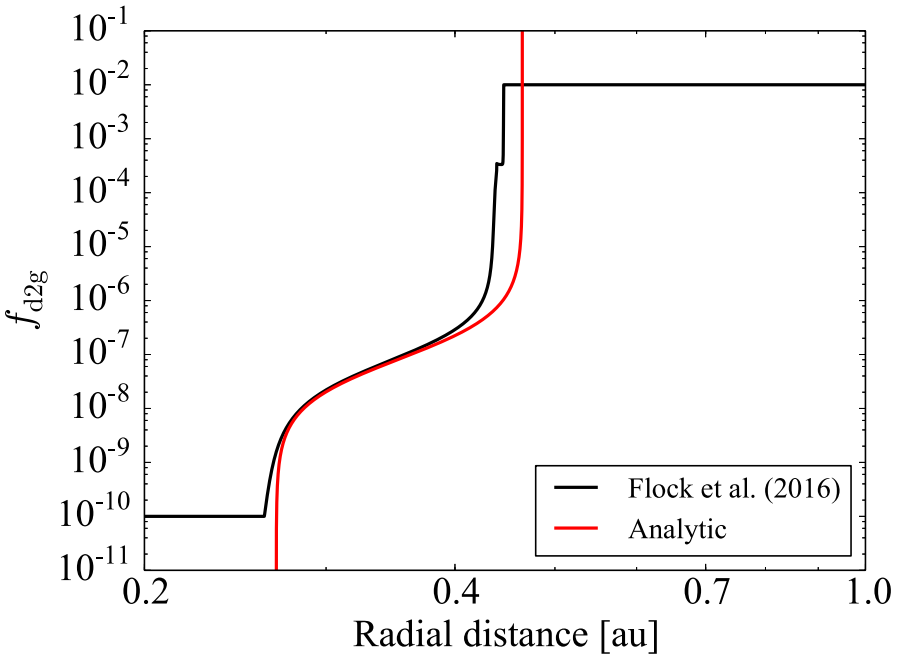

Figure 2.2: Dust-to-gas mass ratio profile $f_{\rm d2g}$ at the midplane in region B. The red and black solid lines show our analytic solution (Equation (2.4)) and the radiation hydrostatic disk model S100 of Flock et al. (2016) with the highest resolution, respectively.

The fact that $T \sim T_{\rm ev}$ in region B can be used to predict the spatial distribution of the dust-to-gas mass ratio $f_{\rm d2g}$ in this region. Substituting Equation (2.2) into Equation (2.1) and solving the equation with respect to $f_{\rm d2g}$, we obtain

$$f_{\rm d2g} = \frac{\kappa_{\rm g}(4r^2T_{\rm B}^4 - R_*^2T_*^4)}{\kappa_{\rm d}(T_*)R_*^2T_*^4 - 4\kappa_{\rm d}(T_{\rm B})r^2T_{\rm B}^4}, \tag{2.4}$$

where $T_{\rm B}$ stands for the temperature in region B. Assuming that $T_{\rm B}$ is constant, Equation (2.4) determines $f_{\rm d2g}$ as a function of r. Figure 2.2 compares Equation (2.4) with the radial profile of $f_{\rm d2g}$ at the midplane taken from the radiation hydrostatic disk model S100 of Flock et al. (2016, see the bottom panel of their Figure 1. The stellar temperature, radius, mass and luminosity are set to $T_* = 10000\,{\rm K}$, $R_* = 2.5R_\odot = 0.0116\,{\rm au}$, $M_* = 2.5M_\odot$ and $L_* = 56L_\odot$, respectively. See also their Table 1 for details). Equation (2.4) perfectly reproduces the result of Flock et al. (2016)

when $T_{\rm B}$ is set to $T_{\rm ev}$ + 100 K $\approx$ 1470 K, where we have used that $T_{\rm ev}$ in region B is $\approx$ 1370 K in their calculation.

As we can see from Figure 2.2, the inner and outer edges of region B correspond to the locations where $f_{\rm d2g}$ given by Equation (2.4) goes to zero and infinity, respectively. The radii of these locations are given by

$$\begin{aligned} R_{\rm AB} &= \frac{1}{2}\left(\frac{T_*}{T_{\rm B}}\right)^2 R_* \\ &= 0.27\left(\frac{T_*}{10^4\,{\rm K}}\right)^2\left(\frac{T_{\rm B}}{1470\,{\rm K}}\right)^{-2}\left(\frac{R_*}{2.5R_\odot}\right)\,{\rm au} \end{aligned} \tag{2.5}$$

and

$$\begin{aligned} R_{\rm BC} &= \frac{1}{2}\left(\frac{\kappa_{\rm d}(T_*)}{\kappa_{\rm d}(T_{\rm B})}\right)^{1/2}\left(\frac{T_*}{T_{\rm B}}\right)^2 R_* \\ &= 0.46\left(\frac{\kappa_{\rm d}(T_*)/\kappa_{\rm d}(T_{\rm B})}{3}\right)^{1/2}\left(\frac{T_*}{10^4\,{\rm K}}\right)^2 \\ &\quad\times\left(\frac{T_{\rm B}}{1470\,{\rm K}}\right)^{-2}\left(\frac{R_*}{2.5R_\odot}\right)\,{\rm au}, \end{aligned} \tag{2.6}$$

respectively. We have expressed the inner radius of region B as $R_{\rm AB}$ because it also stands for the outer radius of the dust-free zone (region A). Similarly, $R_{\rm BC}$ also stands for the inner radius of the optically thick inner rim (region C). We note that our expression for $R_{\rm BC}$ is equivalent to that of Monnier & Millan-Gabet (2002).

Equations (2.5) and (2.6) give the orbital radii of the boundaries of region B if $T_{\rm B}(\approx T_{\rm ev})$ is given. In fact, $T_{\rm ev}$ weakly depends on the gas density, and hence on r. Therefore, if one wants to determine $R_{\rm AB}$ and $R_{\rm BC}$ precisely, one has to solve Equations (2.5) and (2.6) simultaneously with the equation for $T_{\rm ev}$ as a function of r. This is demonstrated in the Appendix.

As we showed, a dust halo naturally appears. The dust halo is a main contributor of the near-infrared emission in the spectral energy distribution of disks around Herbig Ae/Be stars (e.g., Vinković et al. 2006).

2.3.3 Region C: Optically thick dust condensation front

At $r \approx R_{\rm BC}$, dust grains near the midplane fully condense (see Figure 2.2), and the visual optical depth τ_* measured along the line directly from the star exceeds unity at the midplane. Further out, stellar irradiation is absorbed at a height where $\tau_* = 1$, and the midplane temperature is determined by the reprocessed, infrared radiation from dust grains lying at the $\tau_* = 1$ surface. Figure 2.3 schematically illustrates the surface

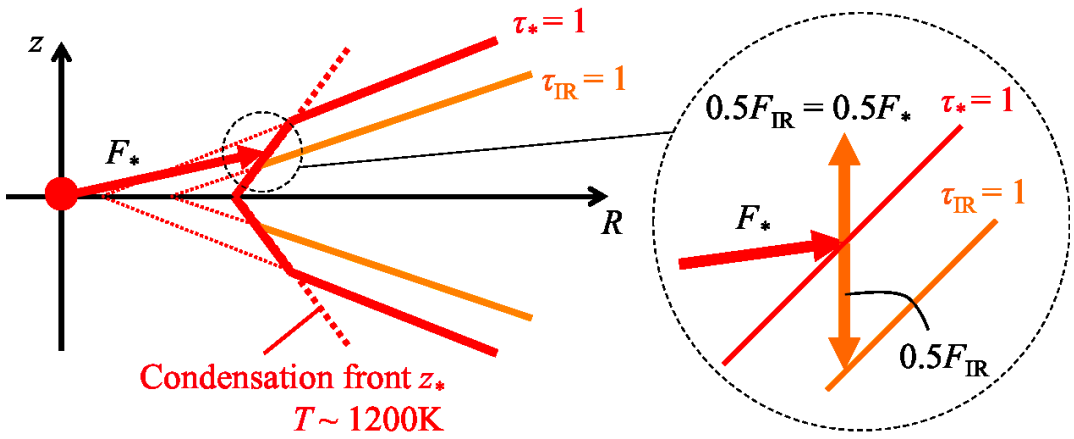

Figure 2.3: Schematic illustration of the geometric and radiative structures of regions C and D. The stellar radiation F_* determines the temperature of the optically thin layer above the $\tau_* = 1$ surface. The dust on the $\tau_* = 1$ surface reprocesses the starlight into infrared radiation $F_{\rm IR}$, and approximately half of the dust emission gets absorbed by the midplane region of the disk. In region C, dust condensation/evaporation controls the location of the $\tau_* = 1$ surface.

structure of regions C and region D. As we show below, region C can be regarded as the zone where the $\tau_* = 1$ surface coincides with the condensation front; the surface structure is approximately determined by the condition that the surface temperature $T_{\rm s,C}$ must be equal to the *characterisctic* temperature ~ 1200 K.

The radial extent of region C is of particular interest because the outer edge of this region sets the inner edge of the dead zone (Flock et al. 2016, Flock et al. 2017). We will see in Section 2.3.4 that the border of regions C and D is related to how the height of the $\tau_* = 1$ surface, z_*, depends on disk radius. Here, we try to estimate this height by considering the energy balance between stellar irradiation on the $\tau_* = 1$ surface and the thermal emission from the surface,

$$\frac{L_*}{4\pi R^2}\sin\theta = \left(\frac{C_{\rm bw}}{4}\right)^{-1}\epsilon\sigma_{\rm SB}T_{\rm s,C}^4, \tag{2.7}$$

where R is the radial distance on the midplane, $\sigma_{\rm SB}$ is the Stefan-Boltzmann constant, and θ is the angle between the starlight and the disk surface (the so-called grazing angle). $C_{\rm bw}$ is a backwarming factor (e.g., Dullemond et al. 2001a) which is defined as the ratio of a full 4π solid angle to the solid angle subtended by the empty sky seen by particles on the surface. The backwarming is heating by surrounding dust particles. If a dust particle radiates into the sky area covered by nearby dust particles, a similar amount of energy is returned from surrounding particles (Kama et al., 2009).

We assume $C_{\rm bw} = 4$, which means that the $\tau_* = 1$ surface can be approximated as a flat wall. In region C, $\epsilon = 1/3$ because dust totally condenses. The grazing angle θ is related to the surface height $z_*(R)$ as (Chiang & Goldreich 1997; Tanaka et al. 2005)

$$\begin{aligned}\theta &= \arcsin\left(\frac{4R_*}{3\pi R}\right) + \arctan\left(\frac{z_*}{R}\frac{d\ln z_*}{d\ln R}\right) - \arctan\left(\frac{z_*}{R}\right) \\ &\approx \frac{4R_*}{3\pi R} + \frac{z_*}{R}\frac{d\ln z_*}{d\ln R} - \frac{z_*}{R},\end{aligned} \tag{2.8}$$

where the second expression assumes $\theta \ll 1$. As mentioned earlier, the $\tau_* = 1$ surface in region C coincides with the condensation front, and the surface temperature $T_{\rm s,C}$ is approximately equal to 1200 K according to the simulations by Flock et al. (2016, see their Figure 2). Substituting Equation (2.8) and $T_{\rm s,C} \approx$ constant into Equation (2.7) and solving the differential equation with respect to z_*, we obtain the surface height in region C as

$$z_{*,\rm C} = \frac{1}{6R_*^2}\left(\frac{T_{\rm s,C}}{T_*}\right)^4 (R^3 - RR_0^2) + \frac{4R_*}{3\pi R_0}(R - R_0), \tag{2.9}$$

where R_0 is the radius at which $z_{*,\rm C} = 0$. Figure 2.4 shows the location of the $\tau_* = 1$ plane obtained by Equation (2.9) and from 3D simulation by Flock et al. (2016). In Figure 2.4, we set $R_0 = 0.4\,$au, which explains Flock et al. (2016) better than $R_0 = R_{\rm BC} \approx 0.46\,$au. Our analytic solution (Equation (2.9)) well reproduces the shape of the condensation front obtained by Flock et al. (2016).

In order to obtain the midplane temperature in region C, $T_{\rm mid,C}$, we assume that the half of the infrared emission from the surface layer come into the interior. Then we have

$$T_{\rm mid,C} = 2^{-1/4} T_{\rm s,C} \approx 1009\ {\rm K}. \tag{2.10}$$

2.3.4 Region D: Optically thick region

Region D is the outermost, coldest region where dust condenses at all heights. Therefore, the temperature structure of this region is essentially the same as that of the classical two-layer disk model by Chiang & Goldreich (1997) and Kusaka et al. (1970). Specifically, the surface temperature profile in this region follows Equation (2.7) with Equation (2.8), $\epsilon = 1/3$, and $C_{\rm bw} = 4$, i.e.,

$$T_{\rm s,D}^4 = 3\left(\frac{R}{R_*}\right)^{-2}\left[\frac{4R_*}{3\pi R} + \frac{z_{*,\rm D}}{R}\left(\frac{d\ln z_{*,\rm D}}{d\ln R} - 1\right)\right] T_*^4, \tag{2.11}$$

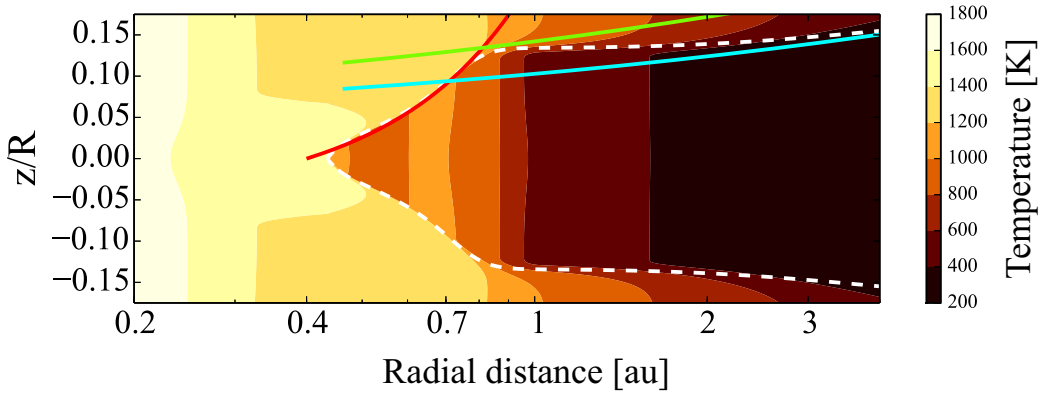

Figure 2.4: Locations of the irradiation ($\tau_* = 1$) surface for the disk model S100 of Flock et al. (2016) obtained from our analytic expressions (solid curves) and from the radiation hydrostatic calculation by Flock et al. (2016) (dashed curve). The red solid curve shows the location of the irradiation surface in region C from our Equation (2.9) with $R_0 = 0.4$ au. The blue and green curves show $z_{*,\mathrm{D}} = 3.6h_\mathrm{g}$ and $4.8h_\mathrm{g}$, which well approximate the height of the irradiation surface in the inner and outer parts of region D, respectively. The curves are overlaid on the 2D temperature map obtained from the radiation hydrostatic calculation of Flock et al. (2016).

where $z_{*,\mathrm{D}}$ is the surface height in region D. Assuming that $z_{*,\mathrm{D}}$ is proportional to the gas scale height $h_\mathrm{g} = c_\mathrm{s}/\Omega_\mathrm{K}$, where c_s is the sound speed and Ω_K is Keplerian angular velocity, we obtain (Kusaka et al., 1970)

$$T_{\mathrm{s,D}}^4 = T_1^4 + T_2^4, \tag{2.12}$$

where

$$\begin{aligned} T_1 &= \left(\frac{4}{\pi}\right)^{1/4}\left(\frac{R}{R_*}\right)^{-3/4} T_* \\ &= 333\left(\frac{R}{1\ \mathrm{au}}\right)^{-3/4}\left(\frac{R_*}{2.5\mathrm{R}_\odot}\right)^{3/4}\left(\frac{T_*}{10^4\ \mathrm{K}}\right)\ \mathrm{K} \end{aligned} \tag{2.13}$$

and

$$\begin{aligned} T_2 &= \left(\frac{6}{7}\right)^{2/7}\left(\frac{z_{*,\mathrm{D}}}{h_\mathrm{g}}\right)^{2/7}\left(\frac{R}{R_*}\right)^{-3/7}\left(\frac{k_\mathrm{B}T_*R_*}{mGM_*}\right)^{1/7} T_* \\ &= 413\left(\frac{z_{*,\mathrm{D}}}{h_\mathrm{g}}\right)^{2/7}\left(\frac{R}{1\ \mathrm{au}}\right)^{-3/7}\left(\frac{R_*}{2.5\mathrm{R}_\odot}\right)^{4/7} \\ &\quad\times\left(\frac{M_*}{2.5M_\odot}\right)^{-1/7}\left(\frac{T_*}{10^4\ \mathrm{K}}\right)^{8/7}\ \mathrm{K}, \end{aligned} \tag{2.14}$$

where k_B is Boltzmann constant, G is the gravitational constant and $m = 4 \times 10^{-24}$ g is the mean molecular mass of the disk gas. As in region C, the midplane temperature

of region D is given by

$$T_{\rm mid,D} = 2^{-1/4} T_{\rm s,D}. \tag{2.15}$$

The border between regions C and D can be defined as the position where the $\tau_* = 1$ surfaces in the two regions intersect. Equating $z_{*,\rm C}$ given by Equation (2.9) with $z_{*,\rm D} = (z_{*,\rm D}/h_{\rm g})h_{\rm g} = (z_{*,\rm D}/h_{\rm g})\sqrt{k_{\rm B}T_{\rm mid,D}R^3/mGM_*}$, we obtain the transcendental equation for the radius $R_{\rm CD}$ of the border,

$$\frac{1}{6R_*^2}\left(\frac{T_{\rm s,C}}{T_*}\right)^4 (R_{\rm CD}^2 - R_{\rm BC}^2) + \frac{4R_*}{3\pi R_{\rm BC}R_{\rm CD}}(R_{\rm CD} - R_{\rm BC}) = \left(\frac{z_{*,\rm D}}{h_{\rm g}}\right)\sqrt{\frac{k_{\rm B}T_{\rm mid,CD}R_{\rm CD}}{mGM_*}}, \tag{2.16}$$

where the subscript CD stands for the value at $R = R_{\rm CD}$. and we have used that $R_0 \approx R_{\rm BC}$ (see Section 2.3.3). In order to derive a closed-form expression for $R_{\rm CD}$, we simplify Equation (2.16) as follows. Firstly, we neglect the second term on the left-hand side of Equation (2.16) because for T-Tauri and Herbig stars the inner-rim radius is much larger than the stellar radius. Secondly, we replace the factor $T_{\rm mid,CD}^{1/2} = (2^{-1}T_{\rm s,CD}^4)^{1/8}$ appearing in the right-hand side of Equation (2.16) by $(T_{\rm 2,CD}^4)^{1/8}$, where $T_{\rm 2,CD}$ is the value of T_2 at $R = R_{\rm CD}$, because $T_1 \sim T_2$ at $R \sim 0.1$–1 au (see Equations (2.13) and (2.14)). Thirdly, we neglect the $R_{\rm CD}$-dependence of the right-hand side, by substituting $R_{\rm CD} = 2R_{\rm BC}$ in the right-hand side only, because the dependence is generally weak ($\sqrt{R_{\rm CD}T_{\rm mid,CD}} \propto R_{\rm CD}^{1/8}$ for $T_{\rm mid,CD} \approx 2^{-1/4}T_{\rm 1,CD}$, and $\sqrt{R_{\rm CD}T_{\rm mid,CD}} \propto R_{\rm CD}^{2/7}$ for $T_{\rm mid,CD} \approx 2^{-1/4}T_{\rm 2,CD}$). With these simplifications, Equation (2.16) can be analytically solved with respect to $R_{\rm CD}$, and we thus obtain an closed-form expression for $R_{\rm CD}$,

$$R_{\rm CD} = \sqrt{1+\Gamma}R_{\rm BC} \tag{2.17}$$

where

$$\Gamma \equiv 3.1\left(\frac{R_{\rm BC}}{0.46\ {\rm au}}\right)^{-12/7}\left(\frac{z_{*,\rm D}/h_{\rm g}}{4.8}\right)^{8/7}\left(\frac{T_*}{10^4\ {\rm K}}\right)^{32/7} \times\left(\frac{M_*}{2.5M_\odot}\right)^{-1/2}\left(\frac{R_*}{2.5R_\odot}\right)^{16/7}. \tag{2.18}$$

If we use Equation (2.6) to eliminate $R_{\rm BC}$ from Γ, we obtain

$$\Gamma = 3.1\left(\frac{z_{*,\rm D}/h_{\rm g}}{4.8}\right)^{8/7}\left(\frac{L_*}{56L_\odot}\right)^{2/7}\left(\frac{M_*}{2.5M_\odot}\right)^{-1/2}, \tag{2.19}$$

here, we set $\kappa_{\rm d}(T_*)/\kappa_{\rm d}(T_{\rm B}) = 1/3$ and $T_{\rm B} = 1470$ K. The resultant equations (Equations (2.17) and (2.19)) justify the validity of the approximation of $R_{\rm CD} = 2R_{\rm BC}$. Our simplifications introduce an error of less than 10% in the estimate of $R_{\rm CD}$; if we exactly solve Equation (2.16), we obtain $R_{\rm CD} = 0.85$ au with $T_* = 10000$ K, $R_* = 2.5R_\odot$, $M_* = 2.5M_\odot$ and $z_{*,\rm D}/h_{\rm g} = 4.8$, while Equation (2.17) leads to $R_{\rm CD} = 0.92$ au. As seen in Figure 2.4, the ratio $z_{*,\rm D}/h_{\rm g}$ is a function of the distance from the central star: The ratio $z_{*,\rm D}/h_{\rm g}$ is about 3.6 at outer part and 4.8 at inner part of region D due to the extra heating by the hot rim surface discussed below. Therefore, when we estimate the location of $R_{\rm CD}$, it is better to use the higher value for $z_{*,\rm D}/h_{\rm g}$ (≈ 4.8). On the other hand, when we estimate the temperature in region D, it is better to use the lower value for $z_{*,\rm D}/h_{\rm g}$ (≈ 3.6).

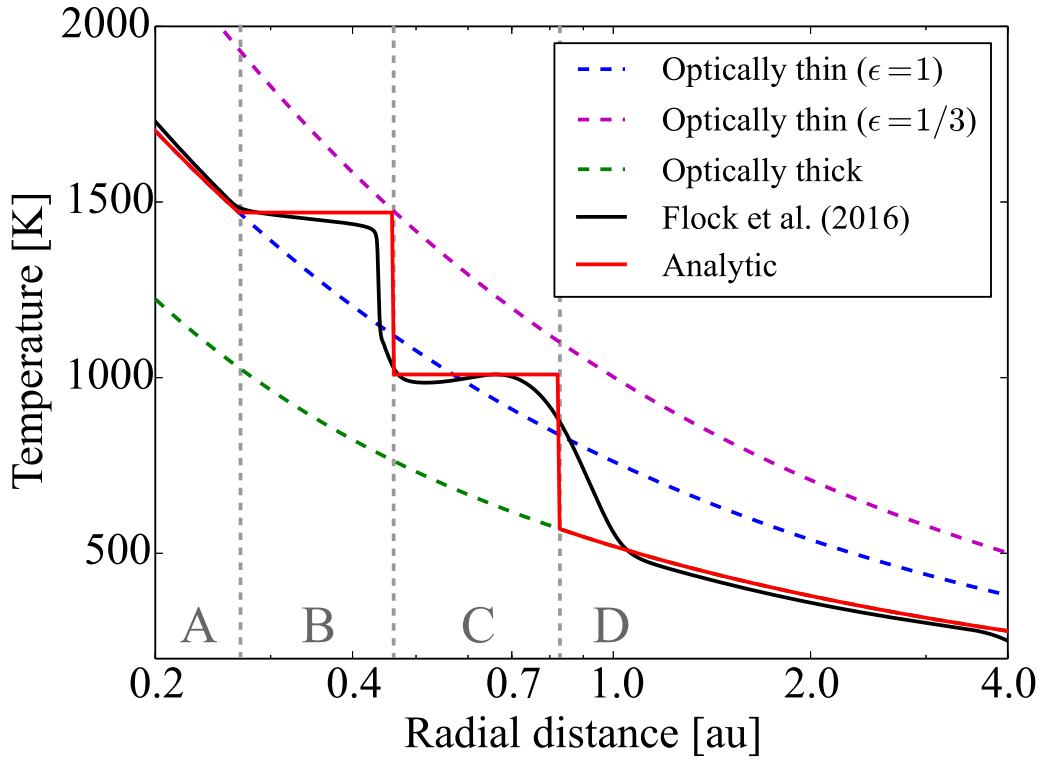

Figure 2.5: Radial profile of the midplane temperature $T_{\rm mid}$ for the disk model S100 of Flock et al. (2016). The black solid line is from the radiative hydrostatic calculation by Flock et al. (2016, their Figure 1), whereas the red solid line is from our analytic expressions: Equation (2.3) for region A, $T = T_{\rm eva} = 1470$ K for region B, Equation (2.10) for region C, Equation (2.15) with $z_{*,\rm D}/h_{\rm g} = 3.6$ for region D. Boundaries are determined by Equations (2.5), (2.6) and (2.17). For reference, the temperature profiles for optically thin disks with $\epsilon = 1$ and $1/3$ are shown by the blue and purple dashed lines, respectively, and the profile for a smooth optically thick disk (Equation (2.15)) is shown by the green dashed line.

In Figure 2.5, we compare our analytic temperature profile with the profile derived from the radiative hydrostatic disk model S100 of Flock et al. (2016). We find that our analytic profile well reproduces the result of Flock et al. (2016) except in the inner part of region D ($R \approx 0.8$–1 au), where our Equation (2.15) underestimates the midplane temperature. This implies that some sources other than the central star heat the inner part of region D.

As we show below, this discrepancy can be resolved by taking into account the irradiation by the hot rim surface located in region C as shown in Figure 2.1. For simplicity, we approximate the $\tau_* = 1$ surface of region C by a flat surface truncated at $R = R_{\rm CD}$, and assume that the $\tau_{\rm IR} = 1$ surface is located at distance h below the $\tau_* = 1$ surface (see Figure 2.6). At any radial position R on the $\tau_{\rm IR}$ surface, the balance between radiative cooling on the $\tau_{\rm IR} = 1$ surface and irradiation heating by the hot rim surface can be written as

$$\sigma_{\rm SB} T_{\rm mid,D}^4 = \int_{-\infty}^{R_{\rm CD}} \frac{\sigma_{\rm SB} T_{\rm s,C}^4}{2\pi l} \frac{h}{l} dR' \tag{2.20}$$

with $l = \sqrt{h^2 + (R - R')^2}$, where we have used that in the absence of internal heat sources, the temperature at the $\tau_{\rm IR} = 1$ is equal to the midplane surface. Performing the integration, we obtain

$$T_{\rm mid,D} = \left\{ \frac{1}{2\pi} \left[\tan^{-1} \left(\frac{R_{\rm CD} - R}{h} \right) + \frac{\pi}{2} \right] \right\}^{1/4} T_{\rm s,C}. \tag{2.21}$$

Strictly speaking, the $\tau_* = 1$ surface of region C is not parallel to the $\tau_{\rm IR} = 1$ surface of region D. From Equations (2.9) and (2.15), the inclinations of $\tau_* = 1$ surfaces in regions C and D with respect to the mid-plane at $R = R_{\rm CD}$ can be estimated as 30° and 10°, respectively. Hence, if we assume that $\tau_{\rm IR} = 1$ surfaces in regions C and D are parallel to the $\tau_* = 1$ surfaces in regions C and D, respectively, the angle made by the $\tau_* = 1$ surface in region C and the $\tau_{\rm IR} = 1$ surface in region D is $\approx 20°$. This deviation from the plane-parallel approximation introduces an error of $\sim 20\%$ in temperature. Nevertheless, our analytic formula (Equation (2.21)) based on the approximation well reproduces the result of Flock et al. (2016) with an error much less than $\sim 20\%$. This might be because the actual position of $\tau_{\rm IR} = 1$ surface in region D is not parallel to the $\tau_* = 1$ surface in region D and should be determined by the optical depth along the ray emitted by each position on the $\tau_* = 1$ surface in region C. If one needs more accurate temperature structure, detailed radiative transfer simulations would be needed.

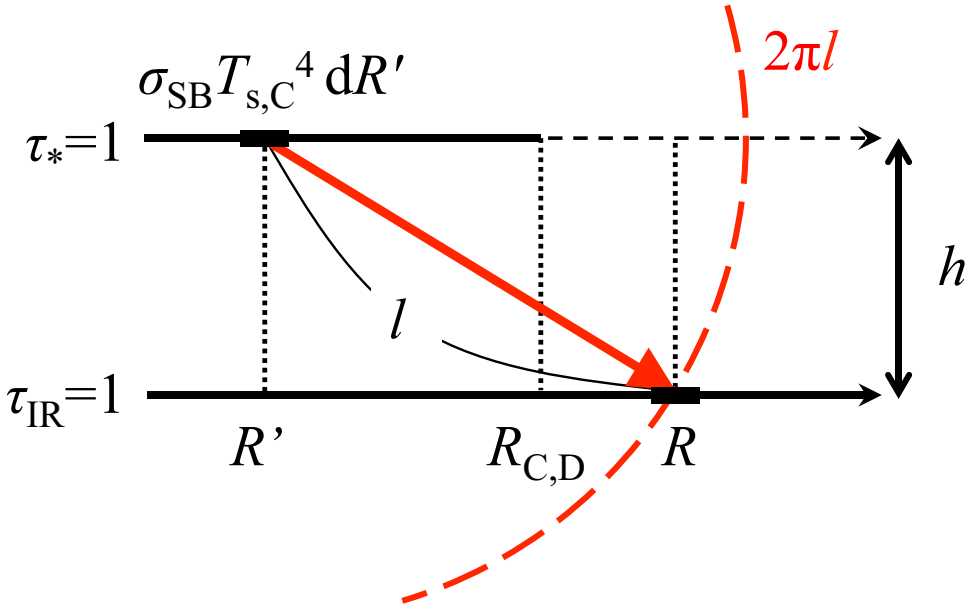

Figure 2.6: Schematic illustration of the irradiation by the condensation front at the vicinity of the boundary between regions C and D. A line element with a width dR' at a position R' on the truncated $\tau_* = 1$ surface irradiates in the infrared wavelength with temperature $T_{s,C}$. The emission travels along the distance l and gets absorbed by the position R on the $\tau_{IR} = 1$ surface located at distance h below the $\tau_* = 1$ surface.

Figure 2.7 shows the analytic temperature profile refined with Equation (2.21). We set $h = 0.05 R_{CD}$ which is a bit larger than the typical gas scale height and $R_{CD} = 0.86$ au which explains Flock et al. (2016) better than that estimated from Equation (2.17) (≈ 0.83 au with $z_{*,D}/h_g = 3.6$). The larger value of h leads to the larger radial extent of the region where the additional heating by the hot rim is important (region D′) We here use Equation (2.21) or (2.15), whichever is greater, for the temperature in region D. We find that the refined model well reproduces the temperature profile of Flock et al. (2016) in the vicinity of the boundary between regions C and D.

2.4 Discussion

2.4.1 The position of the dead zone inner edge

One of the motivation of this work is to determine the position of the dead zone inner edge, R_{DIB}. Our results show that at the boundary between regions C and D, the temperature steeply decreases from $\sim$ 1000 K to $\sim$ 600 K. According to Desch & Turner (2015), the position of the dead zone inner edge would be located at where

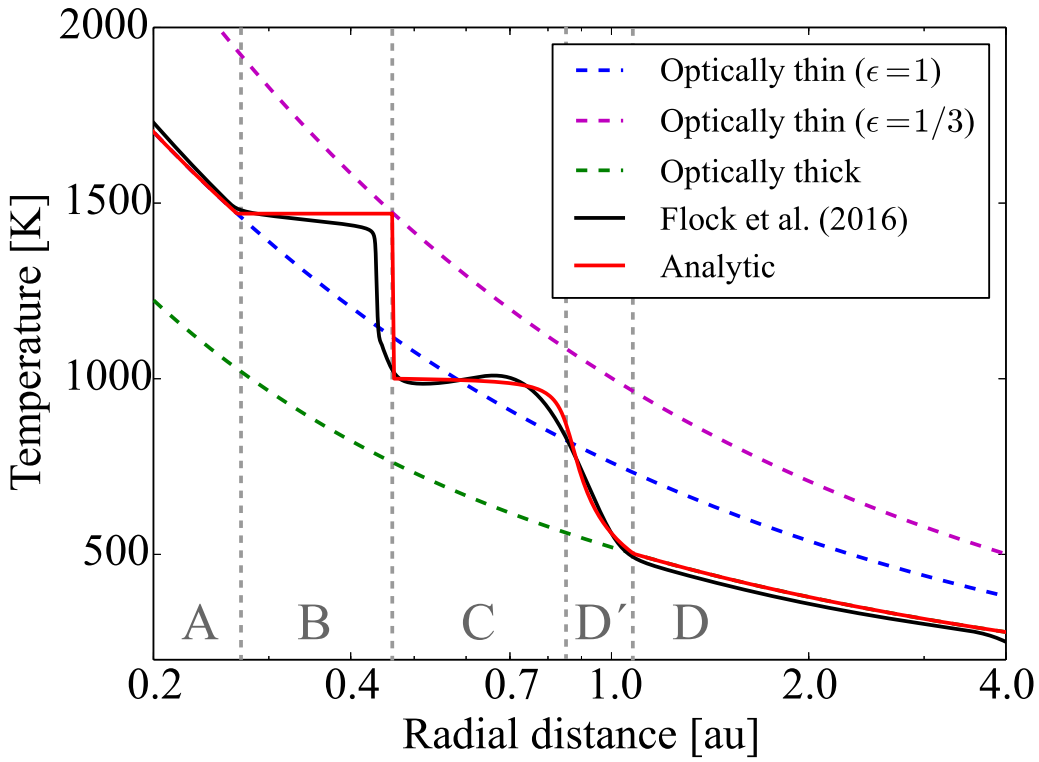

Figure 2.7: Same as Figure 2.5 except that the analytic temperature profile (red line) now uses Equation (2.21) with $h = 0.05 R_{\rm CD}$ for the midplane temperature in inner part of region D, region D′. We set $R_{\rm CD} = 0.86$ au which explains Flock et al. (2016) better than that estimated from Equation (2.17) (0.83 au with $z_{*,\rm D}/h_{\rm g} = 3.6$).

$T \sim 1000$ K. Therefore, the boundary between regions C and D is thought to be the dead zone inner edge. From Equation (2.17), $R_{\rm DIB}$ can be estimated as 0.09 au with $T_* = 5000$ K and $M_* = 1 M_\odot$ and 0.8 au with $T_* = 10000$ K and $M_* = 2.5 M_\odot$ with $z_{*,\rm D}/h_{\rm g} = 4.8$, $\kappa_{\rm d}(T_*)/\kappa_{\rm d}(T_{\rm B}) = 1/3$ and $T_{\rm B} = 1470$ K, while the classical optically thick temperature profile (Equation (2.15)) leads to $R_{\rm DIB} \approx 0.03$ au with $T_* = 5000$ K and $M_* = 1 M_\odot$ and $R_{\rm DIB} \approx 0.3$ au with $T_* = 10000$ K and $M_* = 2.5 M_\odot$. Therefore, the location of the dead zone inner edge estimated from our model is 2–3 times farther out than that estimated from the classical optically thick temperature profile. This is because the temperature in region C is much higher than that estimated from the classical model due to the stellar irradiation on the condensation front with high incident angle.

2.4.2 The effect of viscous heating

We have focused on passively irradiated disks where the effect of viscous heating on the temperature structure is negligibly small. In the opposite case where viscous heating dominates over stellar irradiation, the midplane temperature $T_{\rm mid,vis}$ is given by

$$T_{\rm mid,vis} = \left(1 + \frac{3\tau_{\rm IR}}{4}\right)^{1/4} T_{\rm s,vis} \tag{2.22}$$

where $\tau_{\rm IR}$ is the infrared optical depth at the midplane, and

$$\begin{aligned} T_{\rm s,vis} &= \left(\frac{3GM_*\dot{M}}{8\pi\sigma_{\rm SB}R^3}\right)^{1/4} \\ &\approx 107\left(\frac{R}{1\ {\rm au}}\right)^{-3/4}\left(\frac{M_*}{2.5M_\odot}\right)^{1/4}\left(\frac{\dot{M}}{10^{-8}M_\odot/{\rm yr}}\right)^{1/4}\ {\rm K} \end{aligned} \tag{2.23}$$

is the surface temperature determined by the mass accretion rate $\dot{M} = 3\pi\Sigma_{\rm g}\nu$ (e.g., Shakura & Sunyaev, 1973), where ν is the turbulent viscosity.

To see when viscous heating can be neglected, we compare Equation (2.22) with Equation (2.15), which is the minimum estimate for the midplane temperature of a passively irradiated disk (see Figure 2.7). Combining Equations (2.15) and (2.22), together with $\tau_{\rm IR} = (1/2)\kappa_{\rm d}\Sigma_{\rm d} = (1/2)f_{\rm d2g}\kappa_{\rm d}\Sigma_{\rm g}$ (where $\Sigma_{\rm g}$ and $\Sigma_{\rm d}$ are the surface densities of gas and dust), we find that $T_{\rm mid,D} > T_{\rm mid,vis}$ if

$$\begin{aligned} &0.8\left(\frac{L_*}{56L_\odot}\right)^{-2/7}\left(\frac{M_*}{2.5M_\odot}\right)^{31/70}\left(\frac{\kappa_{\rm d}}{700\ {\rm cm^2\ g^{-1}}}\right)^{1/5}\left(\frac{f_{\rm d2g}}{10^{-2}}\right)^{1/5} \\ &\times\left(\frac{\dot{M}}{10^{-8}M_\odot\ {\rm yr^{-1}}}\right)^{2/5}\left(\frac{\alpha}{10^{-3}}\right)^{-1/5}\left(\frac{R}{1\ {\rm au}}\right)^{-33/70} < 1. \end{aligned} \tag{2.24}$$

Here, we have used the α-prescription for the turbulent viscosity (Shakura & Sunyaev, 1973), i.e., $\nu = \alpha c_{\rm s} h_{\rm g}$. We have also assumed $\tau_{\rm IR} \gg 1$, $z_{*,\rm D}/h_{\rm g} = 3.6$ and $T^4_{\rm s,D} = 2T^4_2$ for simplicity. Equation (2.24) suggests that in a disk around a Herbig Ae star of $L_* = 56L_\odot$ and $M_* = 2.5M_\odot$, and $\dot{M} = 10^{-8}M_\odot\ {\rm yr^{-1}}$, stellar irradiation dominates over viscous heating if $f_{\rm d2g} \lesssim 10^{-2}$, in agreement with the result of the hydrodynamical simulation by Flock et al. (2016, see their Figure 8). Even in a inner part (~ 0.1 au) of a disk around a T Tauri star of $L_* = L_\odot$ and $M_* = M_\odot$, stellar irradiation dominates if $f_{\rm d2g} \lesssim 10^{-3}$ and $\dot{M} \lesssim 6\times10^{-10}M_\odot\ {\rm yr^{-1}}$. Therefore, our temperature model is applicable to weakly accreting T Tauri disks where tiny, opacity-dominating dust is depleted (through, e.g., dust coagulation).

2.4.3 Migration trap

A steep temperature drop as seen in the borders of regions B, C, and D is known to act as a planet trap where the strong corotation torque halts the inward migration of planets due to the negative Lindblad torque from the gas disk (e.g., Paardekooper et al. 2010). In addition, if the boundary between regions C and D sets the dead-zone inner edge as discussed in Section 2.4.1, the positive surface density gradient arising from the change in turbulent viscosity also prevents planets from inward migration (Masset et al., 2006).

It is meaningful to compare the location of the borders to the orbital distribution of observed planets in oder to reveal whether the borders really act as the migration trap. Our solutions show that the positions of the boundaries between regions B, C and D are roughly proportional to $L_*^{1/2}$, though the position of the boundary between regions C and D has the additional factor $\sqrt{1+\Gamma}$ which slightly depends on the stellar parameters.green If we assume $L_* \propto M_*^{3/2}$ (Mulders et al., 2015), these boundaries are scaled as $M_*^{3/4}$. Mulders et al. (2015) investigated Kepler Objects of Interest (KOIs) and showed that the distance from the star where the planet occurrence rate drops scales with semi-major axis as $M_*^{1/3}$, which is different from our estimate. However, the spectral range is not enough for the detailed comparison because the majority of the host star for KOIs are F, G and K-type stars. In order to discuss the boundaries really act as a migration trap, observations of planets around A and B-type stars are needed. Mulders et al. (2015) also showed that many KOIs orbit at ~ 0.1 au which is similar to the value of $R_{\rm DIB}$ estimated from our model.

2.4.4 Instabilities at the inner region of protoplanetary disks

Steep temperature gradients at the boundaries between regions B, C and D would induce various kind of instabilities. One possible instability is the subcritical baroclinic instability, which is the instability powered by radial buoyancy due to the unstable entropy gradient (Klahr & Bodenheimer 2003, Lyra 2014). If we assume the power-law density and temperature profile as $\rho \propto R^{-\beta_\rho}$ and $T \propto R^{-\beta_T}$, respectively, the condition for the subcritical baroclinic instability is given by (Klahr & Bodenheimer, 2003)

$$\beta_T - (\gamma_{\rm ad} - 1)\beta_\rho > 0, \tag{2.25}$$

where $\gamma_{\rm ad}$ is the adiabatic index. This condition would be satisfied at the boundaries between regions B, C and D, where β_T is large. The boundary between regions C and D might also have a positive surface density gradient ($\beta_\rho < 0$) if the dead-zone

edge inner edge lies there. The positive density gradient would further enhance the instability on the boundary. However, the subcritical baroclinic instability does not been observed in Flock et al. (2016). This is because the spatial resolution Flock et al. (2016) has is not enough to resolve the instability. Lyra (2014) showed that for resolutions > 32 cells/h_g the subcritical instability converges, while Flock et al. (2016) uses around 15 cells/h_g. And also, Flock et al. (2016) calculated for around 20 local orbits at 2 au, which is not enough for the subcritical instability to operate. The growth timescale for the instability requires many hundreds of local orbits (Lyra, 2014).

The Rossby wave instability could also be induced at the boundary between regions C and D due to the steep surface density gradient produced by the dead-zone edge (Lyra & Mac Low, 2012). In fact, the magnetohydrodynamical simulation by Flock et al. (2017) shows that the boundary between regions C and D produces a vortex, indicating that the Rossby wave instability should operate there.

If such instabilities operate on these boundaries, vortices caused by the instabilities would accumulate dust (e.g., Barge & Sommeria 1995), which in turn could lead to rocky planetesimal formation via the streaming instability (e.g., Youdin & Goodman 2005). We will explore this possibility in future work.

2.5 Summary

We have analytically derived the temperature and dust-to-gas mass ratio profile for the inner region of protoplanetary disks based on the results from the recent hydrodynamical simulations conducted by Flock et al. (2016). The temperature profile for the inner region of protoplanetary disks can be divided into four regions. The innermost region is dust-free and optically thin with the temperature determined by the gas opacity (Equation (2.3)). As the temperature goes down and approaches the dust evaporation temperature, silicate dust starts to condense, producing an optically thin dust halo with a nearly constant temperature regulated by partial dust condensation. We have derived the dust-to-gas mass ratio profile in the dust halo using the fact that partial dust condensation regulates the temperature to the dust evaporation temperature (Equation (2.4)). Beyond the dust halo, there is an optically thick condensation front where all the available silicate gas condenses out. The curvature of the condensation surface is simply determined by the condition that the surface temperature must be nearly equal to the characteristic temperature $\sim 1200\,\mathrm{K}$ (Equation (2.9)). The temperature profile for the outermost region is essentially same as the classical

optically thick temperature profile (e.g., Kusaka et al. 1970). We have derived the mid-plane temperature in the outer two regions using the two-layer approximation with the additional heating by the condensation front for the outermost region. As a result, the overall temperature profile follows a step-like profile with steep temperature gradients at the borders between the outer three regions. The borders might act as planet traps where the inward migration of planets due to gravitational interaction with the gas disk stops. The temperature at the border between the two outermost regions coincides with the temperature needed to activate magnetorotational instability, suggesting that the inner edge of the dead zone must lie at this border. The radius of the dead-zone inner edge predicted from our temperature profile is $\sim$ 2–3 times larger than that expected from the classical optically thick temperature.

2.6 Appendix

2.6.1 Effect of the evaporation temperature

Dust evaporation temperature $T_{\rm ev}$ is modeled as a function of the gas density ρ as (Isella & Natta, 2005)

$$T_{\rm ev} = 2000 \left(\frac{\rho}{1 \text{ g cm}^{-3}} \right)^{0.0195} \text{ K}. \tag{2.26}$$

Using the relation $\rho = \Sigma_{\rm g} / \sqrt{\pi} h_{\rm g}$ and substituting Equation (2.26) as $T_{\rm B}$, Equations (2.5) and (2.6) can be rewritten as

$$\begin{aligned} R_{\rm AB} &= \left[0.079 \left(\frac{R_*}{0.01 \text{ au}} \right) \left(\frac{T_*}{5000 \text{ K}} \right)^2 \right. \\ &\times \left. \left(\frac{\Sigma_0}{100 \text{ g cm}^{-2}} \right)^{-0.0386} \left(\frac{M_*}{M_\odot} \right)^{-0.0193} \right]^{\gamma} \text{ au} \end{aligned} \tag{2.27}$$

and

$$R_{\rm BC} = \left(\frac{\kappa_{\rm d}(T_*)}{\kappa_{\rm d}(T)} \right)^{\gamma/2} R_{\rm AB}, \tag{2.28}$$

respectively. Here, Σ_0 is the surface density at 1 au. The index γ is related to the index of the radial surface density profile, $\Sigma_{\rm g} \propto r^{-\beta}$, as $\gamma = 2.0195/(1.9025 - 0.078\beta)$. For $\beta = 1$, $\gamma \approx 1.107$. Equation (2.27) is similar to the expression derived by Kama et al. (2009, their Equation (A.4)) although the β dependence is different. If the disk is massive ($\Sigma_0 \gg 1000$ g cm^{-2}), the boundary between region B and C (i.e. the radial position for $\tau_* = 1$) moves closer to the star compared to $R_{\rm BC}$ written by Equations

(2.6) and (2.28) because of the large optical depth. In this case, in oder to determine the radial position of $\tau_* = 1$, we have to calculate the optical depth using Equation (2.4).

Chapter 3

Dust-Pileup at the Dead-Zone Inner Edge and Implications for the Disk Shadow

Modified from Ueda, Flock & Okuzumi 2019, ApJ, 871, 10

3.1 Abstract of this Chapter

We perform simulations of the dust and gas disk evolution to investigate the observational features of a dust-pileup at the dead-zone inner edge. We show that the total mass of accumulated dust particles is sensitive to the turbulence strength in the dead zone, $\alpha_{\rm dead}$, because of the combined effect of turbulence-induced particle fragmentation (which suppresses particle radial drift) and turbulent diffusion. For a typical critical fragmentation velocity of silicate dust particles of 1 m s^{-1}, the stress to pressure ratio $\alpha_{\rm dead}$ needs to be lower than 3×10^{-4} for dust trapping to operate. The obtained dust distribution is postprocessed using the radiative transfer code RADMC-3D to simulate infrared scattered-light images of the inner part of protoplanetary disks with a dust pileup. We find that a dust pileup at the dead-zone inner edge, if present, casts a shadow extending out to $\sim$ 10 au. In the shadowed region the temperature significantly drops, which in some cases yields even multiple water snow lines. We also find that even without a dust pileup at the dead-zone inner edge, the disk surface can become thermally unstable, and the excited waves can naturally produce shadows and ring-like structures in observed images. This mechanism might account for the ring-like structures seen in the scattered-light images of some disks, such as the TW Hya disk.

3.2 Introduction of this Chapter

The inner region of protoplanetary disks is the birthplace of rocky planetesimals and planets. One preferential site of rocky planetesimal formation is the inner edge of the so-called dead zone (e.g., Kretke et al. 2009). The dead zone is the location where magneto-rotational instability (MRI, Balbus & Hawley 1998) is suppressed because of poor gas ionization (Gammie, 1996). The dead zone is likely to have an inner edge where the gas temperature T reaches $\sim$1000 K, above which thermal ionization of the gas is effective enough to activate MRI (Gammie, 1996; Desch & Turner, 2015). Across the dead zone inner edge, the turbulent viscosity arising from MRI steeply decreases from inside out, resulting in a local maximum in the radial profile of the gas pressure (e.g., Dzyurkevich et al. 2010; Flock et al. 2016; Flock et al. 2017). The pressure maximum traps solid particles (Whipple, 1972; Adachi et al., 1976) and the local dust-to-gas mass ratio increases, leading potentially to the formation of rocky planetesimals via the streaming instability (Youdin & Goodman, 2005; Johansen et al., 2007; Carrera et al., 2015) or via the gravitational instability (Coradini et al., 1981).

There have been many studies related to the dust-pileup at the dead-zone inner edge (e.g., Brauer et al. 2008; Kretke et al. 2009; Dzyurkevich et al. 2010; Pinilla et al. 2016). Kretke et al. (2009) examined the accumulation and coagulation of solid particles around the dead-zone inner edge and found that the dust-pileup at the dead-zone inner edge leads to the efficient formation of gas giants. However, Kretke et al. (2009) ignored the effect of the fragmentation of large silicate particles. Both laboratory experiments (e.g., Blum & Wurm 2000) and numerical simulations (e.g., Wada et al. 2013) have shown that silicate dust particles are easy to fragment with a typical collisional velocity in protoplanetary disks. The fragmentation must regulate growth of solids and it significantly affect the behavior of dust motion in the gas. There are also some studies on the dust-pileup at the dead-zone inner edge caused by the combination of the inner-hole due to disk wind and non-thermal ionization (e.g., Pinilla et al. 2016) or by the ice sublimation (e.g., Brauer et al. 2008). In this work, we focus on the innermost dust concentration zone, which is of most importance also in the inside-out planet formation framework (e.g., Chatterjee & Tan 2014).

Even for the observational aspects, the dead-zone inner edge would be a interesting subject. For example, VLTI/MATISSE instrument will allow us to image the inner region of protoplanetary disks at mid-infrared wavelengths with high angular

resolution ($\sim$ 5 mas in L-band, e.g., Lopez et al. 2014), which will provide us opportunities to directly compare the theoretical models with the observations of the dead-zone inner edge. Especially nearby Herbig stars are ideally suited to study this region due to high luminosity and the position of the inner dust rim (Dullemond & Monnier 2010 for review). However, previous studies on the dust-pileup at the dead-zone inner edge have not focused on the comparison with the observations.

This work mainly consists of two parts. First, we investigate the properties of the dust-pileup at the dead-zone inner edge for a broad range of critical fragmentation velocity of silicate dust particles and strength of the turbulence. Second, we examine the observational signatures of the dust-pileup at the dead-zone inner edge by performing the radiative transfer simulations. In Section 3.3, we introduce the model of dust growth simulations and provide results of the simulations. The setup for the radiative transfer simulations and its results are shown in Section 3.4. In Section 3.5, we briefly mention the non-convergence found in the radiative transfer simulations probably caused by the so-called thermal wave instability. The implications for the planet formation and for disk observations are given in Section 3.6. The summary is in Section 3.7.

3.3 Dust-Pileup at the Dead-Zone Inner Edge

In this section, we introduce models of dust growth simulation and show how the properties of the dust-pileup depend on the critical fragmentation velocity of dust particles and the strength of the turbulence.

3.3.1 Dust and gas evolution models

We investigate the evolution of dust and gas disk around a Herbig-type star with stellar mass $M_* = 2.5 M_\odot$, radius $R_* = 2.5 R_\odot$ and effective temperature $T_* = 10000$ K. The resultant stellar luminosity is $56 L_\odot$. The size evolution of dust particles is also simultaneously calculated and we employ simplified dust coagulation equation in which the dust size distribution is characterized by the single representative mass $m_{\rm p}(r)$.

3.3.1.1 Surface density evolution

We follow the time evolution of the gas and dust surface densities Σ_g and Σ_d by calculating one-dimensional continuity equation of dust

$$\frac{\partial \Sigma_d}{\partial t} + \frac{1}{r}\frac{\partial}{\partial r}\left\{ r v_{r,d} \Sigma_d - \frac{\nu}{1+\mathrm{St}^2} r \Sigma_g \frac{\partial Z}{\partial r} \right\} = 0, \tag{3.1}$$

and that of gas

$$\frac{\partial \Sigma_g}{\partial t} + \frac{1}{r}\frac{\partial}{\partial r}(r v_{r,g} \Sigma_g) = 0, \tag{3.2}$$

where r is a midplane distance from the central star, ν is the turbulent viscosity, St is the dimensionless stopping time of the dust particles, Z is the dust-to-gas surface density ratio, $v_{r,d}$ and $v_{r,g}$ are the radial velocities of dust and gas, respectively. The radial velocities of dust and gas are respectively written as (Kretke et al. 2009; Kanagawa, Ueda, Muto, Okuzumi 2017)

$$v_{r,d} = -\frac{\mathrm{St}}{\mathrm{St}^2 + (1+Z)^2} 2\eta v_K + \frac{1+Z}{\mathrm{St}^2 + (1+Z)^2} v_{vis} \tag{3.3}$$

and

$$v_{r,g} = \frac{\mathrm{St}Z}{\mathrm{St}^2 + (1+Z)^2} 2\eta v_K + \left\{ 1 - \frac{(1+Z)Z}{\mathrm{St}^2 + (1+Z)^2} \right\} v_{vis}, \tag{3.4}$$

where v_K is the Keplerian velocity and v_{vis} is the radial velocity of the gas due to viscous diffusion written as

$$v_{vis} = -\frac{3\nu}{r} \frac{\partial \ln \left(r^{1/2} \nu \Sigma_g \right)}{\partial \ln r}. \tag{3.5}$$

Equations (3.3) and (3.4) fully include the effect of dust backreaction on the gas disk. When the disk turbulence is weak and the dust-to-gas mass ratio is high enough, the backreaction leads to the outward motion of the gas, which facilitates efficient piling-up of dust particles (Gonzalez et al. 2017, Kanagawa, Ueda, Muto, Okuzumi 2017). The variable η characterizes the sub-Keplerian motion of the gas disk and is written as

$$\eta = -\frac{1}{2}\left(\frac{c_s}{v_K}\right)^2 \frac{\partial \ln p}{\partial \ln r}, \tag{3.6}$$

where $c_s = \sqrt{k_B T / m_g}$ is the sound speed of disk gas at the midplane and $p = \rho_g c_s^2$ is pressure of the gas with k_B and m_g being the Boltzmann constant and mean molecular mass (taken to be 2.4 amu), respectively.

The motion of dust in disks is characterized by the Stokes number, dimensionless stopping time, defined as

$$\mathrm{St} \equiv \Omega_{\mathrm{K}} \tau_{\mathrm{s}}, \tag{3.7}$$

where Ω_{K} is the Keplerian frequency and τ_{s} is the stopping time of the dust particles. The stopping time is related to the dust radius a as

$$\tau_{\mathrm{s}} = \begin{cases} \dfrac{\rho_{\mathrm{int}} a}{\rho_{\mathrm{g}} v_{\mathrm{th}}}, & a < \dfrac{9\lambda_{\mathrm{mfp}}}{4}, \\ \dfrac{\rho_{\mathrm{int}} a}{\rho_{\mathrm{g}} v_{\mathrm{th}}} \dfrac{4a}{9\lambda_{\mathrm{mfp}}}, & a > \dfrac{9\lambda_{\mathrm{mfp}}}{4}, \end{cases} \tag{3.8}$$

where ρ_{int} is the dust internal density, ρ_{g} is the midplane gas density, $v_{\mathrm{th}} = \sqrt{8/\pi} c_{\mathrm{s}}$ is the thermal velocity of the gas and λ_{mfp} is the mean free path of gas molecules. The midplane gas density is given by $\rho_{\mathrm{g}} = \Sigma_{\mathrm{g}} / \sqrt{2\pi} h_{\mathrm{g}}$, where $h_{\mathrm{g}} = c_{\mathrm{s}} / \Omega_{\mathrm{K}}$ is the gas scale height. The mean free path of gas molecules is related to the midplane gas density as $\lambda_{\mathrm{mfp}} = m_{\mathrm{g}} / (\sigma_{\mathrm{mol}} \rho_{\mathrm{g}})$, where $\sigma_{\mathrm{mol}} = 2 \times 10^{-15}$ cm^2 is the molecular collisional cross section. From these, the Stokes number can be rewritten as

$$\mathrm{St} = \frac{\pi}{2} \frac{\rho_{\mathrm{int}} a}{\Sigma_{\mathrm{g}}} \max\left(1, \frac{4a}{9\lambda_{\mathrm{mfp}}}\right). \tag{3.9}$$

For simplicity, the dust internal density is set to be 3.0 g cm^{-3} for the region where the icy component is evaporated (i.e., $T > 160$ K) and 1.4 g cm^{-3} elsewhere. The initial gas surface density is calculated assuming the radially constant mass accretion rate of $10^{-8} M_\odot$ yr^{-1} and the initial dust surface density is set to be $0.01 \Sigma_{\mathrm{g}}$.

3.3.1.2 Dust-size evolution

For the evolution of dust particles, we calculate the evolution of a representative mass of dust particles, m_{p}, for each radial grid using the single-size approximation (Sato et al., 2016):

$$\frac{\partial m_{\mathrm{p}}}{\partial t} + v_{\mathrm{r,d}} \frac{\partial m_{\mathrm{p}}}{\partial r} = \epsilon_{\mathrm{grow}} \frac{2\sqrt{\pi} a^2 \Delta v_{\mathrm{pp}}}{h_{\mathrm{d}}} \Sigma_{\mathrm{d}}, \tag{3.10}$$

where h_{d} is the scale-height of the dust disk. The dust scale height is assumed to be a mixing-settling equilibrium (Dubrulle et al., 1995; Youdin & Lithwick, 2007)

$$h_{\mathrm{d}} = h_{\mathrm{g}} \left(1 + \frac{\mathrm{St}}{\alpha} \frac{1 + 2\mathrm{St}}{1 + \mathrm{St}}\right)^{-1/2}, \tag{3.11}$$

where α is the stress to pressure ratio (Shakura & Sunyaev, 1973). The coefficient $\epsilon_{\rm grow}$ is the sticking efficiency for a single collision, which we model as (Okuzumi & Hirose, 2012; Okuzumi et al., 2016)

$$\epsilon_{\rm grow} = \min\left\{1, -\frac{\ln(\Delta v_{\rm pp}/v_{\rm frag})}{\ln 5}\right\}, \tag{3.12}$$

where $\Delta v_{\rm pp}$ is the relative velocity between colliding particles and $v_{\rm frag}$ is the critical fragmentation velocity determined by the mechanical properties of the particles. If $\Delta v_{\rm pp} > v_{\rm frag}$, $\epsilon_{\rm grow}$ is negative, meaning that the single collision results into the fragmentation of colliding particles. Laboratory experiments (e.g., Blum & Wurm 2000) and numerical simulations (e.g., Wada et al. 2013) have shown that the typical value of $v_{\rm frag}$ for silicate aggregates is in the range 1–10 m s^{-1}, with the exact value depending on the size of the grains constituting the aggregates. We change the value from 0.1 to 10 m s^{-1} and investigate how it affects the dust evolution around the dead-zone inner edge. The fragmentation velocity of icy dust particles is known to be higher than that for silicate particles (Wada et al., 2013; Gundlach & Blum, 2015). Because the region beyond the snow line is not our main focus, we simply adopt $v_{\rm frag} = 30$ m s^{-1} for icy particles. With this value of $v_{\rm frag}$, icy particles do not experience catastrophic disruption.

For the components of the relative velocity between colliding particles, we consider the relative velocity due to brownian motion of dust particles $\Delta v_{\rm B}$, disk turbulence $\Delta v_{\rm t}$, azimuthal velocity Δv_ϕ, settling velocity $\Delta v_{\rm z}$ and radial drift velocity $\Delta v_{\rm r}$. Therefore, $\Delta v_{\rm pp}$ is written as

$$\Delta v_{\rm pp} = \sqrt{\Delta v_{\rm B}^2 + \Delta v_{\rm r}^2 + \Delta v_\phi^2 + \Delta v_{\rm z}^2 + \Delta v_{\rm t}^2}. \tag{3.13}$$

Around the dead-zone inner edge, due to the high temperature, the relative velocity is dominated by the velocity originating from the disk turbulence (Ormel & Cuzzi, 2007)

$$\Delta v_{\rm t} = \begin{cases} \sqrt{\alpha} c_{\rm s} \sqrt{\dfrac{1}{1+{\rm St}} + \dfrac{1}{1+\epsilon{\rm St}}}, & {\rm St} > 1, \\ \sqrt{3\alpha {\rm St}} c_{\rm s}, & t_\eta \Omega_{\rm K} < {\rm St} \leq 1, \\ \sqrt{\alpha} c_{\rm s} {\rm Re}_t^{1/4} (1-\epsilon) {\rm St}, & {\rm St} \leq t_\eta \Omega_{\rm K}, \end{cases} \tag{3.14}$$

where ${\rm Re}_{\rm t} = 2\nu/v_{\rm th}\lambda_{\rm mfp}$ is the turbulent Reynolds number, $t_\eta = {\rm Re}_{\rm t}^{-1/2}/\Omega_{\rm K}$ is the turnover timescale of the smallest eddies and $\epsilon = 0.5$ represents the ratio of the Stokes number of colliding particles. Sato et al. (2016) found the best fit value of $\epsilon = 0.5$ for this model which means that the dominant collisions are represented by

collisions of grains with a size ratio of two. The relative velocity originating from the Brownian motion is given as

$$\Delta v_{\rm B} = \sqrt{\frac{16 k_{\rm B} T}{\pi m_{\rm p}}}. \tag{3.15}$$

The relative velocity originating from the differential drift velocities $\Delta v_{\rm r}$, Δv_ϕ and $\Delta v_{\rm z}$ are given as

$$\Delta v_{\rm r} = \left| \frac{2{\rm St}}{1+{\rm St}^2} - \frac{2\epsilon{\rm St}}{1+(\epsilon{\rm St})^2} \right| \eta v_{\rm K}, \tag{3.16}$$

$$\Delta v_\phi = \left| \frac{1}{1+{\rm St}^2} - \frac{1}{1+(\epsilon{\rm St})^2} \right| \eta v_{\rm K}, \tag{3.17}$$

$$\Delta v_{\rm z} = \left| \frac{\rm St}{1+{\rm St}} - \frac{\epsilon{\rm St}}{1+\epsilon{\rm St}} \right| \Omega_{\rm K} h_{\rm d}. \tag{3.18}$$

We also consider the sublimation of silicate and icy components. We assume that almost all silicate particles in a grid sublimate if the temperature in the grid is higher than 1350 K, although in order to stabilize calculations we keep a very tiny amount of dust ($\Sigma_{\rm d} = 10^{-10}\Sigma_{\rm g}$) there. Icy particles are assumed to sublimate on the water snow line, which we define as the radial position where the temperature reaches 160 K. We include this effect by reducing the inward solid mass flux across the snow line by 50%, which is the assumed ice fraction of the solid particles in the outer disk. For simplicity, we ignore the re-condensation of silicate and water ice. The initial dust radius is assumed to be 0.1 μm for the entire region of the disk.

3.3.1.3 Radial temperature profile

We focus on passive protoplanetary disks, where the radiation from the central star dominates. The temperature profile is simply assumed to be the temperature profile of an optically thin disk,

$$T = \epsilon_{\rm emit}^{-1/4} \left(\frac{R_*}{2r} \right)^{1/2} T_*, \tag{3.19}$$

where $\epsilon_{\rm emit} = 1/3$ is a ratio between the emission and absorption efficiencies of dust particles. Although this temperature profile is not valid in the optically thick region, we use Equation (3.19) because our main focus is on the inner-most region where the temperature can be well described by an optically thin passive disk model (Ueda et al., 2017; Flock et al., 2017). The actual temperature profile would depend on the dust distribution and evolve with time, but in the dust-growth simulations, we do not consider the evolution of the temperature structure. As mentioned later, in the

radiative transfer simulations, the vertical structure is iteratively calculated using the temperature structure obtained from the previous simulation to obtain the vertically consistent model. For simplicity, we ignore the effect of accretion heating as the effect remains low for Herbig stars with the given mass accretion rate (Flock et al., 2017).

3.3.1.4 Turbulence

For the turbulent viscosity, we use the α-prescription (Shakura & Sunyaev, 1973)

$$\nu = \alpha c_{\rm s} h_{\rm g}. \tag{3.20}$$

We set α as a function of the midplane temperature as (Flock et al., 2016)

$$\alpha = \frac{(\alpha_{\rm MRI} - \alpha_{\rm dead})}{2}\left[1 - \tanh\left(\frac{T_{\rm MRI} - T}{50\ {\rm K}}\right)\right] + \alpha_{\rm dead}, \tag{3.21}$$

where $T_{\rm MRI} = 1000$ K is a critical temperature to activate MRI (Desch & Turner, 2015), $\alpha_{\rm dead}$ is the value of α in the MRI-inactive region and $\alpha_{\rm MRI}$ is that in the MRI-active region. This description leads to $\alpha \approx \alpha_{\rm MRI}$ for $T \gg T_{\rm MRI}$ and $\alpha \approx \alpha_{\rm dead}$ for $T \ll T_{\rm MRI}$. The value of $\alpha_{\rm dead}$ is quite uncertain, so we change the value from 10^{-4} to 10^{-2} and set $\alpha_{\rm MRI}$ to be 10 times larger than $\alpha_{\rm dead}$.

3.3.1.5 Planetesimal formation

If the dust-to-gas mass ratio is sufficiently high, part of dust particles would potentially be converted into plantesimals via the streaming instability (e.g., Youdin & Goodman 2005). To take this effect into account, in some simulations, if the midplane dust density is higher than the gas density, we convert part of the dust surface density into planetesimals following the approach of Drążkowska et al. (2016):

$$\frac{\partial \Sigma_{\rm plts}}{\partial t} = \zeta \frac{\Sigma_{\rm d}}{T_{\rm K}}, \quad \frac{\partial \Sigma_{\rm d}}{\partial t} = -\frac{\partial \Sigma_{\rm plts}}{\partial t}, \tag{3.22}$$

where $\Sigma_{\rm plts}$ is the planetesimal surface density, $T_{\rm K}$ is the orbital period and $\zeta = 10^{-4}$ is the planetesimal formation efficiency. While Drążkowska et al. (2016) assumed that only particles with ${\rm St} > 10^{-2}$ are converted into planetesimals, we do not set such limitation on the size of dust particles because recent numerical simulations suggest that the streaming instability would occur even for smaller particles (${\rm St} < 10^{-2}$) (Yang et al., 2017).

3.3.2 Results of simulations of dust and gas disk evolution

Figure 3.1 shows the time evolution of the gas and dust disks with different values of $\alpha_{\rm dead}$ and $v_{\rm frag}$. In our disk model for a Herbig type star, the inner rim of dust disk (location where silicate dust particles sublimate) and the dead-zone inner edge are located at ~ 0.5 au and ~ 1 au, respectively.

Figure 1(a) shows the dust and gas surface density for three different time snapshots assuming $\alpha_{\rm dead} = 10^{-3}$ and $v_{\rm frag} = 1$ m s^{-1}. For this model, the inner disk (< 40 au) has nearly reached a steady state. The dust particles remain small and no pileup of dust particles is seen at the dead-zone inner edge even though there is a local pressure maximum. This can be explained by the fact that, when the disk turbulence is strong and/or dust particles are poorly sticky (i.e., fragmentation velocity is small), dust particles keep their size to be so small that they cannot accumulate on the pressure maximum due to turbulent diffusion.

This picture of the disk evolution changes dramatically if one allows the grains to grow further. For $v_{\rm frag} = 10$ m s^{-1} (Figures 1(b), (c) and (d)), dust particles pile up at the dead-zone inner edge. In Figure 1(a), the maximum Stokes number at the dead-zone inner edge is of the order of 10^{-4}, which is ∼100–1000 times smaller than that in Figure 1(b), (c) and (d). Even though there is a dust-pileup in Figure 1(b), the dust-to-gas mass ratio at the midplane remains above unity only for 5×10^4 years. This is because the dust mass accretion rate decreases with time and the trapped dust particles gradually leaks out due to turbulent diffusion. For $\alpha_{\rm dead} = 10^{-4}$ (Figure 1(c)) the dust-to-gas mass ratio at the midplane around the dead-zone inner edge exceeds unity for more than 5×10^5 years.

The evolution of dust and gas disk with the same parameter with Figure 1(c) but including the effect of planetesimal formation is shown in Figure 1(d). In Figure 1(c), the width of the dust-concentrated region at $t = 5 \times 10^5$ year is ~ 1 au, while it is narrower (~ 0.3 au) in Figure 1(d). This is because in Figure 1(d), the mass transfer into planetesimals inhibits a strong dust accumulation. If planetesimal formation occurs, dust particles trapped at the dead-zone inner boundary are converted into planetesimals before they leak out, resulting in the depletion of dust particles inside the dead-zone inner boundary. Figure 1(d) shows large particles (~ 10 cm) between 0.6 and 1 au with a very small surface density ($< 10^{-3}$ g cm^{-3}). This very tiny amount of large particles is leaking out of the dust-pileup. They keep their size large within the timescale we focus on because they hardly collide with each other owing to low dust-to-gas mass ratio.

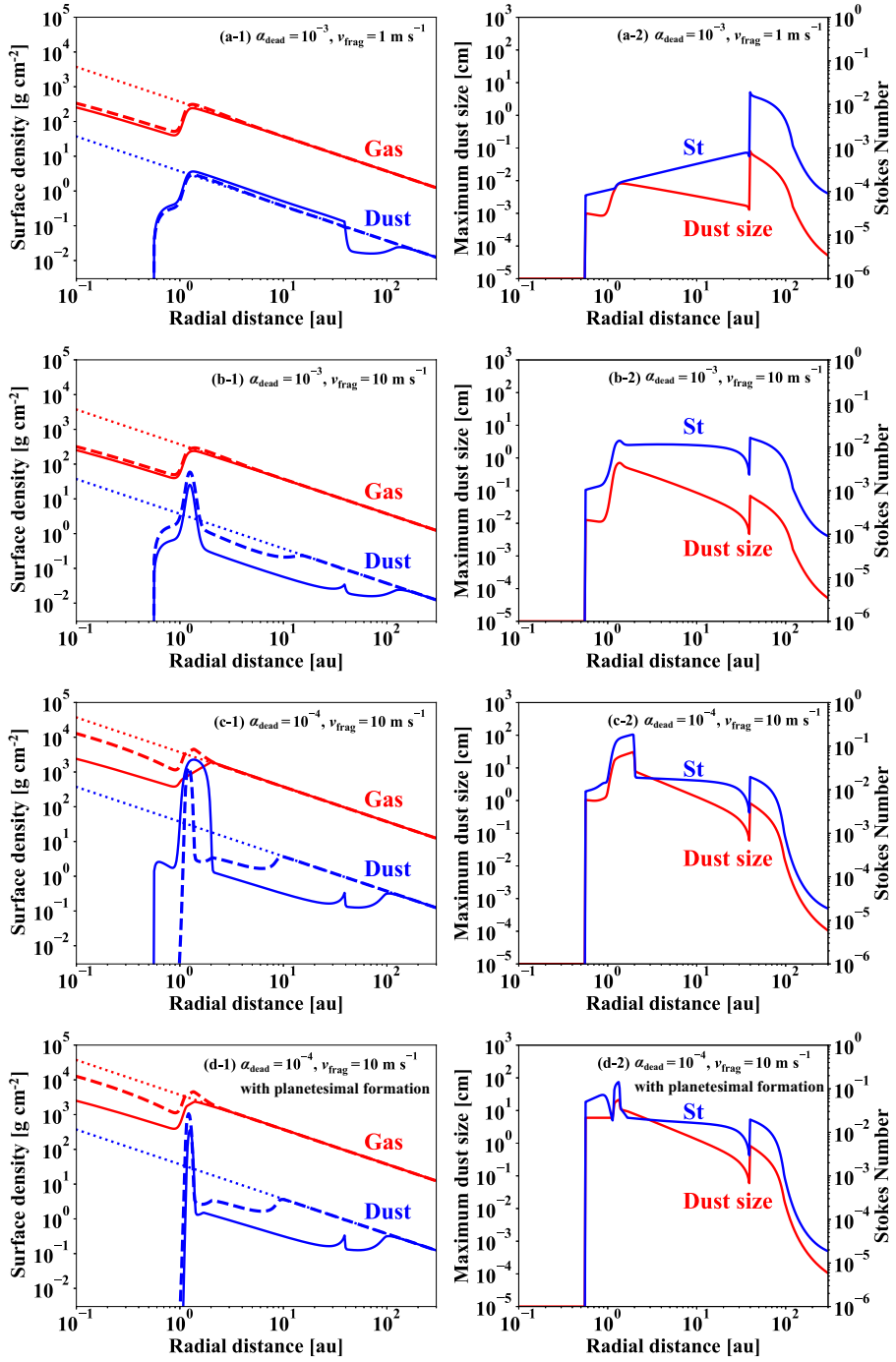

Figure 3.1: Dust and gas surface densities at $t = 0$ yr (dotted), 1×10^4 yr (dashed) and 3×10^5 yr (solid) (left-planels) and the maximum dust radius and the Stokes number at $t = 3\times10^5$ yr (right-planels) for (a) $\alpha_{\rm dead} = 10^{-3}$ and $v_{\rm frag} = 1$ m s^{-1}, (b) $\alpha_{\rm dead} = 10^{-3}$ and $v_{\rm frag} = 10$ m s^{-1}, (c) $\alpha_{\rm dead} = 10^{-4}$ and $v_{\rm frag} = 10$ m s^{-1}, (d) $\alpha_{\rm dead} = 10^{-4}$ and $v_{\rm frag} = 10$ m s^{-1} with planetesimal formation (Equation (3.22)).

In contrast, the outer disk region behind the snow line has not much evolved for the given time output. A unique feature is a drop of the size of dust particles when crossing the ice line (e.g., Birnstiel et al. 2010; Okuzumi et al. 2016). Figure 1(a) and (b) show mm-sized grains at the snow line, while the grains can grow up to cm size at the snow line at 40 au in Figure 1(c) and (d).

The results shown in Figure 3.1 imply that a strong dust-pileup at the dead-zone inner edge only occurs when the dust particles can grow large enough, either due to a reduced turbulent mixing or a higher fragmentation velocity. To confirm this

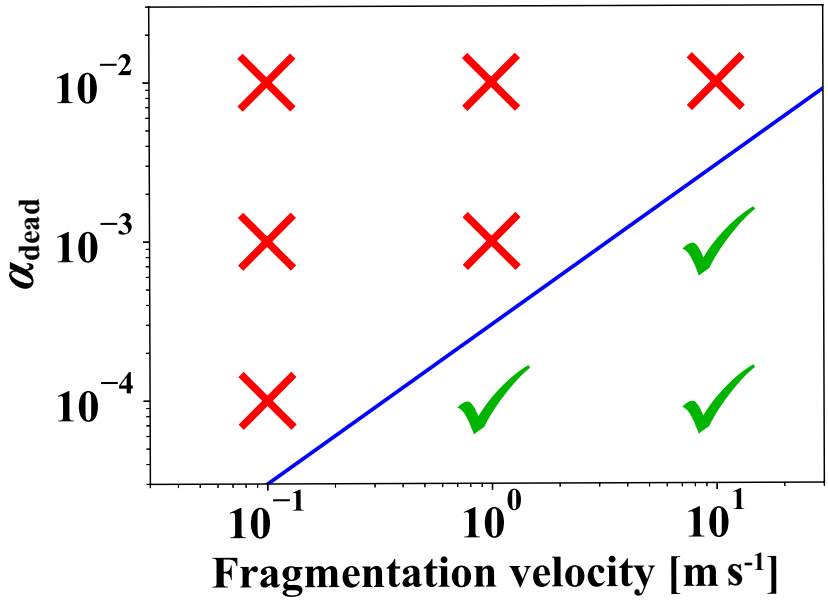

Figure 3.2: Parameter dependence on the dust-pileup at the dead-zone inner edge. The green ticks and red crosses respectively denote the case where the disk has a dust-pileup and no dust-pileup at the dead-zone inner edge. The blue solid line represents the criterion for the dust-pileup given by Equation (3.25).

over a wider parameter space, we summarize in Figure 3.2 the outcome of all our simulations. For $\alpha_{\rm dead} = 10^{-2}$, dust particles cannot pile up on the dead-zone inner edge even if the critical fragmentation velocity of silicate dust particles is 10 m s^{-1}. As mentioned above, for the disk with $\alpha_{\rm dead} = 10^{-3}$ and $v_{\rm frag} = 10$ m s^{-1}, dust particles can pile up on the dead-zone inner edge, but the maximum dust-to-gas mass ratio at the midplane is merely ~ 3 and is kept for less than 5×10^4 years. The total planetesimal mass formed at $t = 6 \times 10^5$ yr is $1 M_\oplus$ for the disk with $\alpha_{\rm dead} = 10^{-3}$ and $v_{\rm frag} = 10$ m s^{-1}, $374 M_\oplus$ for the disk with $\alpha_{\rm dead} = 10^{-4}$ and $v_{\rm frag} = 1$ m s^{-1}, and

$705 M_\oplus$ for the disk with $\alpha_{\rm dead} = 10^{-4}$ and $v_{\rm frag} = 10$ m s^{-1}. It should be noted that the absolute value of the total planetesimal mass depends on how long time the inflow of drifting dust particles continues. In these simulations, we do not consider any truncation mechanism of the inflow such as the gap-opening by an outer giant planet or the disk outer edge.

Here we derive the condition for the dust-pileup at the dead-zone inner edge as a function of $\alpha_{\rm dead}$ and $v_{\rm frag}$ by comparing the radial drift timescale of dust particles $\tau_{\rm drift}$ with the diffusion timescale $\tau_{\rm diff}$. If the diffusion timescale is much larger than the radial drift timescale of dust particles , dust particles can pile up without a significant mass loss due to the diffusion (see also Zhu et al. 2012; Birnstiel et al. 2013). If we assume St $\ll 1$, which is basically valid in the whole disk (see Figure 3.1), the condition can be written as

$$\frac{\tau_{\rm vis}}{\tau_{\rm drift}} \sim \frac{r^2}{\nu}\frac{{\rm St}\eta v_{\rm K}}{r} = \frac{\rm St}{2\alpha}\left|-\frac{\partial \ln p}{\partial \ln r}\right| \gg 1. \tag{3.23}$$

When we assume the absolute value of $\partial \ln p/\partial \ln r$ is an order of unity, Equation (3.23) requires St $\gg \alpha$. Let us estimate the typical value of the Stokes number of dust particles at the dead-zone inner edge. Because the size of dust particles in the inner region of disks is regulated by the collisional fragmentation due to turbulent motion, the size can be estimated by equating the relative velocity originating from the turbulence with the critical fragmentation velocity: $\sqrt{3\alpha {\rm St}}c_{\rm s} = v_{\rm frag}$. Because the dust-pileup occurs within the MRI-suppressed region, i.e. $\alpha = \alpha_{\rm dead}$, the Stokes number of dust particles in the dust-concentrated region is written as

$${\rm St} \approx 10^{-4}\left(\frac{v_{\rm frag}}{1\ {\rm m\ s^{-1}}}\right)^2\left(\frac{\alpha_{\rm dead}}{10^{-3}}\right)^{-1}, \tag{3.24}$$

here we use $T = T_{\rm MRI} = 1000$ K. Equation (3.24) well explain the Stokes number shown in Figure 3.1. Therefore, the critical value of $\alpha_{\rm dead}$ for the dust-pileup at the dead-zone inner edge can be written as a function of $v_{\rm frag}$ as

$$\alpha_{\rm dead} \approx 3\times 10^{-4}\left(\frac{v_{\rm frag}}{1\ {\rm m\ s^{-1}}}\right). \tag{3.25}$$

If $\alpha_{\rm dead}$ is larger than this value, dust particles are unable to pile up on the dead-zone inner edge due to efficient diffusion. In Figure 3.2, we indicate Equation (3.25) by the blue solid line. We find that Equation (3.25) explains the outcomes of all our simulations.

3.4 Radiative Transfer Simulations

The dust wall formed at the dead-zone inner boundary might block off the stellar irradiation and cast a shadow just behind it. In order to investigate this effect on the disk structure and its appearance, we perform radiative transfer calculations with the Monte Carlo radiative transfer code RADMC-3D (Dullemond et al., 2012).

3.4.1 Radiative transfer models

We perform radiative transfer simulations using the dust distributions at $t = 3 \times 10^5$ yr shown in Section 3.3.2. Table 3.1 summarize the disk models that we used in the radiative transfer simulations.

Table 3.1: Disk models used in the radiative transfer simulations

Model	$\alpha_{\rm dead}$	$v_{\rm frag}$ [m s^{-1}]	Note
Model 1	10^{-3}	1	$0.01\Sigma_{\rm d}$
Model 2	10^{-3}	10	
Model 3	10^{-4}	10	
Model 4	10^{-4}	10	Equation (3.22)

Model 1 ($\alpha_{\rm dead} = 10^{-3}$ and $v_{\rm frag} = 1$ m s^{-1}) has no dust-pileup, while the others have a dust-pileup at the dead-zone inner edge. In model 2, 3 and 4, we directly use the dust distribution shown in Figure 3.1, while we have a modification in model 1. In model 1, the dust surface density is reduced by a factor of 100 from that obtained by the dust-growth simulation to avoid non-convergence (see Section 3.5). The effect of planetesimal formation (Equation (3.22)) is included only in model 4.

The radial coordinate ranges from 0.03 au to 1000 au and is logarithmically divided into 100 grids per one decade. The theta coordinate (angle from z-axis) ranges from 60° to 90° and is linearly divided into 96 grids. We assume that the disk is axisymmetric. For each radial bin, we assume a dust size distribution ranging from 0.1 μm to $a_{\rm max} = (3m_{\rm p}/4\pi\rho_{\rm int})^{1/3}$ that follows a power law with a index of -3.5 similar to the MRN distribution (Mathis et al., 1977). In order to allow settling of different sizes of dust particles to a different height in the disk, the dust size distribution is divided into five groups, < 0.3, 0.3–3, 3–30, 30–300, 300–3000 μm, having a representative size of 0.1, 1, 10, 100, 1000 μm, respectively. We ignore the contribution from dust particles larger than 3000 μm because it has little effect on the result within the range of wavelength we focus on. For each dust size bin, the dust scale height is calculated by Equation (3.11).

The dust opacities are computed using Mie theory. For simplicity, dust particles are assumed to be a single species of amorphous silicate ($Mg_{0.7}Fe_{0.3}SiO_3$). The optical constants are taken from the Jena database[1] (Jaeger et al., 1994; Dorschner et al., 1995).

We assume isotropic scattering for simplicity and employ the modified random walk approximation (Min et al., 2009) in order to treat a very optically thick region owing to the dust-pileup. The central star is treated as a finite-size sphere. The radiative transfer simulations are iteratively performed to obtain a robust structure of the disk and we use 10^8 photon packages for each simulation. In Appendix 3.8.2, we show that the number of photon packages of 10^8 is large enough to obtain a well converged temperature profile. The vertical density structure was iterated based on the thermal structure obtained from previous radiative transfer calculation following the approach of Kama et al. (2009). The iteration is performed until the deviation of the midplane temperature in each iteration is less than 10%.

3.4.2 Results of radiative transfer simulations

3.4.2.1 Radial intensity profile

Figure 3.3 shows the radial intensity profiles at 1.65μm (H-band) for the disks with different values of $\alpha_{\rm dead}$ and $v_{\rm frag}$. We clearly see a large bump in the radial intensity profile around 0.9 au in model 1, 0.6 au in model 2 and 3 and 1.1au in model 4. This bright ring is caused by the direct irradiation on the inner rim of the dust disk (see Dullemond & Monnier 2010 for review). In model 1, because we artificially reduced the dust surface density, the radial optical depth for the stellar light is smaller than that in model 2 and 3, and hence the dust rim occurs at a larger distance from the star. Model 4 also has a dust rim at a larger distance ($\sim$ 1.1au). This is because dust particles are converted into planetesimals at the dead-zone inner boundary before they leak out of the dead-zone inner boundary, resulting into the depletion of dust particles inside the dead-zone inner boundary.

Although there is a dust wall at the dead-zone inner boundary in model 2, 3 and 4, it is hard to distinguish it from the bright inner rim of dust disk because the separation between the inner rim and the dust wall is almost comparable to the width of the inner rim. Especially in model 4, the dust wall at the dead-zone inner boundary coincides with the inner rim of the dust disk because of the depletion of dust particles inside the dead-zone inner boundary.

[1] `http://www.astro.uni-jena.de/Laboratory/OCDB/`

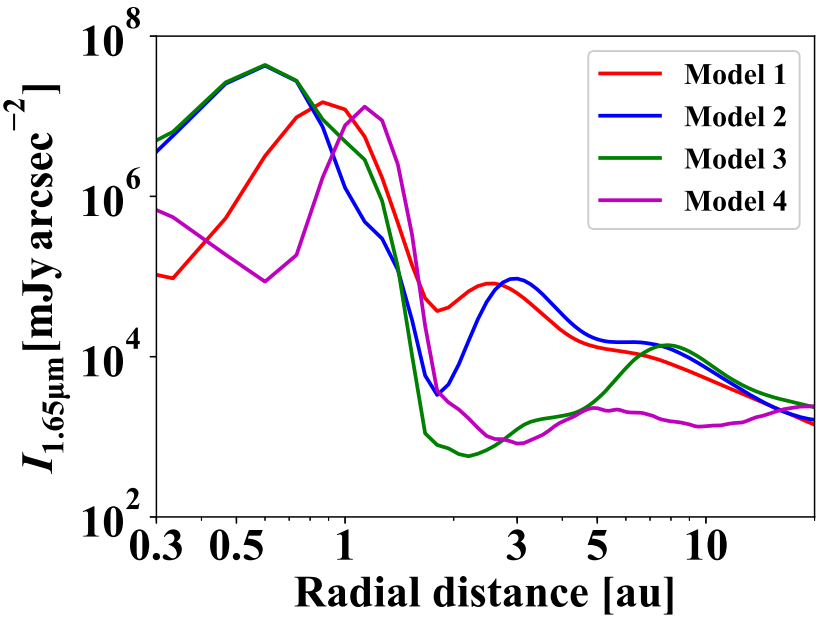

Figure 3.3: Radial intensity profiles at 1.65 μm for the disks with different values of $\alpha_{\rm dead}$ and $v_{\rm frag}$. The intensity is the value at the major axis of the disk (along the long part of the ellipse) with inclination of 45°. *red*: $\alpha_{\rm dead} = 10^{-3}$ and $v_{\rm frag} = 1$ m s^{-1} with reducing the dust surface density by a factor of 100, *blue*: $\alpha_{\rm dead} = 10^{-3}$ and $v_{\rm frag} = 10$ m s^{-1}, *green*: $\alpha_{\rm dead} = 10^{-4}$ and $v_{\rm frag} = 10$ m s^{-1}, *magenta*: $\alpha_{\rm dead} = 10^{-4}$ and $v_{\rm frag} = 10$ m s^{-1} with planetesimal formation effect.

The most important difference in the radial intensity profile of the four models is in the deep intensity dip beyond 1 au. This is an indication of a shadow mainly caused by the dust-pileup at the dead-zone inner edge, with small additional contribution from the puffed-up inner rim. In model 3, the intensity decreases by five orders of magnitude around the dead-zone inner edge from inside out and the shadowed region extends to $\sim$ 8 au. In this region, the angle between the disk surface and incident stellar light is nearly zero, meaning that disk surface does not receive direct irradiation from the central star (see Figure 3.15(a) in Appendix 3.8.3). In model 4, because the dust wall acts even as a inner rim of the dust disk, the combined effect results in the shadow extending to $\sim$ 20 au.

The effect of the dust shadow is more significant for smaller $\alpha_{\rm dead}$ and larger $v_{\rm frag}$. There are two reasons for this trend. Firstly, smaller $\alpha_{\rm dead}$ and larger $v_{\rm frag}$ lead to more efficient trapping of dust particles as mentioned in Section 3.3.2. Secondly, smaller $\alpha_{\rm dead}$ and larger $v_{\rm frag}$ result in a smaller amount of small particles behind the dead-zone inner edge because the particles grow and drift inward without catastrophic

fragmentation. As explained below, this effect strongly depends on these parameters. With the assumption that the surface number density of dust particles per unit particle size is proportional to $a^{-3.5}$, one can show that the surface number density in each dust-size bin is approximately proportional to $\Sigma_{\rm d} a_{\rm max}^{-1/2}$. The dust surface mass density is approximately inversely proportional to the maximum Stokes number, which is proportional to $a_{\rm max}$. Therefore, the number of small particles behind the dead-zone inner edge is proportional to $a_{\rm max}^{-3/2}$. If we combine this with Equation (3.24), the number of small particles in the region just behind the dead-zone inner edge is proportional to $\alpha_{\rm dead}^{-3/2} v_{\rm frag}^{3}$, which indicates that the width and depth of the dust shadow is sensitive to these parameters.

3.4.2.2 Synthetic images

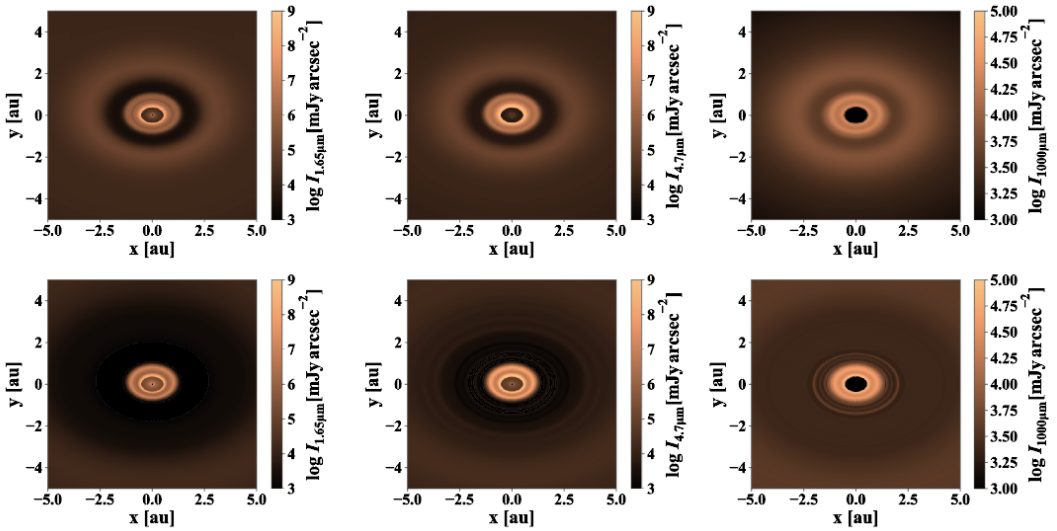

Figure 3.4: Synthetic images of the inner region of disks for model 2 (top) and 3 (bottom) viewed 45° from face-on. The intensity maps are at wavelengths 1.65 (left), 4.7 (center) and 1000 μm (right) in log-scale.

To provide a realistic view of the inner region of disks, we constructed synthetic images of our models. Figure 3.4 shows the images of the inner region of disks with model 2 and 3 for an inclination of 45°. The top panels correspond to model 2 and the bottom panels to model 3. The images are at wavelengths 1.65, 4.7 and 1000 μm from left to right. In model 2, we observe a sharp shadow with a width of $\sim$ 1 au behind the dead-zone inner edge, while the shadow is less sharp in model 3 due to its large width ($\sim$ 9 au). The dust halo in front of the inner rim of dust disk is brightest

at wavelength 1.65 μm, while the dust rim itself is brighter at 4.7 μm as described by Flock et al. (2016). At longer wavelengths, the width of shadow is smaller. When seen at 1 mm, the brightness of the shadowed region differs only by a factor of < 5 between models 2 and 3. At 1.65 μm, in contrast, the brightness differs by two orders of magnitude.

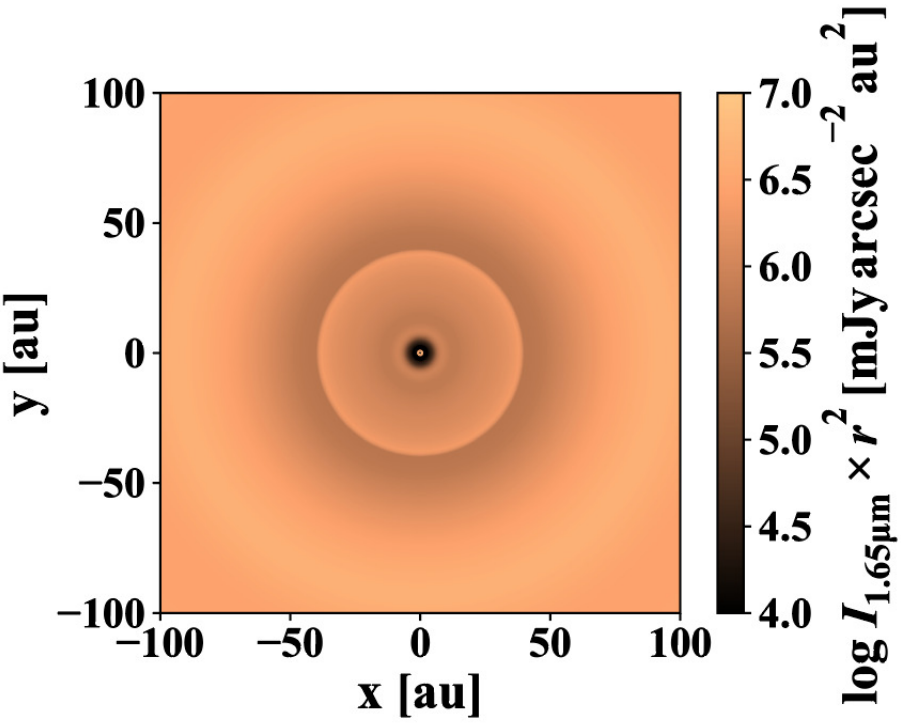

Figure 3.5: Intensity map of the disk model 3 with the field width of 200 au at wavelength 1.65 μm viewed from face-on. The intensity is multiplied by r^2 to compensate for the stellar flux attenuation.

We also provide a intensity map of the disk model 3 at 1.65 μm with the field of view of 200 au wide (Figure 3.5, the intensity is multiplied by r^2). Figure 3.5 shows that the intensity distribution has a central hole of 10 au in radius, corresponding to the shadow casted by the dust-pileup. In addition to that, we observe another shadow extending from 40 au outward. This extended outer shadow is caused by the water snow line (see also Pinilla et al. 2017). Outside the snow line, dust particles can grow large and settle onto the midplane, while dust particles just inside the snow line are smaller due to ice sublimation and fragmentation. The abrupt change in the size of dust particles around the snow line creates a shadow behind it.

3.4.2.3 Midplane temperature

In Figure 3.6, we show the midplane temperature derived from the thermal Monte Carlo simulations done by RADMC-3D (Dullemond et al., 2012). In model 1, an

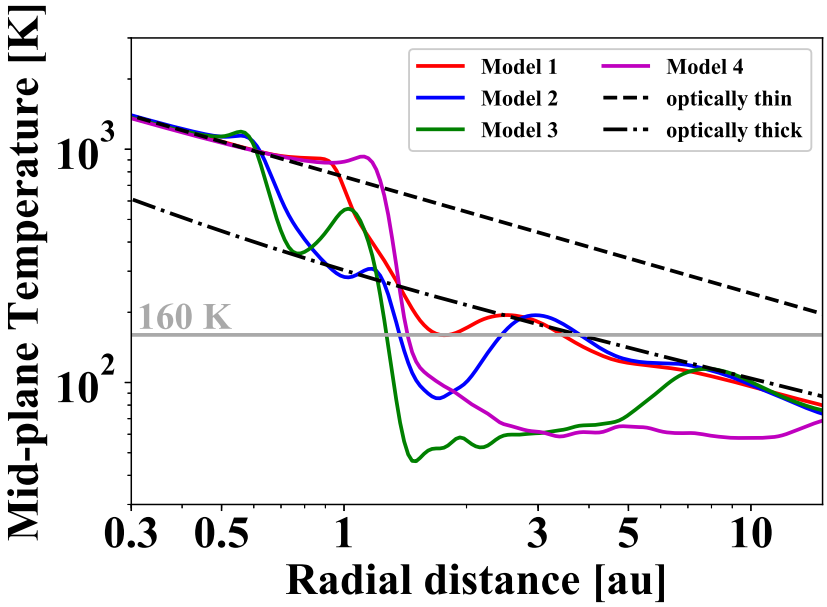

Figure 3.6: Midplane temperature profile of the disks with different values of $\alpha_{\rm dead}$ and $v_{\rm frag}$. *red*: $\alpha_{\rm dead} = 10^{-3}$ and $v_{\rm frag} = 1$ m s^{-1}, *blue*: $\alpha_{\rm dead} = 10^{-3}$ and $v_{\rm frag} = 10$ m s^{-1}, *green*: $\alpha_{\rm dead} = 10^{-4}$ and $v_{\rm frag} = 10$ m s^{-1}, *magenta*: $\alpha_{\rm dead} = 10^{-4}$ and $v_{\rm frag} = 10$ m s^{-1} with planetesimal formation. Black dashed and dot-dashed lines denote the temperature profile given by Equation (3.19) and that of the optically thick disk (Equations (11)-(15) in Ueda et al. 2017 with $z_{*,\rm D} = 0.5h_{\rm g}$). Gray horizontal line corresponds to the sublimation temperature of water ice ($T = 160$ K).

optically thin inner disk connects smoothly to an optically thick outer disk, with a shallow dip in the temperature profile at ~ 2 au caused by a shadow. As mentioned above, there is no dust-pileup in model 1, so this shadow simply originates from the puffed-up inner rim (Dullemond et al., 2001b; Flock et al., 2016). In model 2, 3 and 4, we observe a wide dip in the midplane temperature behind ~ 1 au. Especially for model 3 ($\alpha_{\rm dead} = 10^{-4}$ and $v_{\rm frag} = 10$ m s^{-1}), the temperature in the shadowed region has a minimum of as low as 40 K. In Appendix 3.8.3, we examine the effect of scattering by switching off it and find that the minimum temperature in the shadowed region is insensitive to scattering.

Due to the shadowing effect, the location of the water snow line is completely different from what is expected from the temperature profiles of smooth disks. Assum-

ing the water sublimation temperature of 160 K, the water snow line in the smooth, optically thin (with an assumption that grains behave as a black body) and thick disks is located at $\approx$ 20 au and $\approx$ 3 au, respectively. In comparison, the water snow line in model 3 and 4 lies at $\approx$ 1.3 au, which is just behind the dead-zone inner edge. In model 2, there are three water snow lines located respectively at $\approx$ 1.3, 2 and 4 au because of the local temperature dip lying at 1–2 au. These multiple snow lines would affect the evolution of dust particles through the sublimation and recondensation of water ice as we discuss in Section 3.6.

3.4.2.4 Spectral energy distribution

It is known that the spectral energy distribution (SED) of the Herbig Ae stars can be divided into two groups (Meeus et al. 2001). The first one has an almost flat SED in the mid-infrared wavelength (so-called group I) and the second one has a SED with a strong decline towards the far-infrared wavelength (group II). The difference in two groups is thought to come from the self-shadowing by the inner rim of the dust disk: disks with high optical depth turn out to be flaring and have a strong far-infrared emission, while disks with an optical depth below a certain threshold drop into the shadow of their own puffed-up inner rim and are weak in the far-infrared (Dullemond & Dominik 2004).

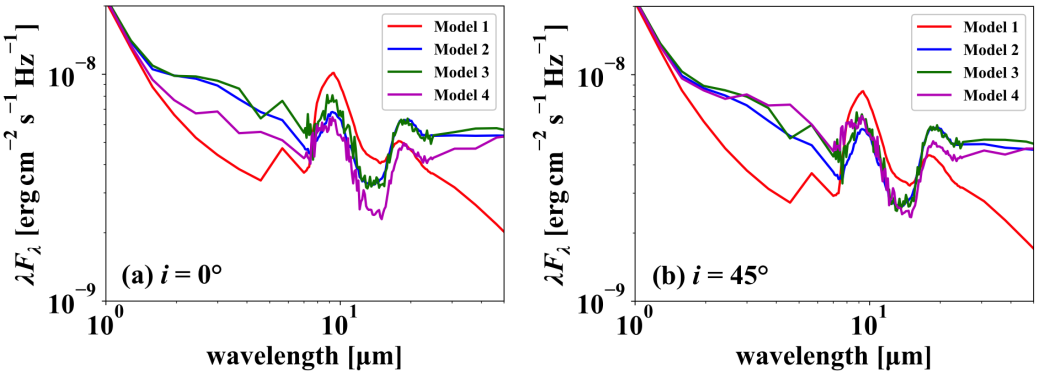

Figure 3.7: Spectral energy distribution of the disks with inclination of (a) 0° and (b) 45°. *red*: $\alpha_{\rm dead} = 10^{-3}$ and $v_{\rm frag} = 1$ m s^{-1}, *blue*: $\alpha_{\rm dead} = 10^{-3}$ and $v_{\rm frag} = 10$ m s^{-1}, *green*: $\alpha_{\rm dead} = 10^{-4}$ and $v_{\rm frag} = 10$ m s^{-1}, *magenta*: $\alpha_{\rm dead} = 10^{-4}$ and $v_{\rm frag} = 10$ m s^{-1} with planetesimal formation.

Figure 3.7 shows the spectral energy distribution of the disks with different values of $\alpha_{\rm dead}$ and $v_{\rm frag}$. As you can see, the disk with $\alpha_{\rm dead} = 10^{-3}$ and $v_{\rm frag} = 1$ m s^{-1}

(Model 1) is less luminous in near and far-infrared wavelength and the SED belongs to group II. This is simply because we artificially reduce the dust surface density by a factor of 100. We found that although disk model 2 and 3 have a shadow, the spectral energy distributions of these disk models do not so different between each other and they look belonged to group I, implying that the shadow casted by the dust-pileup does not related to the group I and II classification. The disk model 4 is less luminous in near-infrared wavelength compared to the disk model 2 and 3. Since the edge of dust disk in model 4 is truncated by the dust-pileup, the shape of disk edge is like a verticall wall. If we look at the vertical wall from the face-on view (Figure 3.7(a)), there is almost no emission from the wall since we cannot see the illuminated side of the wall. If the disk is inclined (Figure 3.7(b)), the disk is brighter in near-infrared wavelength than the disk with no-inclination since the side of the wall can be observed (e.g., Dullemond & Monnier 2010). The disk model 4 is less luminous also in far-infrared wavelength compared to the disk model 2 and 3. This is because of the shadowing effect but the difference between these models is only a factor of 10%. The small difference in the SED suggests that it is hard to identify it from the SED.

3.5 Waves on the Disk Surface

In this section, we show the results of the radiative transfer simulations of model 1 without the reducing factor for the dust surface density (in other words, we use the original dust distribution obtained from the dust-growth simulation). In this model, we observe oscillatory behavior in the temperature structure probably connected to the so-called thermal wave instability (D'Alessio et al., 1999; Dullemond, 2000; Watanabe & Lin, 2008). For this reason, the temperature profile does not relax into a steady state (see more details in Appendix 3.8.1).

Figure 3.8 illustrates the oscillatory behavior of the temperature profile. We here show the midplane temperature at the 17th to 30th iteration steps. We see that the temperature structure is stable in the innermost region (< 1 au) and in the outermost region (> 100 au), but oscillates in the intermediate region (1 au $< r < 100$ au). The oscillatory behavior is caused by waves propagating inward along the disk surface as reported by Watanabe & Lin (2008) and Min et al. (2009). Figure 3.9 shows the intensity profiles at wavelength $1.65\,\mu$m at the 17th to 30th iteration steps. We see that the shadows and bright ring-like structures in the radial intensity profile move inward and decay around 2 au. Once a bump is created on the surface by the perturbation,

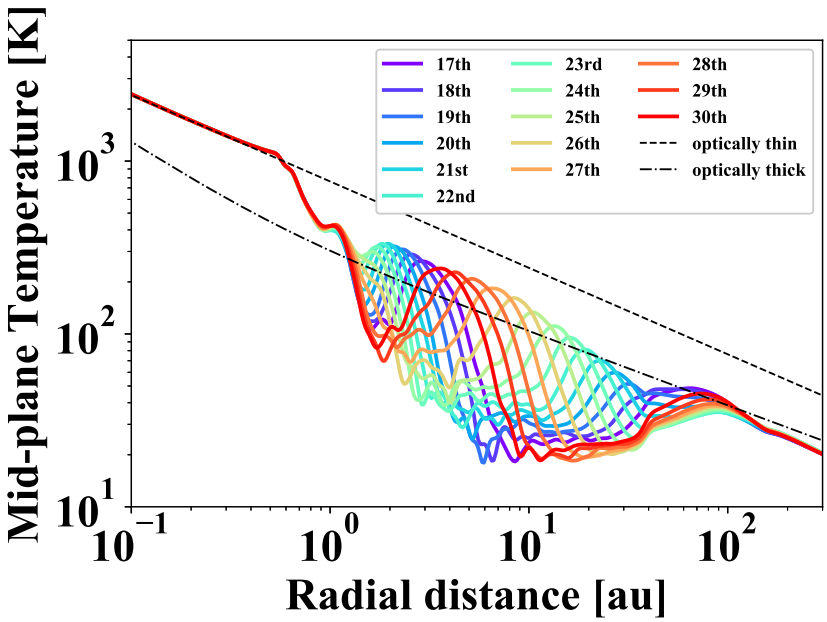

Figure 3.8: Midplane temperature of model 1 without the reducing factor for the dust surface density at the 17th to 30th iteration steps. Black dashed and dot-dashed lines are the same as in Figure 3.6.

the illuminated front side of the bump receives more stellar light and the shady back side of the bump receives insufficient flux. At the illuminated side, the disk surface puffs up further as the midplane temperature increases, resulting in further decrease in the temperature at the back side (Figure 3.10). The oscillatory behavior is not related to the shadow casted by the water snow line ($\sim$ 40 au, see also Figure 3.5). We confirmed that the oscillatory behavior still exists even without the water snow line.

The reason why only model 1 shows the oscillatory behavior is not clear, but it might be linked with the optical thickness. Model 1 has the highest optical depth in our models because of efficient fragmentation of dust particles. We found that in model 1, the amplitude of the oscillation decreases as the dust surface density is reduced. And also we confirmed that even in the other models, the oscillatory behavior is seen if we artificially increase the dust surface density by a factor of 30–100.

We remind that our radiative transfer simulations assume hydrostatic equilibrium of vertical structure and calculate equilibrium temperature structure for a given dust distribution at each iteration step, meaning that our approach does not treat the time evolution of the instability and does not necessarily give us the realistic behavior of

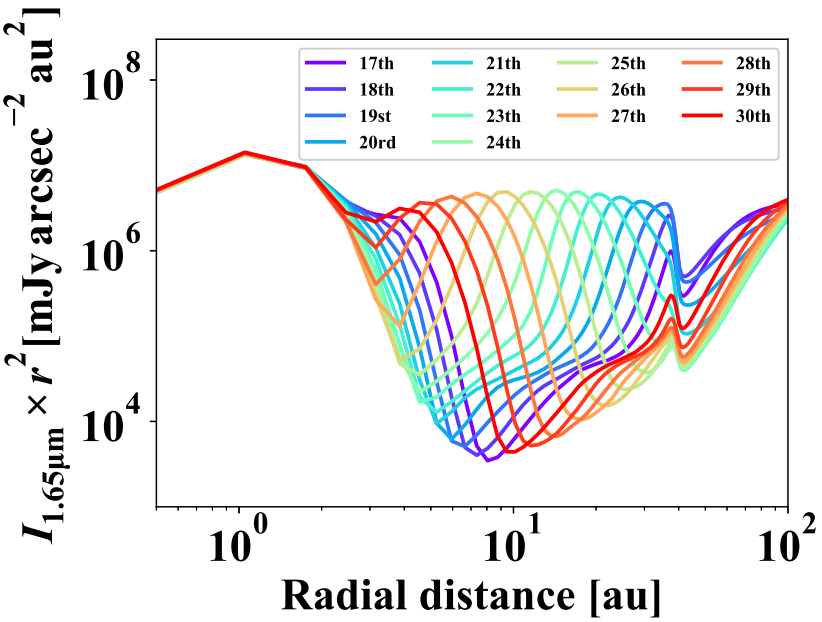

Figure 3.9: Radial intensity profile of model 1 without the reducing factor for the dust surface density at the 17th to 30th iteration steps. The intensity is the value at the major axis of the disk with inclination of 45°. The intensity is multiplied by r^2 to compensate for the stellar flux.

it. In order to know the realistic behavior of the instability, it is important to calculate the vertical heat diffusion and hydro dynamics time-dependently because the height of the disk surface where the stellar irradiation is received depends on the midplane temperature.

3.6 Discussion

3.6.1 Implications for planet formation

We demonstrated that the total mass of planetesimals formed at the dead-zone inner edge strongly depends on the turbulence strength and the critical fragmentation velocity. As we mentioned in Section 3.3.2, the total planetesimal mass is $1 M_\oplus$ for disk with $\alpha_{\rm dead} = 10^{-3}$ and $v_{\rm frag} = 10$ m s^{-1}, while it is $705 M_\oplus$ for disk with $\alpha_{\rm dead} = 10^{-4}$ and $v_{\rm frag} = 10$ m s^{-1}. The large difference in the total planetesimal mass caused by the difference in the turbulence strength might link with the difference in the formation of the solar system and super-earth systems. Our results suggest that systems with low-mass terrestrial planets such as the solar system would form in the disk with rel-

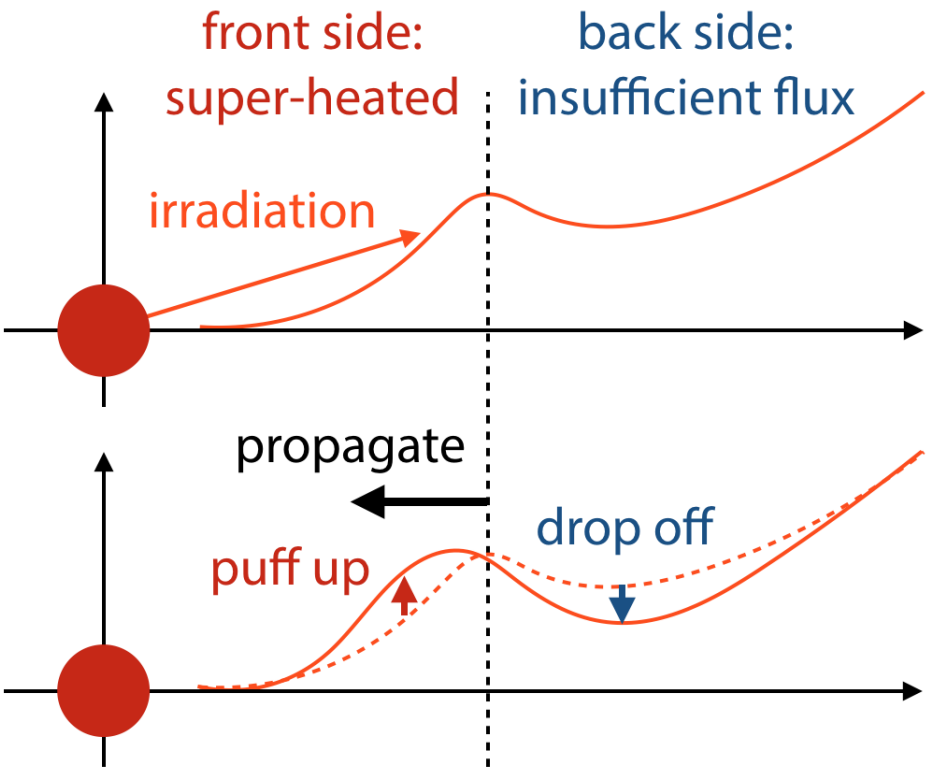

Figure 3.10: Schematic of the thermal wave instability. The illuminated front side of the bump on disk surface receives more stellar light and the shady back side of the bump receives insufficient flux. As the midplane temperature increases at the illuminated side, the disk surface at the illuminated side puffs up further, resulting in further decrease in the temperature at the back side.

atively strong turbulence ($\alpha_{\rm dead} \gtrsim 10^{-4}$), while systems with super-earths would form in the disk with weak turbulence ($\alpha_{\rm dead} \lesssim 10^{-4}$). Recent 3D MHD simulations suggest that the turbulence strength in the dead-zone is weaker than 10^{-4} (e.g., Gressel et al. 2015; Flock et al. 2017), indicating that super-earth systems should be more common than systems like the solar system. Although the dead-zone inner edge lies much closer to the central star ($\sim$ 0.1 au) for T-Tauri disks, Ogihara et al. (2018) showed that outward migration of planetesimals induced by the disk wind may have led to the formation of terrestrial planets in the solar system.

The non-monotonic radial temperature profile caused by the shadow would affect the water mass fraction of inner planets. Grimm et al. (2018) showed that in the TRAPPIST-1 system, planet d has a relatively low density ($\sim$ 3.4 g cm^{-3}) while the other outer planets has higher density ($\sim$ 4–5.6 g cm^{-3}). This density distribution suggests that planet d might have a higher water mass fraction ($>$ 5%) than that of

the other outer planets (Grimm et al., 2018). The inner icy region caused by the shadow might explain the origin of water in the inner planet.

3.6.2 Feedback from the shadows on dust growth

As shown in Section 3.4.2.3, the shadows affect the temperature structure and the resultant temperature differs considerably from that used in the dust growth simulations. In particular, in models 2, the shadow causes a local dip of the midplane temperature below the ice-sublimation temperature, producing two snow line in addition to the one lying at $\approx$ 4 au that would be present without the shadow. The multiple water snow lines would result into the multiple bright and dark rings in millimeter and infrared observations as proposed by Pinilla et al. (2017). If icy dust particles recondense in the shaded region, the particles can grow larger and settle down to the disk midplane, which would enhance the shadowing effect by lowering the local disk surface.

The thermal wave instability would also affect the evolution of dust particles. As shown in Section 3.5, the thermal waves create the positive temperature gradient in front of the peak. If the pressure gradient is positive, dust particles drift outward. In our simulations, the sign of pressure gradient does not be positive but the absolute value is less than unity (see Appendix 3.8.1), indicating that the thermal waves might help dust particles to grow larger beyond the radial drift barrier. Investigation of these possibilities requires dust growth simulations coupled with radiation hydrodynamical calculations, which will be the subject of future work.

3.6.3 Implications for disk observations

As shown in Figures 3.3, it is not easy to directly detect a bright ring structure originating from the dust-pileup at the dead-zone inner edge because it is too close to the inner rim. However, the shadow casted by the dust-pileup would potentially appear in the observations.

Millan-Gabet et al. (2016) examined the SEDs and near- and mid-infrared visibilities of 11 T-tauri and Herbig stars and showed that the classical "star + inner dust rim + flared disk" model strongly fails to simultaneously reproduce the SEDs and visibilities. In order to explain the discrepancy, Millan-Gabet et al. (2016) proposed that the disks should have the "second bright ring" located at $\sim$ 1–7 au. Although the inferred temperature of the second dust rim has large uncertainty and ranges from 800 K to 1750 K, the dust-pileup at the dead-zone inner edge could potentially be one possible

explanation. As we mentioned in section 3.4.2.4, to identify the detailed feature of the dead-zone inner edge from only SED is difficult. Therefore, the comprehensive understanding of not only SED but also the infrared visibilities and direct imaging is necessary to unveil the inner disk morphology. Future high resolution observations at (mid-)infrared wavelength using such as VLTI/MATISSE, E-ELT and TMT will allow us to directly compare our models with the observations. For example, E-ELT/METIS (e.g., Brandl et al. 2014) would have an angular resolution of 5 mas at a wavelength of 10 μm, which provides us images of the inner region of disks at a distance of 100 pc with the spatial resolution of 0.5 au.

The thermal wave instability also creates shadows and ring-like structures on the disk surface. Recent infrared observations have revealed that many circumstellar disks have ring-like structures on its surface (e.g., Avenhaus et al. 2018; Bertrang et al. 2018). Although such structures are sometimes interpreted as an evidence of on going formation of giant planets, the thermal wave instability would be another explanation. The disk around TW Hya would be a nice example having three bright ring-like structures (van Boekel et al., 2017; Akiyama et al., 2015) possibly caused by the thermal wave instability. One possible way to distinguish the origins of these rings is to measure the gas surface density profile by using molecular line emission (e.g., $C^{18}O$, Nomura et al. 2016). The gas surface density must have gaps if the shadows and rings are caused by planets, while the thermal wave instability does not create large gaps in the gas surface density profile since it is associated with the change in the temperature structure.

3.7 Summary

We performed simulations of one-dimensional dust and gas disk evolution with fully including the backreaction from dust to gas to investigate the observational features of a dust-pileup at the dead-zone inner edge. Around the dead-zone inner edge, dust particles are easy to fragment into small particles because of high speed collisions due to the turbulent motion, which interferes with the dust-pileup. We demonstrated that a strong dust pile-up at the dead-zone inner edge occurs only for condition where the Stokes number of dust particles is much larger than the turbulence strength in the dead-zone. Based on the fact that the Stokes number at the dead-zone inner edge is determined by the turbulence induced fragmentation, we derived the condition for the dust-pileup as a function of the critical fragmentation velocity of silicate dust particles and the turbulence strength, and found that if the critical fragmentation velocity

is 1 m s^{-1}, the turbulence parameter in the dead-zone needs to be lower than 3×10^{-4} for dust trapping to operate. The total mass of planetesimals formed at the dead-zone inner boundary is quite sensitive to the turbulence strength, which might explain the diversity in the mass of the inner planets such as super-earths and terrestrial planets in our solar system.

Using the dust distribution obtained above, we also performed the radiative transfer simulations with RADMC-3D to construct models of the inner region of protoplanetary disks including the effect of the dust-pileup. We found that if dust particles strongly concentrate at the dead-zone inner edge, the dust-pileup acts as an optically thick wall, casting a 10 au-scale shadow directly behind the dead-zone inner edge. The shadow significantly reduces the midplane temperature. The resultant temperature profile suggests that the water snow line could be much closer to the central star and potentially creates multiple water snow lines.

Even if dust particles do not pile up on the dead-zone inner edge owing to efficient fragmentation, waves are naturally excited on the disk surface, possibly by the so-called thermal wave instability, creating shadows and ring-like structures on the disk surface. These ring-like structures might account for the bright rings seen in the scattered light images of some disks, including that of TW Hya (van Boekel et al., 2017). The waves create a positive temperature gradient in front of the peak, which might help dust particles to grow larger beyond the radial drift barrier.

Future high resolution observations at (mid-)infrared wavelength using such as VLTI/MATISSE, E-ELT and TMT will allow us to directly compare our models with the observations.

3.8 Appendix

3.8.1 Details of the oscillatory behavior

In this appendix, we provide the details of the oscillatory behavior shown in Section 3.5. Figure 3.11 shows the midplane temperature at 3 au, which is within the unstable region. The temperature oscillates around 150 K with an amplitude of 130 K with a period of 14 iterations. We confirmed that the periodic oscillation does not converge at least within 80 iterations.

Figure 3.12 shows the logarithmic pressure gradient $\partial \ln p / \partial \ln r$ in the simulation after 20 iterations. The local pressure maximum around 1 au is associated with the dead-zone inner edge. In addition to that, there are two peaks in $\partial \ln p / \partial \ln r$ around $\sim$ 2 au and $\sim$ 20 au respectively. These peaks correspond to the illuminated side of

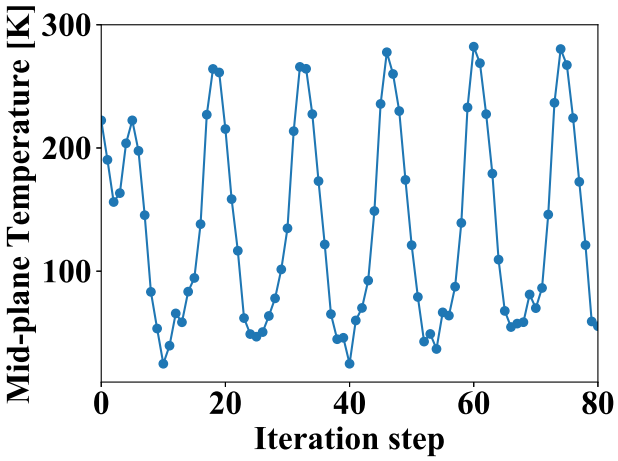

Figure 3.11: Midplane temperature at 3 au of model 1 without the reducing factor for the dust surface density at each iteration step.

the waves on the disk surface. The intense irradiation onto the illuminated side of the waves creates the positive temperature gradient which makes the disk gas rotates with Keplerian frequency. When the pressure gradient is negative/positive, dust particles drift inward/outward. Although the value of $\partial \ln p / \partial \ln r$ at these peaks is not positive, the absolute value is 4–6 times smaller than the fiducial value (~ 3).

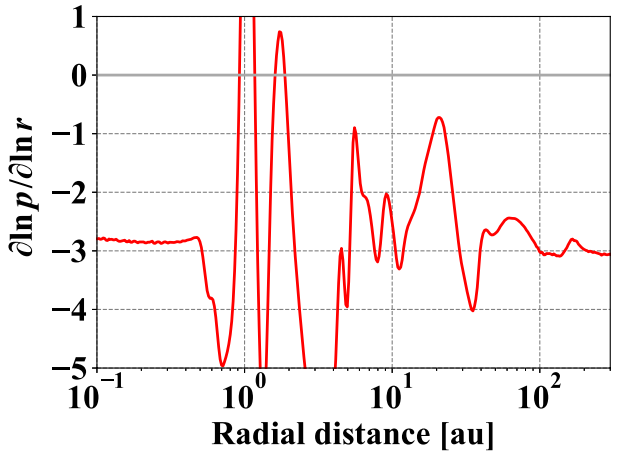

Figure 3.12: Logarithmic pressure gradient $\partial \ln p / \partial \ln r$ in the simulation after 20 iterations. The horizontal gray solid line denotes $\partial \ln p / \partial \ln r = 0$ where the direction of the dust radial motion is reversed.

3.8.2 Convergence of the Thermal Monte Carlo simulation

We used 1×10^8 photon packages for each thermal Monte Carlo simulation. In order to investigate if the thermal Monte Carlo simulations converge well, we additionally performed simulations with 2×10^9 photon packages, which is 20 time higher than fiducial. Figure 3.13 shows the midplane temperature profile for disk model 3 ob-

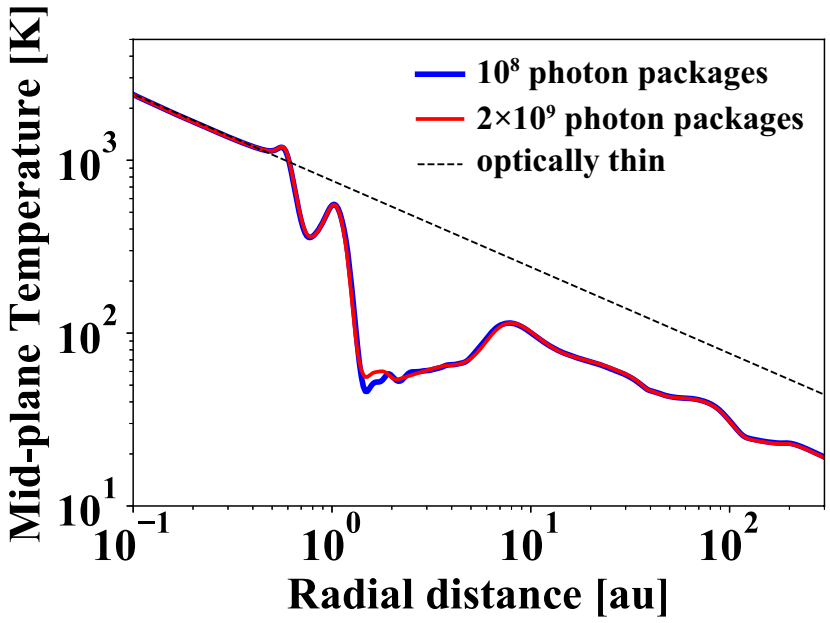

Figure 3.13: Midplane temperature for disk model 3 obtained from the thermal Monte Carlo simulations using 1×10^8 (blue) and 2×10^9 (red) photon packages. The black dashed line denotes the temperature profile given by Equation (3.19).

tained from the thermal Monte Carlo simulations for the two different numbers of photon packages. We find no significant difference between the two simulation results, indicating convergence. We also confirmed that the number of photon packages of 1×10^8 is large enough to obtain a well converged temperature profile for the other disk models.

3.8.3 Effect of Scattering

In this section, we examine how dust scattering affects the temperature structure of the disk. Even if the disk cannot receive the direct irradiation from the star, photons scattered from the upper layer could heat the disk interior. In order to investigate the effect of scattering, we performed radiative transfer simulations with scattering

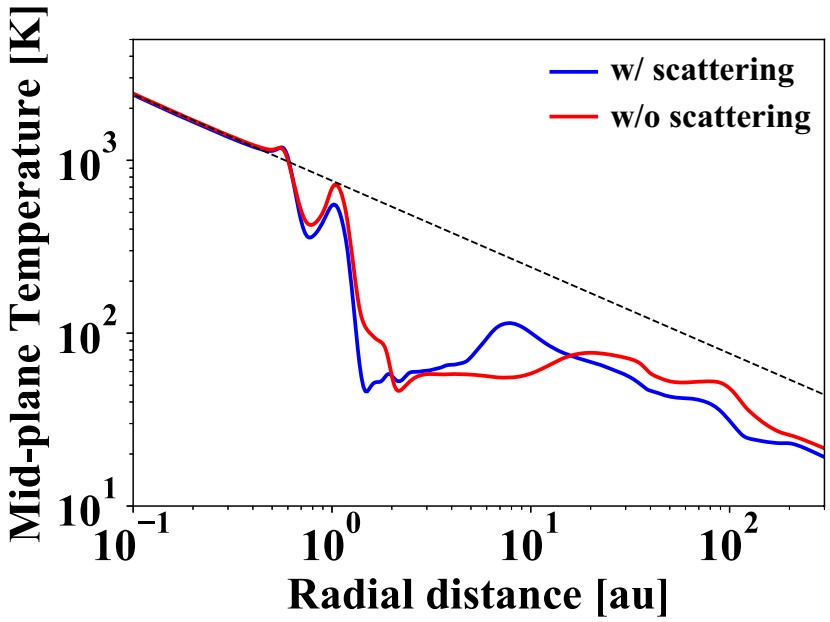

Figure 3.14: Midplane temperature profile for disk model 3 obtained from radiative transfer simulations with (blue) and without (red) scattering. The black dashed line denotes the temperature profile given by Equation (3.19).

switched off. Figure 3.14 shows the results with and without scattering for model 3. We find that the radial width of the shadow is narrower when scattering is switched on but the minimum midplane temperature in the shadowed region is insensitive to scattering.

Figure 3.15(a) shows the two-dimensional distribution of the dust absorption opacity $\kappa_{\rm abs}\rho_{\rm d}$ for the wavelength of 0.3 μm contributed from the smallest dust-size bin. We also plot the effective absorption surface where the effective optical depth $\tau_{\rm eff}$ is equal to unity and the absorption surface where the absorption optical depth $\tau_{\rm abs}$ is equal to unity. The effective absorption optical depth is calculated using the effective absorption coefficient $\kappa_{\rm eff} = \sqrt{\kappa_{\rm abs}(\kappa_{\rm abs} + \kappa_{\rm sca})}$ (Rybicki & Lightman, 1985) where $\kappa_{\rm abs}$ and $\kappa_{\rm sca}$ are respectively the absorption and scattering coefficient. The effective absorption coefficient is useful to express how much distance a photon travels before it is truly absorbed by the medium with taking into account of the effect of scattering. We see that the effective absorption surface is not so different from the absorption surface, which means that scattering does not change the surface structure so much. Figure 3.15(a) also shows that the effective optical depth is almost determined by the smallest grains. The height of absorption surface in the r-z/r plane is constant between 1 and 8 au, In this region, the disk surface does not receive direct irradiation

from the central star. Owing to the shadowing effect, the midplane temperature in the shadowed region significantly decreases as shown in Figure 3.15(b).

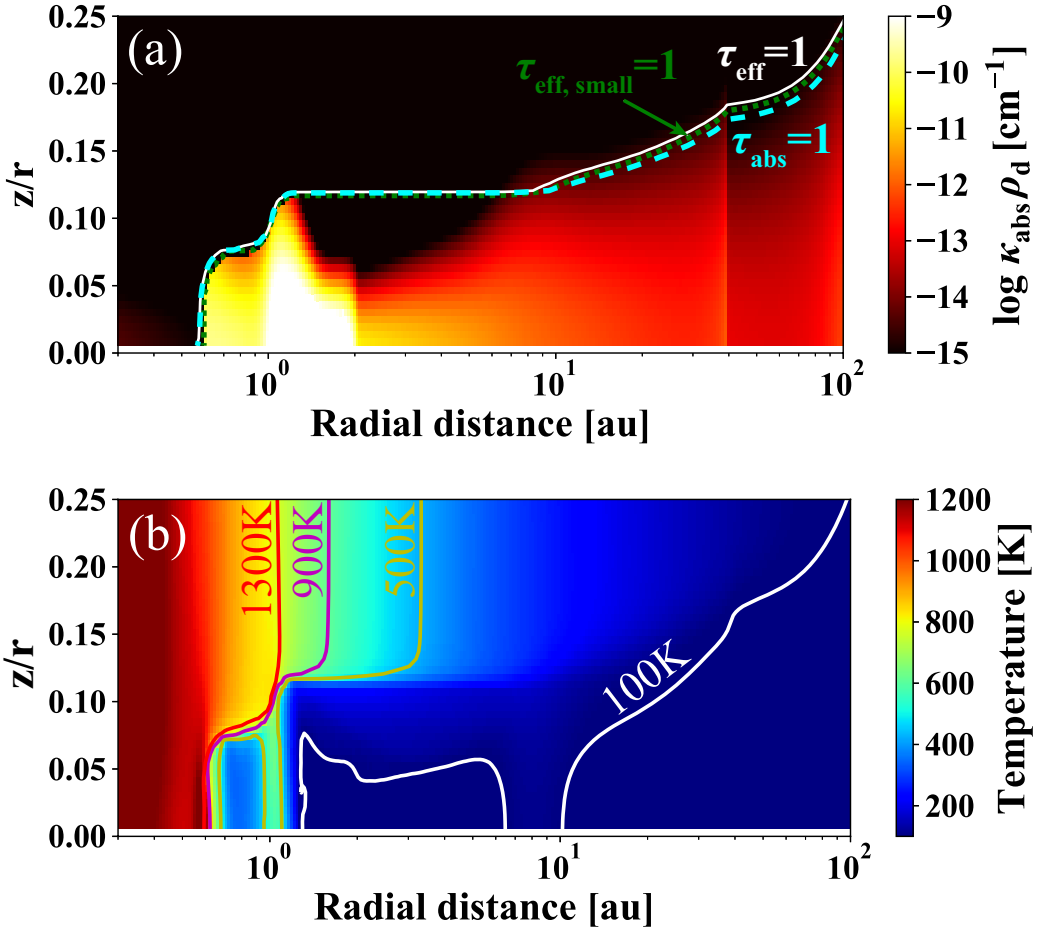

Figure 3.15: Two-dimensional structure of disk model 3. (a) Distribution of the dust absorption opacity $\kappa_{\rm abs}\rho_d$ for the wavelength of 0.3 μm contributed from the smallest dust-size bin (< 0.3 μm). The white solid line denotes the effective absorption surface where the total effective optical depth $\tau_{\rm eff}$ is equal to unity. The cyan dashed line denotes the absorption surface where the absorption optical depth $\tau_{\rm abs}$ is equal to unity. The green dash-dotted line denotes the location where the effective optical depth contributed from the smallest dust-size bin $\tau_{\rm eff,small}$ is equal to unity. (b) Temperature distribution with contour lines of 100K (white), 500K (yellow), 900K (purple) and 1300K (red).

Chapter 4

Inner Solar System Formation via the Dust-Pileup at the Dead-Zone Inner Edge

4.1 Abstract of this Chapter

The dynamical configuration of the inner solar system planets invokes that they formed from a narrow annulus of plantesimals. In this study, we investigate whether the planetesimal formation at the dead-zone inner edge can reproduce the initial planetesimal distribution invoked from the current configuration of the inner solar system planets. We show that if the disk is visously heated, rocky planetesimals form at $\sim$ 0.7–1 au via the dust-pileup at the dead-zone inner edge. The total mass of the planetesimals invoked from the current total mass of the inner solar system planets can also be reproduced, but the turbulence strength in the dead zone needs to be finely tuned since the total planetesimal mass is sensitive to it. Since the disk mass has to be massive for the dead-zone inner edge to be located $\sim$ 0.7–1 au, the disk outer edge needs to be smaller than $\sim$ 80 au to avoid the gravitational instability. Although the subsequent evolution of planetesimals is uncertain, this scenario would potentially account for the inner solar system formation.

4.2 Introduction of this Chapter

Solar system is the most nearest planetary system and has been well studied for past decades (e.g., Hayashi 1981). Nevertheless, the formation of the solar system is still of the most interest subject. The inner solar system has a unique dynamical configuration: large planets (Venus and Earth) sandwiched by two small planets (Mercury and Mars). It is difficult to reproduce the characteristic dynacamical configuration from uniform distribution of planetesimals (e.g., Raymond et al. 2009). Hansen (2009) proposed a scenario that the inner solar system planets have formed from a narrow planetesimal annulus ranges from 0.7 to 1 au with a total mass of $2M_{\oplus}$. Figure 4.1 shows the result of N-body simulations done by Hansen (2009). Hansen

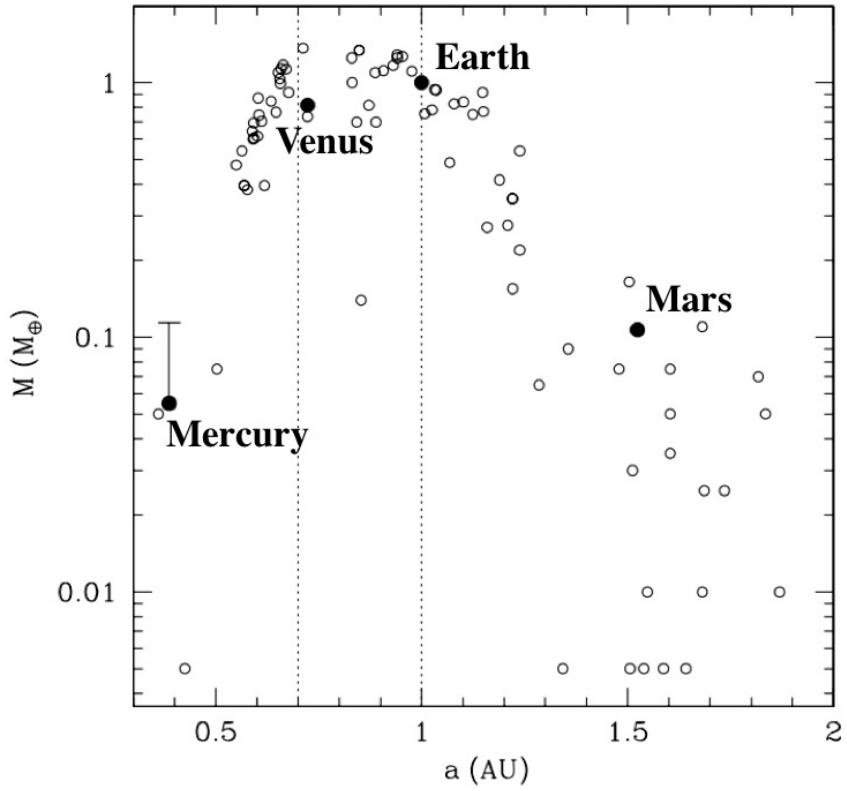

Figure 4.1: Formation of inner solar system planets from a narrow annulus of planetesimals (Figure 1 in Hansen 2009). Open circles represent the distribution of planets obtained from the simulations. The solid points are the four solar system terrestrial planets. The vertical dotted lines indicate the edges of the original annulus of planetesimals.

(2009) showed that planet formation from a narrow planetesimal annulus can explain naturally the configuration of inner solar system planets. The planetesimal formation

via the dust-pileup at the dead-zone inner edge potentially fit to the narrow annulus model because the planetesimals forming from a dust-pileup would be locally distributed. In this section, I investigate whether the planetesimal formation at the dead-zone inner edge can reproduce the initial planetesimal distribution of the inner solar system proposed by Hansen (2009).

4.3 Calculation Method

The calculation method used in this study is basically the same as the method descirbed in section 3.3 except for some respects. In this section, we describe the differences from the method descirbed in section 3.3.

For the central star, we assume a Sun-like star with stellar mass $M_* = M_\odot$, radius $R_* = R_\odot$ and effective temperature $T_* = 5778$ K. For the temperature structure of the disk, we consider the effect of viscous heating in addition to the irradiation heating. If we consider only the irradiation heating, the location of the dead-zone inner edge is around 0.1 au (Ueda et al., 2017) which is much inside the location of the planetesimal annulus proposed by Hansen (2009). However, the mid-plane temperature in the inner region of disks around a Sun-like star can be heated by the viscous heating. The mid-plane temperature of viscously heated disk is given by (e.g., Nakamoto & Nakagawa 1994; Oka et al. 2011)

$$T_{\rm mid,vis} = \left(\frac{3}{2} + \frac{3\tau}{8}\right)^{1/4} \left(\frac{GM_*\dot{M}}{4\pi\sigma_{\rm SB}R^3}\right)^{1/4}, \tag{4.1}$$

where $\tau = \kappa\Sigma_{\rm g}/2$ is the vertical optical depth of the disk at the peak wavelength of the dust thermal emission. Therefore, in this study, the mid-plane temperature T is calculated as

$$T^4 = 2(T_1^4 + T_2^4) + T_{\rm mid,vis}^4 + T_{\rm bg}^4, \tag{4.2}$$

where T_1 and T_2 are the temperature determined by the stellar irradiation (Equations (2.13) and (2.14)) and $T_{\rm bg} = 10$ K is a floor value of the temperature determined by the external heating.

The opacity κ is a function of the amount of dust particles and defined as

$$\kappa = \kappa_{\rm g} + \frac{\Sigma_{\rm d}}{\Sigma_{\rm g}}\kappa_{\rm d}, \tag{4.3}$$

where $\kappa_{\rm g} = 10^{-4}$ cm^2 g^{-1} and $\kappa_{\rm d} = 500$ cm^2 g^{-1} are the gas and dust opacity, respectively. If we adopt the typical value of $\Sigma_{\rm d}/\Sigma_{\rm g} = 0.01$, Equation (4.3) leads to $\kappa \approx 5$ cm^2 g^{-1}.

For the initial condition, α is set to be $\alpha_{\rm dead}$ for the entire region of the disk. The initial surface density is determined as $\Sigma_{\rm g} = \dot{M}/3\pi\nu$ with $\dot{M}$ being a parameter. The disk is assumed to have a exponential cut off radius $r_{\rm c}$ of 80 au.

4.4 Results

4.4.1 Disk evolution

Figure 4.2 shows the time evolution of the dust and gas surface densities and the temperature profile for the disk with $\dot{M} = 10^{-8} M_\odot$ yr^{-1}, $\alpha_{\rm dead} = 1.05 \times 10^{-3}$ and $v_{\rm frag} = 10$ m s^{-1}. In this simulation, the dead-zone inner edge is initially located at ~ 0.5 au. We clearly see that dust particles are trapped around the dead-zone inner edge. The trapped dust particles increase the mid-plane temperature by increasing the vertical optical thickness of the disk. It pushes the dead-zone inner boundary radially outward. However, the dust-pileup cannot keep its high dust-to-gas mass ratio for a long time because dust particles gradually leak out of the dust-pileup due to turbulent diffusion and dust mass flux from the outer region decreases with time.

The temperature profile can be divided into four regimes. In the inner most region (< 0.03 au), the temperature profile follows Equation (4.1) with $\tau \simeq 0$ since the almost all of dust particles evaporate. The region where ~ 0.03–0.3 au has a uniform temperature profile that is equal to the evaporation temperature $T_{\rm ev} = 1350$ K. If T falls below $T_{\rm ev}$, dust particles start to condense, but the condensed dust particles act to push the temperature back up because it increases the vertical optical thickness. Hence, in this region, dust evaporation and condensation regulate the temperature to the evaporation temperature (see also section 2.3.2). In the outer region (0.3–10 au), the temperature profile follows Equation (4.1) with the contribution from the optical thickness since dust particles do not evaporate in this region. In the outermost region (> 10 au), the temperature is determined by the stellar irradiation.

Since our focus is on the inner solar system formation, we set the turbulence strength to be relatively strong ($\alpha_{\rm dead} \sim 10^{-3}$), otherwise too much planetesimals form. We found that if we choose smaller value of $\alpha_{\rm dead}$, dust particles are strongly concentrated on the dead-zone inner edge and eventually the dust surface density shows the oscillatory behavior. This would be caused by the instability induced by the opacity gradient (Klahr & Lin 2005). We discuss the details of the instability in section 4.7.1.

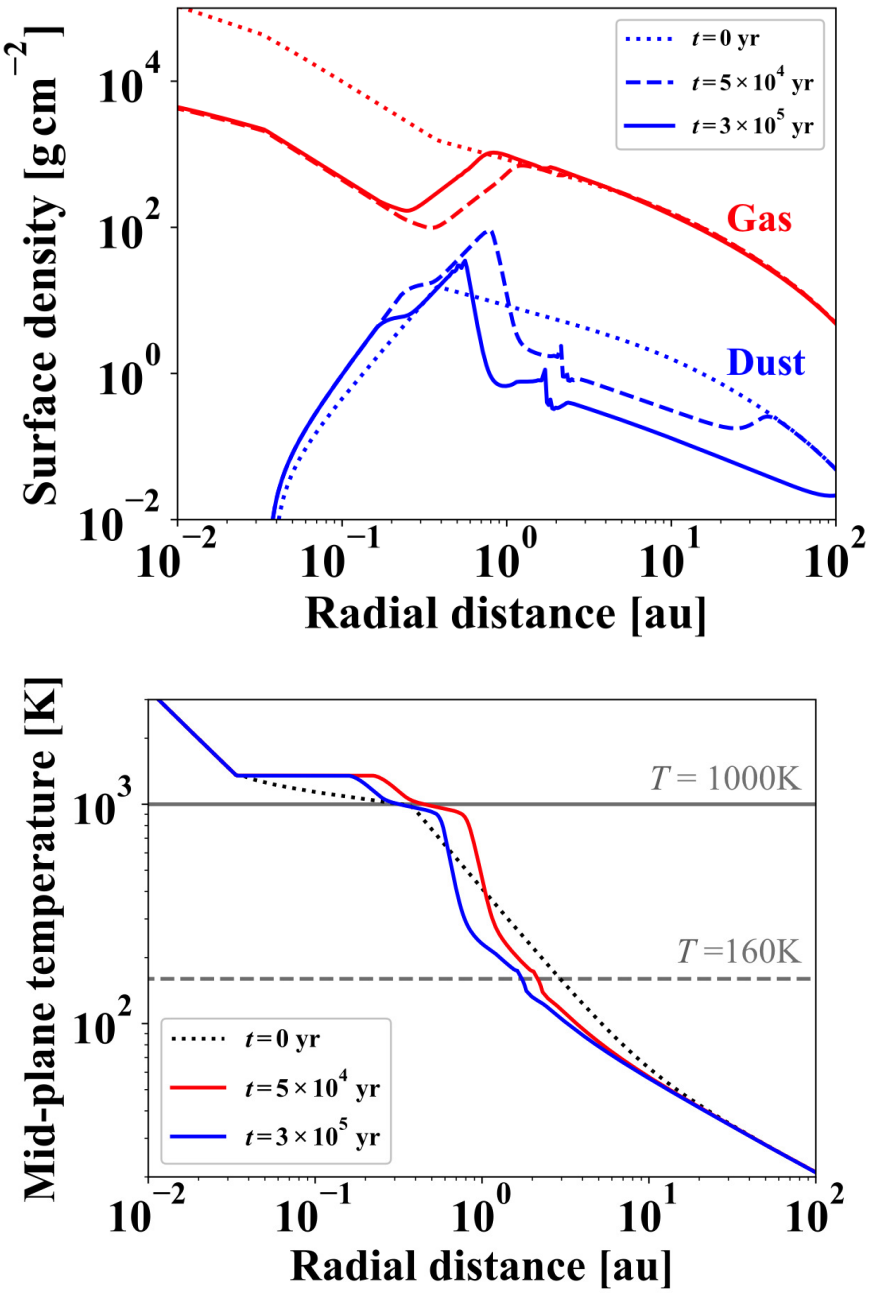

Figure 4.2: *top*: Time evolution of the dust and gas surface densities of the disk with $\dot{M} = 10^{-8} M_\odot$ yr^{-1}, $\alpha_{\rm dead} = 1.05 \times 10^{-3}$ and $v_{\rm frag} = 10$ m s^{-1}. The dotted lines denote the initial distribution. The dashed and solid lines denote the surface densities at $t = 5 \times 10^4$ and 3×10^5 yr, respectively. *bottom*: Time evolution of the temperature profile of the disk around a Sun-like star. The black dotted line denotes the initial temperature profile. The red and blue solid lines denote the temperature profile at $t = 5 \times 10^4$ and 3×10^5 yr, respectively. The gray dashed and solid lines denote $T = 160$ K and 1000 K, respectively.

4.4.2 Planetesimal surface density

Figure 4.3 shows the surface densities of planetesimals forming at the dead-zone inner edge for different disk models. We see that in these simulations, planetesimals

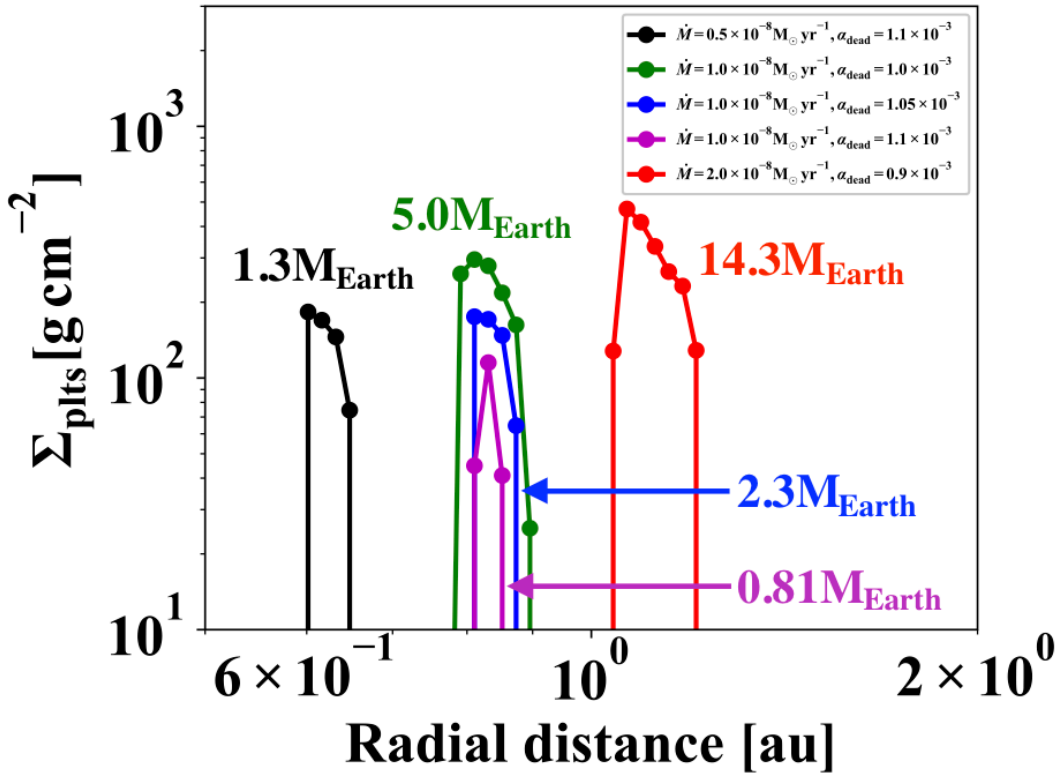

Figure 4.3: Planetesimal surface density profiles for different disk models. *red*: $\dot{M} = 2.0 \times 10^{-8} M_\odot\,\mathrm{yr}^{-1}$ and $\alpha_{\rm dead} = 0.9 \times 10^{-3}$, *magenta*: $\dot{M} = 1.0 \times 10^{-8} M_\odot\,\mathrm{yr}^{-1}$ and $\alpha_{\rm dead} = 1.1 \times 10^{-3}$, *blue*: $\dot{M} = 1.0 \times 10^{-8} M_\odot\,\mathrm{yr}^{-1}$ and $\alpha_{\rm dead} = 1.05 \times 10^{-3}$, *green*: $\dot{M} = 1.0 \times 10^{-8} M_\odot\,\mathrm{yr}^{-1}$ and $\alpha_{\rm dead} = 1.0 \times 10^{-3}$, *black*: $\dot{M} = 0.5 \times 10^{-8} M_\odot\,\mathrm{yr}^{-1}$ and $\alpha_{\rm dead} = 1.1 \times 10^{-3}$. The fragmentation velocity of rocky grains is set to be 10 m s^{-1}.

form at the location where the Venus and Earth currently exist ($\sim$ 0.7–1 au). Because the higher mass accretion rate results in the higher disk temperature, the planetesimal annulus is located more distant from the central star for the disk with higher mass accretion rate. The location where planetesimals form can be estimated from Equation (4.1). If we assume a steady accretion, $\dot{M} = 3\pi\Sigma_{\rm g}\nu$, Equation (4.1) is rewritten as

$$T_{\rm mid,vis} = 437 \left(\frac{r}{\rm au}\right)^{-9/10} \left(\frac{\dot{M}}{10^{-8} M_\odot\ \mathrm{yr}^{-1}}\right)^{2/5} \left(\frac{\kappa}{5\ \mathrm{cm}^2\ \mathrm{g}^{-1}}\right)^{1/5} \left(\frac{\alpha}{10^{-3}}\right)^{-1/5} \mathrm{K}, \qquad (4.4)$$

here we assume $\tau \gg 1$ and the central star is assumed to be the Sun. For the typical values of $\dot{M} = 10^{-8} M_\odot\ \mathrm{yr}^{-1}$, $\kappa = 5\ \mathrm{cm}^2\ \mathrm{g}^{-1}$ and $\alpha = 10^{-3}$, Equation (4.4) leads to

$T_{\rm vis,mid} = T_{\rm MRI} = 1000$ K at $r = 0.4$ au. However, if dust particles concentrate on the dead-zone inner edge, the opacity κ increases and it pushes the dead-zone inner edge outward. As we can see in Figure 4.2, the dust-to-gas mass surface density ratio at the dead-zone inner edge is ~ 20 times higher than the fiducial value of 0.01. If we adopt $\Sigma_{\rm d}/\Sigma_{\rm g} = 0.2$ to Equation (4.3), $\kappa = 100$ cm^2 g^{-1}, leading to $T_{\rm vis,mid} = T_{\rm MRI}$ at $r = 0.8$ au.

We can see from Figure 4.3 that the total mass of planetesimals is sensitive to the turbulence strength as we mentioned in chapter 3. Nevertheless the difference in the value of $\alpha_{\rm dead}$ is only a factor of ~ 0.1, total mass of planetesimals in the disk with $\dot{M} = 10^{-8} M_\odot$ yr^{-1} varies from $0.81 M_\oplus$ to $5.0 M_\oplus$.

4.4.3 Condition for the inner solar system formation

As you can see in Figure 4.3, the location of the birth place of planetesimals and its amount depend on the disk properties such as the gas mass accretion rate and the turbulence strength. Here, we derive the condition for the planetesimal formation which is preferable for the inner solar system. In this study, we define two conditions as the condition for the inner solar system formation.

The first one specifies the location where planetesimals form. In order to form the inner solar system planets, planetesimals should form between 0.7 and 1 au. This condition can be estimated by equating Equation (4.4) to $T_{\rm MRI}$ as

$$0.32 \lesssim \left(\frac{\alpha_{\rm dead}}{10^{-3}}\right)\left(\frac{\dot{M}}{10^{-8}{\rm M}_\odot\ {\rm yr}^{-1}}\right)^{-2}\left(\frac{\kappa}{100\ {\rm cm}^2\ {\rm g}^{-1}}\right)^{-1} \lesssim 1.6. \tag{4.5}$$

The left inequality comes from the condition that the dead-zone inner edge is located within 1 au and the right inequality comes from the condition that the dead-zone inner edge is located outside of 0.7 au.

The second condition specifies the amount of planetesimals. In order to form the inner solar system planets, the total planetesimal mass needs be around $2 M_\oplus$. In chapter 3, we demonstrated that the dust-pileup at the dead-zone inner edge operates when $\alpha_{\rm dead}$ is smaller than the critical value given by Equation (3.25) and the total mass of planetesimals increases as $\alpha_{\rm dead}$ decreases. If $\alpha_{\rm dead}$ is sufficiently smaller than the critical value given by Equation (3.25), too much planetesimals would form, indicating that the value of $\alpha_{\rm dead}$ slightly smaller than the critical value is preferable for the inner solar system formation. Table 4.1 summarizes the parameters and the obtained total planetesimal mass in different disk models. If the $\alpha_{\rm dead}$ is lower than 0.9×10^{-3}, the total mass of planetesimals exceeds $10 M_\oplus$, which might leads to the

sub-Neptune mass planet. In contrast, if the $\alpha_{\rm dead}$ is higher than 1.1×10^{-3}, the total mass of planetesimals is less than $1 M_\oplus$, which is not enough to form terrestrial planets. Our simulations suggest that $\alpha_{\rm dead} \approx 1.0 \times 10^{-3}$, which is 3 times smaller than the critical $\alpha_{\rm dead}$ value given by Equation (3.25), is preferable to form the inner solar system.

Table 4.1: Parameters and results obtained in different disk models

$\dot{M}[10^{-8}{\rm M}_\odot\ {\rm yr}^{-1}]$	$\alpha_{\rm dead}$ $[10^{-3}]$	planetesimal mass $[M_\oplus]$
0.5	0.7	22
	0.8	12
	0.9	7.1
	1.0	3.3
	1.1	1.3
1.0	0.7	39
	0.8	21
	0.9	11
	1.0	5.0
	1.1	0.81
2.0	0.7	60
	0.8	30
	0.9	14
	1.0	3.8
	1.1	0.0

It would be worth noted that if $\alpha_{\rm dead}$ is too small, the disk would be gravitationally unstable. Because the critical value of $\alpha_{\rm dead}$ is proportional to $v_{\rm frag}$, the preferable value of $\alpha_{\rm dead}$ for the inner solar system formation would be smaller as $v_{\rm frag}$ is smaller. However, smaller $\alpha_{\rm dead}$ leads to more massive gas disk. It means that if $v_{\rm frag}$ is too small, the preferable value of $\alpha_{\rm dead}$ is too small to keep the gas disk being gravitationally stable. Let us roughly estimate the disk mass to examine the stability of the disk. If we assume the temperature profile given by Equation (4.4) and a steady accretion disk, the surface density profile is given as

$$\Sigma_{\rm g} = 832 \left(\frac{r}{\rm au}\right)^{-3/5} \left(\frac{\dot{M}}{10^{-8}{\rm M}_\odot\ {\rm yr}^{-1}}\right)^{3/5} \left(\frac{\alpha}{10^{-3}}\right)^{-4/5} \left(\frac{\kappa}{5\ {\rm cm}^2\ {\rm g}^{-1}}\right)^{-1/5} {\rm g\ cm}^{-2}. \quad (4.6)$$

Therefore, the total mass of the disk within the region ranging from $r_{\rm in}$ to $r_{\rm c}$ is

$$M_{\rm disk} = \int_{r_{\rm in}}^{r_{\rm c}} 2\pi \Sigma_{\rm g} r {\rm d}r \quad (4.7)$$

$$= 0.19 M_\odot \left(\frac{r_{\rm c}}{80\ {\rm au}}\right)^{7/5} \left(\frac{\dot{M}}{10^{-8}{\rm M}_\odot\ {\rm yr}^{-1}}\right)^{3/5} \left(\frac{\alpha}{10^{-3}}\right)^{-4/5} \left(\frac{\kappa}{5\ {\rm cm}^2\ {\rm g}^{-1}}\right)^{-1/5}, \quad (4.8)$$

here we assume $r_{\rm in} \ll r_{\rm c}$. Because the condition for the gravitationally stable disk is $M_{\rm disk}/M_* \lesssim 0.1$ (Toomre, 1964), using Equation (4.8), the condition can be written as

$$\alpha_{\rm dead} > 2 \times 10^{-3} f \left(\frac{r_{\rm c}}{80\ {\rm au}}\right)^{7/4} \left(\frac{\dot{M}}{10^{-8} {\rm M}_\odot\ {\rm yr}^{-1}}\right)^{3/4} \left(\frac{\kappa}{5\ {\rm cm}^2\ {\rm g}^{-1}}\right)^{-1/4}, \tag{4.9}$$

where f is a modification factor. Since, in the derivation of Equation (4.6), we assume a viscous heating as a heat source even in the outer region where the temperature basically determined by the stellar irradiation, Equation (4.6) overestimates the disk mass. If we carefully consider such detailed disk structure, the disk mass is $0.1 M_\odot$ when $r_{\rm c} = 80$ au, $\dot{M} = 10^{-8} M_\odot$ yr^{-1}, $\alpha_{\rm dead} = 10^{-3}$ and $\kappa = 5$ cm^2 g^{-1}, which is marginally stable, meaning that Equation (4.8) overestimates the disk mass by a factor of ~ 2. In order to correct the error, we set $f = 0.5$ in Figure (4.4), . Note that even if the disk is gravitationally unstable, the gravitational instability occurs only in the outer region and the inner region where we focus on is still stable.

Figure 4.4 summarizes the obtained planetesimal mass in different disk models and the condition for the inner solar system formation via the dust-pileup at the dead-zone inner edge. From the point of view of the location of the planetesimal formation, the gray-colored area in Figure 4.4 is preferable for the inner solar system formation. From the point of view of the total mass of planetesimals, the blue-colored area in Figure 4.4 is preferable for the inner solar system formation. Therefore, the parameter space where the gray-colored region overlaps the blue-colored region in Figure 4.4 is a sweet spot for the inner solar system formation.

4.5 Discussion

4.5.1 Dependence on Planetesimal Formation Model

In our model, we assume that planetesimals form via the streaming instability when the mid-plane dust-to-gas mass ratio is higher than unity with the formation efficiency of $\zeta = 10^{-4}$ (Equation (3.22)). The efficiency of planetesimal formation via the streaming instability is still unclear and have been recently investigated by the numerical simulations (e.g., Simon et al. 2016,Simon et al. 2017). Simon et al. (2016) performed simulations of the streaming instability including the self-gravity of the dust particles and showed that planetesimals form via the streaming instability with a timescale corresponding to $\eta \sim 10^{-2}$ for the particles of St $= 0.3$. Since the radial drift velocity of dust particles is proportional to the Stokes number and hence

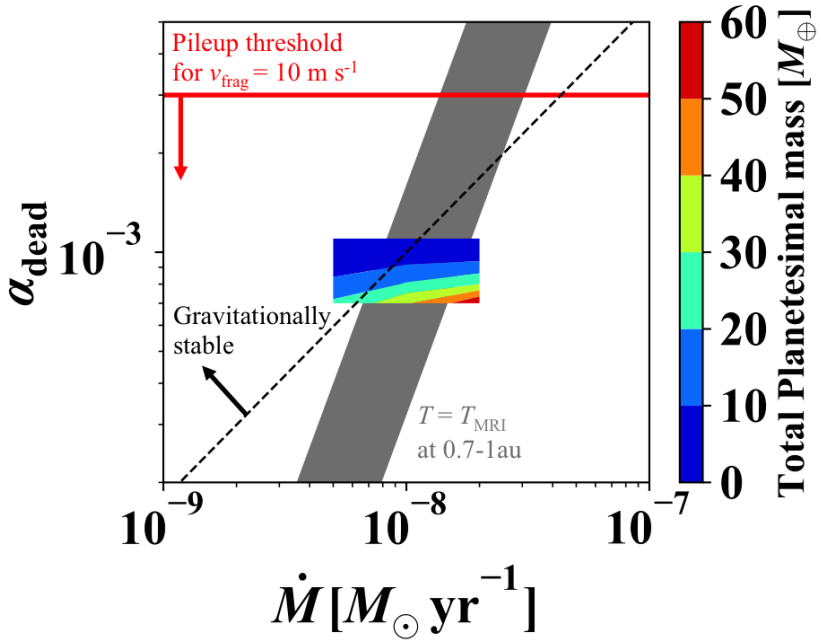

Figure 4.4: Condition for the inner solar system formation. The color map shows the total planetesimal mass obtained in different disk models The red solid lines denote the condition for the dust-pileup to operate (Equation (3.25)). The gray-colored area shows the condition for the dead-zone inner edge to be located between 0.7 and 1 au (Equation (4.5) with assuming $\kappa = 100$ cm^2 g^{-1}). The black dashed line denote the condition for the disk to be gravitationally stable (Equation (4.9) with $\kappa = 5$ cm^2 g^{-1} and $f = 0.5$).

the size of dust particles, the formation of planetesimals via the streaming instability takes longer time for smaller particles. Yang et al. (2017) investigated the streaming instability for much smaller particles and found that the strong dust concentration via the streaming instability occurs with the timescale of $\sim$ 400–1000 $T_{\rm K}$ and $\sim$ 600–2000 $T_{\rm K}$ for particles with St $= 10^{-2}$ and 10^{-3}, respectively. Although Yang et al. (2017) did not investigate the planetesimal formation through the subsequent evolution of the dust concentration because their simulations did not treat the self-gravity of the particles, their results imply that the planetesimal formation efficiency ζ is smaller than $\sim 10^{-3}$ for dust particles with the Stokes number smaller than 10^{-2}.

In order to investigate the uncertainty in the total mass of planetesimals originating from the uncertainty in the planetesimal formation efficiency η, we additionally perform the simulations of planetesimal formation with the same setting with the simulation in Figure 4.2 other than the value of ζ. We find that the total mass of

planetesimals is $0.72M_\oplus$ and $4.5M_\oplus$ for $\zeta = 10^{-5}$ and 10^{-3}, while $\zeta = 10^{-4}$ results in the total mass of planetesimals of $3.1M_\oplus$. Therefore, we can say that, although an order of difference in the planetesimal formation efficiency makes the difference in the total mass with a factor of $\sim$ 1.5–4, the condition for the terrestrial planet formation is not so sensitive to the value of the planetesimal formation efficiency. The dependence of total planeteismal mass on ζ is determined by the balance between the supply of drifting dust particles and taking the dust particles away via the planetesimal formation (e.g., Drążkowska et al. 2016). If the supply of the dust particles is enough large, the dust surface density is determined by the radial drift and hence the total mass of planetesimals increases with increasing ζ. However, if the supply of the dust particles is small, the dust surface density decreases with increasing ζ hence the total mass of planetesimals does not strongly depend on ζ.

4.5.2 Effect of uncertainty in the opacity on the planetesimal formation

In this study, we assume the dust opacity of 500 cm^2 g^{-1}. However, the dust opacity has large uncertainty and basically changes with the dust radius (e.g., Pollack et al. 1994; Weingartner & Draine 2001).

Birnstiel et al. (2018) calculated the dust opacities with different dust-size distributions and different optical properties and showed that the absorption opacity is $\sim$ 100–1000 μm at the wavelength of 3 μm which corresponds to the peak wavelength of the black-body radiation with the temperature of 1000 K when the maximum dust radius is 1 mm. Because the maximum dust radius at the dead-zone inner edge in our simulations is an order of 1 cm, the absorption opacity would be $\sim$ 10–100 μm, which is $\sim$ 5–50 times smaller than that we used. The smaller opacity would result into the lower temperature which pushes the dead-zone inner edge inward. As we can see from Equation (4.5), the location of the dead-zone inner edge is a function of $\dot{M}^2\kappa$. Therefore, if κ is $\sim$ 5–50 times smaller, $\dot{M}$ needs to be $\sim$ 2.2–7 times higher to put the dead-zone inner edge to the same radial location.

4.5.3 Implication from the cosmochemical constraints

Our results suggest that the building blocks of the inner solar system potentially formed via the dust-pileup at the dead-zone inner edge. In this section, we discuss the possibility that the scenario can account for the cosmochemical constraints.

The Mars is the only planet, except for the Earth, for which we have direct samples. The Hf-W system tell us about the formation timescale of the planets because Hf and W behave differently when the metal segregation occurs (e.g., Nimmo & Kleine 2007). ^{182}Hf which is a lithophile element decays to stable ^{182}W which is a siderophile element with a half-year of 9 Myr. Hence, if the core formation occurs earlier, the mantle has higher ^{182}W/^{183}W ratio. The isotope analysis of the bulk Earth and Mars meteorite samples showed that the Earth and Mars should form within 30 Myr and 1–10 Myr, respectively (e.g, Nimmo & Kleine 2007; Kleine et al. 2009). Hansen (2009) showed that these timescales are well explained by the formation via the narrow annulus of planetesimals.

Although the observational value of the Hf-W system can be explained by the narrow annulus model, there are isotopic systems that suggest that the building blocks of the Earth and Mars should be different. For example, the bulk of Mars is clearly enriched in ^{17}O with respect to the bulf of Earth and Moon (e.g., Franchi et al. 1999; Wittmann et al. 2015). Other isotopic systems that trace nucleosynthetic anomalies, such as titanium, chromium, and nickel, also show clear differences in the Earth and Mars (Brasser et al. 2017). To reproduce the isotopic differences with the same building materials is difficult because there is no mass-dependent process which can account for these differences (Qin & Carlson 2016).

In order to explain the isotopic differences in the Earth and Mars, they should form from different building blocks. However, if the planets formed from the planetesimal annulus formed via the dust-pileup at the dead-zone inner edge, their isotopic composition would be similar to each other. One possible solution of this problem is another source of building blocks. Recent numerical simulations have suggested that the snow line is a preferential site for the icy planetesimal formation (Schoonenberg & Ormel 2017; Drążkowska & Alibert 2017). Just behind the snow line, the icy grains can potentially grow beyond the drift barrier through the recondensation of water vapor (Ros & Johansen 2013; Wang 2015). In our simulation, the snow line is located at 2–3 au which is similar to the current orbits of main-belt asteroids. If planetesimals form around the snow line, some of them would be scattered into the inner region and would make the compositional difference in the inner planets. This possibility should be investigated in near future.

4.5.4 Migration of formed planetesimals

In this section, we estimate the migration timescale of planetesimals forming at the dead-zone inner edge. Even if the planetesimals form at the location where Hansen

(2009) proposed, the planetesimals might radially migrate due to the gravitational interaction with the gas disk. The migration timescale due to the gravitational interaction with the gas disk is given by Tanaka et al. (2002)

$$\tau_{\rm mig,I} = \frac{1}{2.7 + 1.1p}\left(\frac{M_{\rm p}}{M_*}\right)^{-1}\left(\frac{\Sigma_{\rm g} r^2}{M_*}\right)^{-1}\left(\frac{c_{\rm s}}{v_{\rm K}}\right)^2 \Omega_{\rm K}^{-1}, \tag{4.10}$$

where p is an absolute value of the power-law index of the radial surface density profile. If we assume $r = 1$ au and $p = 1.0$,

$$\tau_{\rm mig,I} \simeq 1.9 \times 10^8 \left(\frac{\Sigma_{\rm g,1\ au}}{100\ {\rm g\ cm^{-2}}}\right)^{-1}\left(\frac{T}{1000\ {\rm K}}\right)\left(\frac{r_{\rm p}}{1000\ {\rm km}}\right)^{-3}\ {\rm yr}. \tag{4.11}$$

Equation (4.11) indicates that the planetesimals does not suffer from the significant inward migration if their radii are less than $\sim$ 1000 km. Although the typical size of the planetesimals formed by the streaming instability is still under discussion and depends on the local structure of the disk, some numerical simulations suggest that the size of planetesimals would be an order of $\sim$ 10–100 km in radius (e.g., Johansen et al. 2012, Abod et al. 2018).

4.6 Summary

We investigated whether the planetesimal formation at the dead-zone inner edge can reproduce the initial planetesimal distribution for the inner solar system formation proposed by Hansen (2009). We showed that if the disk is viscously heated, the dust-pileup locally enhances the vertical optical depth at the dead-zone inner edge, which pushes the dead-zone inner edge outward. Helped by the local temperature enhancement, rocky planetesimals can form at $\sim$ 0.7–1 au even the gas accretion rate is $\sim 10^{-8} M_\odot$ yr^{-1}. The total mass of planetesimals which is inferred from the current mass of inner solar system planets can also be reproduced, but the value of $\alpha_{\rm dead}$ needs to be finely tuned since the total planetesimal mass is sensitive to $\alpha_{\rm dead}$. Our simulations suggest that for the critical fragmentation velocity of 10 m s^{-1}, $\alpha_{\rm dead} \sim 0.9$–$1.1 \times 10^{-3}$, which is$\sim$ 3 times smaller than the critical value for dust-trapping to operate given by Equation (3.25), is preferable to reproduce the total planetesimal mass for the inner solar system planets. Even the dead-zone inner edge is located at $\sim$ 0.7–1 au, the location of the snow-line still keep close to the central star; $\sim$ 2–3 au which is similar to the orbits of the main-belt asteroids. The formation of planetesimals at the snow-line might contribute to the compositional difference between the Earth and Mars. Although the subsequent evolution of planetesimals has

large uncertainty, this scenario would potentially account for the inner solar system formation.

4.7 Appendix

4.7.1 Instability induced by the opacity gradient

In this section, we analyze the stability of the dust disk embed in the viscously heated gas disk. In order to investigate the stability of the dust disk in the viscously heated protoplanetary disk, let us formulate the one dimensional continuity equation of dust disk including the effect of viscous heating. One dimensional continuity equation of dust is

$$\frac{\partial \Sigma_{\rm d}}{\partial t} = -\frac{1}{r}\frac{\partial (r\Sigma_{\rm d} v_{\rm d})}{\partial r}. \tag{4.12}$$

The radial velocity of dust particles $v_{\rm d}$ is written as

$$v_{\rm d} = -\frac{2{\rm St}}{1+{\rm St}^2}\eta v_{\rm K}. \tag{4.13}$$

The variable η represents the deviation in the rotational velocity of the gas from the Keplerian velocity and is written as

$$\eta = -\frac{1}{2}\left(\frac{c_{\rm s}}{v_{\rm K}}\right)^2 \frac{\partial \ln p}{\partial \ln r}, \tag{4.14}$$

where $c_{\rm s}$ and p are the sound speed and the pressure of the gas written as

$$c_{\rm s}^2 = \frac{kT}{m} \tag{4.15}$$

and

$$p = \rho_{\rm g} c_{\rm s}^2 \tag{4.16}$$

respectively, where k is the Boltzmann constant, m is the mean molecular mass, T is the mid-plane temperature and $\rho_{\rm g}$ is the gas density at the mid-plane. Using the relation $\rho_{\rm g} = \Sigma_{\rm g}/\sqrt{\pi} h_{\rm g}$ where $h_{\rm g} = c_{\rm s}/\Omega_{\rm K}$ is the gas scale height, Equation (4.16) can be rewritten as

$$p = \frac{\Sigma_{\rm g} c_{\rm s} \Omega_{\rm K}}{\sqrt{\pi}}. \tag{4.17}$$

If we consider the disk heated by viscous accretion, the mid-plane temperature is written as

$$T^4 \approx \frac{3}{8}\kappa_{\rm d}\Sigma_{\rm d}\frac{9\nu\Sigma_{\rm g}\Omega_{\rm K}^2}{8\sigma}, \tag{4.18}$$

where κ_d is the Rosseland-mean opacity of dust particles, ν is the viscosity coefficient and σ is the Stefan-Boltzmann constant. In Equation (4.18), we assume that the vertical optical depth $\tau = \kappa_d \Sigma_d / 2$ is sufficiently larger than unity and ignore the effect of the gas opacity for simplicity. Using Equation (4.18), Equation (4.15) is rewritten as

$$c_s^2 = \frac{k}{m} \left(\frac{3}{8} \kappa_d \Sigma_d \right)^{1/4} \left(\frac{9 \nu \Sigma_g \Omega_K^2}{8\sigma} \right)^{1/4}. \tag{4.19}$$

Introducing the alpha-viscosity model $\nu = \alpha c_s^2 / \Omega_K$, Equation (4.19) is rewritten as

$$c_s = \left(\frac{k}{m} \right)^{2/3} \left(\frac{3}{8} \kappa_d \Sigma_d \right)^{1/6} \left(\frac{9 \alpha \Sigma_g \Omega_K}{8\sigma} \right)^{1/6}. \tag{4.20}$$

Let us introduce a typical consntant-value of Σ_d, $\Sigma_{d,0}$, and the corresponding sound speed $c_{s,0}$ and gas pressure p_0. Using these values and Equation (4.20), Equation (4.17) can be rewritten as

$$p = p_0 \left(\frac{\Sigma_d}{\Sigma_{d,0}} \right)^{1/6}. \tag{4.21}$$

Substituting Equation (4.21) into Equation (3.6), we obtain

$$\eta = -\frac{1}{2} \left(\frac{c_s}{v_K} \right)^2 \left(\frac{\partial \ln p_0}{\partial \ln r} + \frac{1}{6} \frac{\partial \ln \Sigma_d}{\partial \ln r} \right). \tag{4.22}$$

Combining Equations (4.12), (4.13) and (4.22), we obtain the continuity equation for dust particle in viscously heated disks as

$$\frac{\partial \Sigma_d}{\partial t} = -\frac{1}{r} \frac{\partial}{\partial r} \left\{ \frac{r \Sigma_d v_K \mathrm{St}}{1 + \mathrm{St}^2} \left(\frac{c_s}{v_K} \right)^2 \left(\frac{\partial \ln p_0}{\partial \ln r} + \frac{1}{6} \frac{\partial \ln \Sigma_d}{\partial \ln r} \right) \right\}.$$

The last term on the left side of Equation (4.23) is the diffusion term with the negative coefficient. Therefore, if the diffusion term dominates over the first term on the left side, which means that the radial gradient of the dust surface density is much steeper than that of the gas pressure, a bump in the dust surface density will grow and be sharpened with time leading to be unstable. If we assume $\Sigma_g \propto r^{-1}$ and $T \propto r^{-3/4}$, $\partial \ln p_0 / \partial \ln r = -23/8$. Therefore, this instability needs very steep surface density gradient which might be originated from dust concentration caused by the dust-trapping at the pressure maximum or dust pileup at the water snow line.

Figure 4.5 shows the schematic of the instability induced by the opacity gradient. When dust particles drift inward and concentrate at the local maximum of the gas

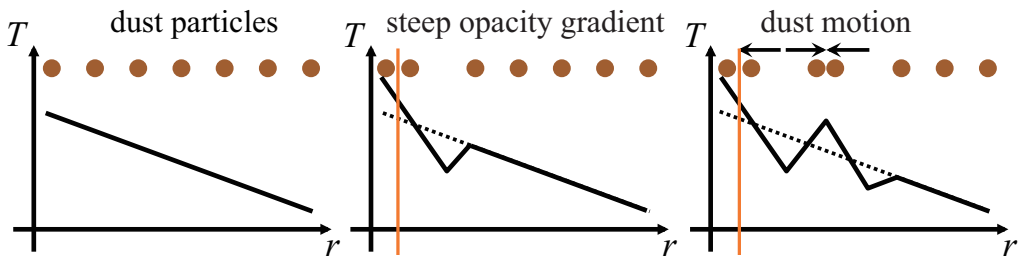

1. Uniform dust distribution (initial)
2. Steep opacity gradient leads to steep temperature gradient
3. Steep temperature gradient enhances the radial dust segregation, resulting in the radial dust clumping

Figure 4.5: Schematic of the instability induced by the opacity gradient.

pressure, the temperature of that location increases because the dust concentration enhances the vertical optical depth. This increase in temperature causes a large pressure gradient leading to fast radial drift of dust particles, resulting in the deficit in dust amount just behind the dust concentration. The deficit in dust amount causes decrease in temperature leading to the next pressure maximum just behind it.

Chapter 5

Summary and Future Prospect

In this thesis, we investigated the rocky planetesimal formation at the dead-zone inner edge and its impact on the disk structure by performing dust growth simulations and radiative transfer simulations.

Since the dead-zone inner edge is located at the radial location where the temperature reaches 1000 K, to understand the temperature structure of the inner region of protoplanetary disks is important to discuss the planetesimal formation at there. In chapter 2, we analytically investigated the temperature structure of the inner region of passively heated protoplanetary disks based on the results from the recent radiation hydrodynamical simulations. The inner part of a disk can be divided into four regions: a dust-free region with a gas temperature in the optically thin limit, an optically thin dust halo, an optically thick condensation front, and the classical, optically thick region, in order from the innermost to the outermost. We derived the analytic expressions successfully describing these characteristic structures obtained from the numerical simulations. Using the analytic formulas, we found that the radius of the dead zone inner edge is $\sim$ 2-3 times larger than that expected from the temperature profile of the classical optically thick disk model.

In chapter 3, as a next step, we performed simulations of the dust and gas disk evolution around a Herbig Ae star to investigate the planetesimal formation at the dead-zone inner edge. We showed that the total mass of planetesimals is sensitive to the turbulence strength in the dead zone because of the combined effect of turbulence-induced particle fragmentation and turbulent diffusion. For a typical critical fragmentation velocity of silicate dust particles of 1 m s^{-1}, the stress to pressure ratio in the dead zone needs to be lower than 3×10^{-4} for dust trapping to operate.

The obtained dust distribution was postprocessed using the radiative transfer code RADMC-3D to investigate the effect of a shadow casted by the dust-pileup. We found that a dust pileup at the dead-zone inner edge, if present, casts a shadow extending

out to $\sim$ 10 au. In the shadowed region the temperature significantly drops, which in some cases yields even multiple water snow lines. These unique features in the inner region of disks would be probed by the future observations. In Figure 5.1,

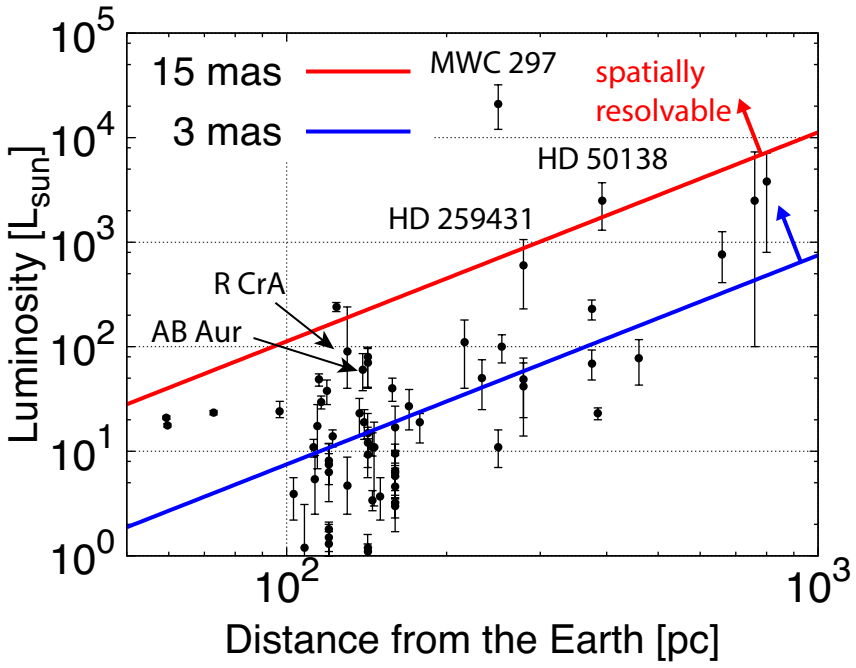

Figure 5.1: Luminosity of stars having a disk as a function of the distance from the Earth. The Stellar parameters are taken from Meeus et al. (2012) and Menu et al. (2015). The blue and red solid lines respectively denote the condition for the spatial resolution of telescopes having the angular resolution of 3 and 15 mas to be comparable to the radius of the dead-zone inner edge estimated by Equation (2.17).

we show the lusminosity of stars having a disk as a function of the distance from the Earth. We also plot the condition for the spatial resolution of telescopes having the angular resolution of 3 and 15 mas to be comparable to the radius of the dead-zone inner edge estimated by Equation (2.17) with $\Gamma = 3, \kappa_{\rm d}(T_*)/\kappa_{\rm d}(T_{\rm B}) = 3$ and $T_{\rm B} = 1470$ K. If the star is located at above the line in the luminosity-distance plane, the dead-zone inner edge is potentially spatially resolvable. Since future observations at (mid-)infrared wavelength using such as VLTI/MATISSE, E-ELT and TMT will accomplish the angular resolution of $\sim$ 3, $\sim$ 5, $\sim$ 15 mas, respectively, these telescopes and interferometer will allow us to directly compare our models with the observations.

In chapter 3, we also found that even without a dust pileup at the dead-zone inner edge, the disk surface can become thermally unstable, and the excited waves can nat-

urally produce shadows and ring-like structures in observed images. This mechanism might account for the ring-like structures seen in the scattered-light images of some disks, such as the TW Hya disk.

The effect of these shadows on the dust growth should be investigated in detail since the temperature structure determines whether dust particles grow larger, evaporate, drift radially or fragment into small grains. If icy dust particles recondense in the shaded region, the particles can grow larger and settle down to the disk midplane, which would enhance the shadowing effect by lowering the local disk surface. At the outer edge of the shadowed region, the radial temperature profile has a positive gradient which potentially halts the rapid radial drift of dust particles. As we showed in chapter 3, thermal waves are excited at $\sim$ 1–100 au. Therefore, the thermal waves could potentially be both the origin of the observed disk structures and also the mechanism that facilitates planetesimal formation in the outer part of disks where the gaps are found in observations.

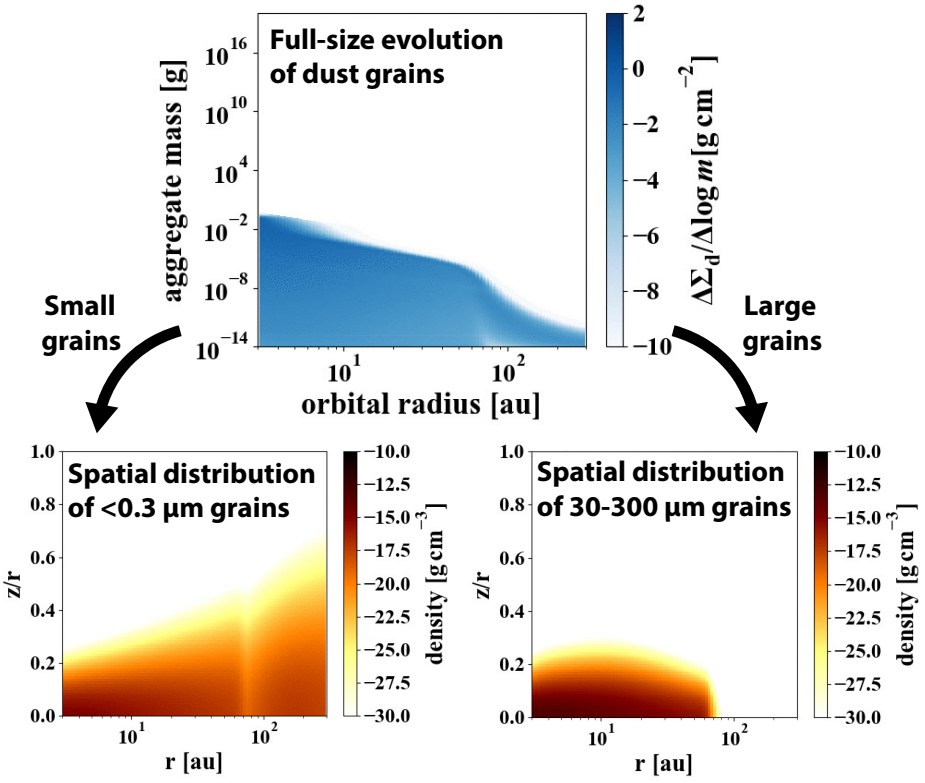

Figure 5.2: Schematic of the dust-growth simulation code we are developing. Thermal structure is simultaneously calculated based on the 2D dust distribution obtained from the dust-growth simulation.

In order to investigate this effect, it is essential to simultaneously calculates dust evolution and thermal structure of the gas disk. Now we are developing the code which simultaneously calculate the evolution of the dust-size distribution and the two-dimensional radiative transfer (Figure 5.2).

Finally, in chapter 4, by applying the simulation code developed in chapter 3, we investigated whether rocky planetesimal formation at the dead-zone inner edge can account for the formation of inner solar system planets. We showed that if the disk is viscously heated, rocky planetesimals form at ~ 0.7–1 au via the dust-pileup at the dead-zone inner edge. In addition, we also showed that the total mass of planetesimals invoked from the total mass of inner solar system planets can also be reproduced. However, the turbulence strength in the dead-zone needs to be finely tuned because the total mass of planetesimals is quite sensitive to it as shown in chapter 3. Since the disk needs to be massive for the dead-zone inner edge to be located at $\sim$ 0.7–1 au, the disk needs to have a outer edge of $\lesssim 80$ au to be gravitationally stable.

Although this hypothesis potentially account for the inner solar system formation, the subsequent evolution of planetesimals has large uncertainty. We showed that if the planetesimals have radii smaller than ~ 1000 km, they does not suffer from the significant inward migration. However, the planetesimals collide each other and grow into larger one, which might lead to the inward migration of the planetesimals. At the same time, the planetesimals would be diffused by the gravitational scattering. By the combined effect of these processes, the resultant planetary system might be different from the solar system. In order to verify the hypothesis we proposed, the subsequent evolution of formed planetesimals will be investigated in near future.

As we demonstrated in chapter 3, the total mass of planeteimals formed at the dead-zone inner edge is sensitive to the turbulence strength in the dead zone; weaker turbulence leads to larger amount of planetesimals. In addition to that, as we showed in chapter 4, if the disk is viscously heated, the gas mass accretion rate controls the radial location of the dead-zone inner edge; higher mass accretion rate leads to much outer dead-zone inner edge. It means that stronger turbulence leads to much outer dead-zone inner edge for a given disk mass. These facts invoke that the planetesimal formation at the dead-zone inner edge potentially account for both close-in super-earth systems and the solar system; close-in super-earth system (massive planets with small orbital radii) forms in a disk with weak turbulence, while the solar system (small planets with large orbital radii) forms in a disk with strong turbulence. This possibility will be also investigated in future.

Acknowledgements

Firstly, I would like to thank my supervisor, Shigeru Ida, for his support during my Ph.D. His continuous support always help me to move forward my studies.

I especially would like to thank Satoshi Okuzumi. Most of the works in this thesis was done under the supervision of him. He gave me plenty of useful advices not only on my studies but also on how to understand the physics in the planet formation, how to give a good presentation, how to write a paper, and much more. He did spend a lot of time discussing ideas with me and opening up new opportunities for me.

I am also thankful to Mario Flock for his support and hosting me at the MPIA, Heidelberg. He always pushed me to a bit further, which significantly improved my work. Thanks also go to Heide Seifert, Gesa H.-M. Bertrang, Lizxandra Flores, Marcelo Barraza, Toshiki Saito and Masafusa Onoue for taking care of me in Heidelberg. I really enjoyed my life in Heidelberg thanks to their supports. There are many more other people in Heidelberg than I can acknowledge here.

I also would like to thank Hiroshi Kobayashi and Taku Takeuchi. They always encouraged me in my studies. I could not have written my first paper without their encouragements.

Many thanks go to all the members of Planet group at the Department of Earth and Planetary Sciences, Tokyo Institute of Technology. I especially like to thank Yuhito Shibaike and Shoji Mori. I could not have come this far without them. I really appreciate them.

Finally, I would like to thank my parents for their support and for making me who I am.

Bibliography

Abod, C. P., Simon, J. B., Li, R., et al. 2018, ArXiv e-prints, arXiv:1810.10018

Adachi, I., Hayashi, C., & Nakazawa, K. 1976, Progress of Theoretical Physics, 56, 1756

Akiyama, E., Muto, T., Kusakabe, N., et al. 2015, ApJL, 802, L17

ALMA Partnership, Brogan, C. L., Pérez, L. M., et al. 2015, ApJ, 808, L3

Andrews, S. M., Wilner, D. J., Zhu, Z., et al. 2016, ApJ, 820, L40

Arakawa, S., & Nakamoto, T. 2016, ApJ, 832, L19

Armitage, P. J. 2011, Annual Review of Astronomy and Astrophysics, 49, 195

Avenhaus, H., Quanz, S. P., Garufi, A., et al. 2018, ApJ, 863, 44

Bae, J., Pinilla, P., & Birnstiel, T. 2018, ApJ, 864, L26

Balbus, S. A., & Hawley, J. F. 1998, Reviews of Modern Physics, 70, 1

Banzatti, A., Pinilla, P., Ricci, L., et al. 2015, ApJ, 815, L15

Barge, P., & Sommeria, J. 1995, A&A, 295, L1

Bertrang, G. H.-M., Avenhaus, H., Casassus, S., et al. 2018, MNRAS, 474, 5105

Birnstiel, T., Dullemond, C. P., & Brauer, F. 2010, A&A, 513, A79

Birnstiel, T., Dullemond, C. P., & Pinilla, P. 2013, A&A, 550, L8

Birnstiel, T., Dullemond, C. P., Zhu, Z., et al. 2018, ApJ, 869, L45

Blum, J., & Wurm, G. 2000, Icarus, 143, 138

Brandl, B. R., Feldt, M., Glasse, A., et al. 2014, in Proc. SPIE, Vol. 9147, Ground-based and Airborne Instrumentation for Astronomy V, 914721

Brasser, R., Mojzsis, S. J., Matsumura, S., & Ida, S. 2017, Earth and Planetary Science Letters, 468, 85

Brauer, F., Henning, T., & Dullemond, C. P. 2008, A&A, 487, L1

Carrera, D., Johansen, A., & Davies, M. B. 2015, A&A, 579, A43

Chatterjee, S., & Tan, J. C. 2014, ApJ, 780, 53

Chiang, E. I., & Goldreich, P. 1997, ApJ, 490, 368

Chokshi, A., Tielens, A. G. G. M., & Hollenbach, D. 1993, ApJ, 407, 806

Coleman, G. A. L., & Nelson, R. P. 2016, MNRAS, 457, 2480

Coradini, A., Magni, G., & Federico, C. 1981, A&A, 98, 173

D'Alessio, P., Cantó, J., Hartmann, L., Calvet, N., & Lizano, S. 1999, ApJ, 511, 896

Desch, S. J., & Turner, N. J. 2015, ApJ, 811, 156

Dorschner, J., Begemann, B., Henning, T., Jaeger, C., & Mutschke, H. 1995, A&A, 300, 503

Drążkowska, J., & Alibert, Y. 2017, A&A, 608, A92

Drążkowska, J., Alibert, Y., & Moore, B. 2016, A&A, 594, A105

Drążkowska, J., Windmark, F., & Dullemond, C. P. 2013, A&A, 556, A37

Dubrulle, B., Morfill, G., & Sterzik, M. 1995, Icarus, 114, 237

Dullemond, C. P. 2000, A&A, 361, L17

Dullemond, C. P., & Dominik, C. 2004, A&A, 417, 159

Dullemond, C. P., Dominik, C., & Natta, A. 2001a, ApJ, 560, 957

—. 2001b, ApJ, 560, 957

Dullemond, C. P., Juhasz, A., Pohl, A., et al. 2012, RADMC-3D: A multi-purpose radiative transfer tool, Astrophysics Source Code Library, , , ascl:1202.015

Dullemond, C. P., & Monnier, J. D. 2010, ARA&A, 48, 205

Dzyurkevich, N., Flock, M., Turner, N. J., Klahr, H., & Henning, T. 2010, A&A, 515, A70

Ercolano, B., & Glassgold, A. E. 2013, MNRAS, 436, 3446

Flock, M., Fromang, S., Turner, N. J., & Benisty, M. 2016, ApJ, 827, 144

—. 2017, ApJ, 835, 230

Franchi, I. A., Wright, I. P., Sexton, A. S., & Pillinger, C. T. 1999, Meteoritics and Planetary Science, 34, 657

Fressin, F., Torres, G., Charbonneau, D., et al. 2013, ApJ, 766, 81

Gammie, C. F. 1996, ApJ, 462, 725

Gonzalez, J.-F., Laibe, G., & Maddison, S. T. 2017, MNRAS, 467, 1984

Gressel, O., Turner, N. J., Nelson, R. P., & McNally, C. P. 2015, ApJ, 801, 84

Grimm, S. L., Demory, B.-O., Gillon, M., et al. 2018, A&A, 613, A68

Gundlach, B., & Blum, J. 2015, ApJ, 798, 34

Hansen, B. M. S. 2009, ApJ, 703, 1131

Hayashi, C. 1981, Progress of Theoretical Physics Supplement, 70, 35

Hirose, S. 2015, MNRAS, 448, 3105

Isella, A., & Natta, A. 2005, A&A, 438, 899

Isella, A., Guidi, G., Testi, L., et al. 2016, PhRvL, 117, 251101

Jaeger, C., Mutschke, H., Begemann, B., Dorschner, J., & Henning, T. 1994, A&A, 292, 641

Johansen, A., Oishi, J. S., Mac Low, M.-M., et al. 2007, Nature, 448, 1022

Johansen, A., Youdin, A. N., & Lithwick, Y. 2012, A&A, 537, A125

Kama, M., Min, M., & Dominik, C. 2009, A&A, 506, 1199

Kanagawa, K. D., Muto, T., Tanaka, H., et al. 2015, ApJ, 806, L15

—. 2016, Publications of the Astronomical Society of Japan, 68, 43

Keppler, M., Benisty, M., Müller, A., et al. 2018, A&A, 617, A44

Klahr, H., & Lin, D. N. C. 2005, ApJ, 632, 1113

Klahr, H. H., & Bodenheimer, P. 2003, ApJ, 582, 869

Kleine, T., Touboul, M., Bourdon, B., et al. 2009, Geochimica et Cosmochimica Acta, 73, 5150

Kretke, K. A., Lin, D. N. C., Garaud, P., & Turner, N. J. 2009, ApJ, 690, 407

Kusaka, T., Nakano, T., & Hayashi, C. 1970, Progress of Theoretical Physics, 44, 1580

Long, F., Pinilla, P., Herczeg, G. J., et al. 2018, arXiv e-prints, arXiv:1810.06044

Lopez, B., Lagarde, S., Jaffe, W., et al. 2014, The Messenger, 157, 5

Lynden-Bell, D., & Pringle, J. E. 1974, MNRAS, 168, 603

Lyra, W. 2014, ApJ, 789, 77

Lyra, W., & Mac Low, M.-M. 2012, ApJ, 756, 62

Masset, F. S., Morbidelli, A., Crida, A., & Ferreira, J. 2006, ApJ, 642, 478

Mathis, J. S., Rumpl, W., & Nordsieck, K. H. 1977, ApJ, 217, 425

Meeus, G., Waters, L. B. F. M., Bouwman, J., et al. 2001, A&A, 365, 476

Meeus, G., Montesinos, B., Mendigutía, I., et al. 2012, A&A, 544, A78

Mentiplay, D., Price, D. J., & Pinte, C. 2018, MNRAS, L210

Menu, J., van Boekel, R., Henning, T., et al. 2015, A&A, 581, A107

Millan-Gabet, R., Che, X., Monnier, J. D., et al. 2016, ApJ, 826, 120

Min, M., Dullemond, C. P., Dominik, C., de Koter, A., & Hovenier, J. W. 2009, A&A, 497, 155

Monnier, J. D., & Millan-Gabet, R. 2002, ApJ, 579, 694

Mulders, G. D., Pascucci, I., & Apai, D. 2015, ApJ, 798, 112

Nakagawa, Y., Sekiya, M., & Hayashi, C. 1986, Icarus, 67, 375

Nakamoto, T., & Nakagawa, Y. 1994, ApJ, 421, 640

Natta, A., Prusti, T., Neri, R., et al. 2001, A&A, 371, 186

Nimmo, F., & Kleine, T. 2007, Icarus, 191, 497

Nomura, H., Tsukagoshi, T., Kawabe, R., et al. 2016, ApJL, 819, L7

Ogihara, M., Kokubo, E., Suzuki, T. K., & Morbidelli, A. 2018, A&A, 612, L5

Oka, A., Nakamoto, T., & Ida, S. 2011, ApJ, 738, 141

Okuzumi, S., & Hirose, S. 2012, ApJL, 753, L8

Okuzumi, S., Momose, M., Sirono, S.-i., Kobayashi, H., & Tanaka, H. 2016, ApJ, 821, 82

Ormel, C. W., & Cuzzi, J. N. 2007, A&A, 466, 413

Paardekooper, S.-J., Baruteau, C., Crida, A., & Kley, W. 2010, MNRAS, 401, 1950

Perez-Becker, D., & Chiang, E. 2011, ApJ, 735, 8

Pinilla, P., Flock, M., Ovelar, M. d. J., & Birnstiel, T. 2016, A&A, 596, A81

Pinilla, P., Pohl, A., Stammler, S. M., & Birnstiel, T. 2017, ApJ, 845, 68

Pollack, J. B., Hollenbach, D., Beckwith, S., et al. 1994, ApJ, 421, 615

Qin, L., & Carlson, R. W. 2016, GEOCHEMICAL JOURNAL, 50, 43

Raymond, S. N., O'Brien, D. P., Morbidelli, A., & Kaib, N. A. 2009, Icarus, 203, 644

Ros, K., & Johansen, A. 2013, A&A, 552, A137

Rybicki, G. B., & Lightman, A. P. 1985, Radiative processes in astrophysics.

Santerne, A., Moutou, C., Tsantaki, M., et al. 2016, A&A, 587, A64

Sato, T., Okuzumi, S., & Ida, S. 2016, A&A, 589, A15

Schoonenberg, D., & Ormel, C. W. 2017, A&A, 602, A21

Shakura, N. I., & Sunyaev, R. A. 1973, A&A, 24, 337

Simon, J. B., Armitage, P. J., Li, R., & Youdin, A. N. 2016, ApJ, 822, 55

Simon, J. B., Armitage, P. J., Youdin, A. N., & Li, R. 2017, ApJ, 847, L12

Tan, J. C., Chatterjee, S., Hu, X., Zhu, Z., & Mohanty, S. 2015, ArXiv e-prints, arXiv:1510.06703

Tanaka, H., Himeno, Y., & Ida, S. 2005, ApJ, 625, 414

Tanaka, H., Takeuchi, T., & Ward, W. R. 2002, ApJ, 565, 1257

Testi, L., Birnstiel, T., Ricci, L., et al. 2014, Protostars and Planets VI, 339

Toomre, A. 1964, ApJ, 139, 1217

Ueda, T., Okuzumi, S., & Flock, M. 2017, ApJ, 843, 49

Umebayashi, T., & Nakano, T. 1981, Publications of the Astronomical Society of Japan, 33, 617

van Boekel, R., Henning, T., Menu, J., et al. 2017, ApJ, 837, 132

Vinković, D., Ivezić, Ž., Jurkić, T., & Elitzur, M. 2006, ApJ, 636, 348

Wada, K., Tanaka, H., Okuzumi, S., et al. 2013, A&A, 559, A62

Wada, K., Tanaka, H., Suyama, T., Kimura, H., & Yamamoto, T. 2008, ApJ, 677, 1296

Wang, X.-M. 2015, MNRAS, 449, 1084

Watanabe, S.-i., & Lin, D. N. C. 2008, ApJ, 672, 1183

Weidenschilling, S. J. 1977, MNRAS, 180, 57

Weingartner, J. C., & Draine, B. T. 2001, ApJ, 548, 296

Whipple, F. L. 1972, in From Plasma to Planet, ed. A. Elvius, 211

Wittmann, A., Korotev, R. L., Jolliff, B. L., et al. 2015, Meteoritics and Planetary Science, 50, 326

Yang, C.-C., Johansen, A., & Carrera, D. 2017, A&A, 606, A80

Youdin, A. N., & Goodman, J. 2005, ApJ, 620, 459

Youdin, A. N., & Lithwick, Y. 2007, Icarus, 192, 588

Zhu, W., Petrovich, C., Wu, Y., Dong, S., & Xie, J. 2018, ApJ, 860, 101

Zhu, Z., Nelson, R. P., Dong, R., Espaillat, C., & Hartmann, L. 2012, ApJ, 755, 6